UNIVERSITY OF THESSALY
SCHOOL OF ENGINEERING
DEPARTMENT OF MECHANICAL ENGINEERING

Air-Assist Atomizer Spray in Cross-Flow

by
KONSTANTINOS TINGOS

Submitted in partial fulfillment of the requirements for the degree of Diploma in Mechanical Engineering at the University of Thessaly

Volos, 2022

© 2022

All rights reserved. The approval of the present D Thesis by the Department of Mechanical Engineering, School of Engineering, University of Thessaly, does not imply acceptance of the views of the author (Law 5343/32 art. 202).

Approved by the Committee on Final Examination:

Advisor	Dr. Georgios Charalampous, Assistant Professor, Department of Mechanical Engineering, University of Thessaly
Member	Dr. Anastasios Stamatelos, Professor, Department of Mechanical Engineering, Aristotle University of Thessaly
Member	Dr. Nikolaos Andritsos, Professor, Department of Mechanical Engineering, University of Thessaly

Date Approved: [09, 21, 2022]

Acknowledgements

This thesis was conducted in partial fulfillment of the requirements for the Diploma of Mechanical Engineering at the University of Thessaly. In this context, it is worth mentioning the incredible support and assistance received by certain people.

First and foremost, I would like to express my sincere gratitude and appreciation to my supervisor Assistant Professor Dr. Georgios Charalampous, who gave me the opportunity and entrusted me to work on this particular project, in conjunction to his constant teachings. His continuous support and motivation provided me with the according aid to overcome every difficulty that arose during the experiments, as well in the completion of my thesis. His excellent guidance and tutoring through the experimental procedures and the according theory of the topic, were of enormous significance not only for the completion of the project, but also for my deep understanding and acquisition of knowledge upon the subject. Throughout the course of my thesis, my supervisor dedicated an immense amount of time and energy to assist and transmit his knowledge to me, and I am really grateful to him.

In addition to my supervisor, I would like to sincerely thank the members of my thesis committee, Professor Dr. Anastasios Stamatelos and Professor Dr. Nikolaos Andritsos, for the knowledge and inspiration transmitted to me through their teachings, during my studies.

Last but not least, I would like to thank my family for their significant support during my studies. I am really grateful to my parents, Stefanos Tingos and Eleni Kotsiri, for the mental support they provided me with. A special thanks goes to my mother Eleni, for helping me with improving the appearance of my thesis. Lastly, I would like to thank my brother Filippos Tingos for the many times he lent me his computer, to work on my thesis.

AIR-ASSIST ATOMIZER SPRAY IN CROSS-FLOW

KONSTANTINOS TINGOS

Department of Mechanical Engineering, University of Thessaly

Supervisor: Dr. Georgios Charalampous

Assistant Professor, Thermofluid Processes with Energy Applications

Abstract

The main research interest of this project is the investigation of the attributes of a spray or jet structure, injected in a crossflow airstream. The primary physical phenomena reviewed are the atomization of the liquid and the liquid/gas flow interaction. The problem is mainly governed by the following parameters: the liquid Reynolds Re, the crossflow Weber We, the liquid-to-crossflow momentum ratio q, and the atomizer gas-to-liquid mass flow GLR. The variables ranged about Re=1200-2700, We=0-0.68, q=340-1750 and GLR=0.25-0.41. For the purpose of this study, an experimental configuration is employed, utilizing a twin-fluid, air-assist atomizer for the atomization of the liquid. The airflow is uniform and is generated by a centrifugal blower. As the experimental method, the shadowgraphy technique is employed, utilizing a CCD camera for the collection of images. The obtained images are processed in order to acquire the characteristics of the spray. The main aspects of interest are: the spray/jet trajectory (centerline), the column breakup location (CBL) of the jet, and the spray boundaries. The trajectory and the boundaries are predicted employing a power-law interpolation, while the CBL is inspected statistically. In this study, it is demonstrated that the power-law function can effectively describe the trajectory, along with the spray boundaries. In the endnote, the conclusions are summarized, demonstrating associations in the spray characteristics, in conjunction with certain behavioral patterns of the problem.

Key words: spray, jet, crossflow, atomization, shadowgraphy, trajectory, CBL, spray boundaries, power-law

ΣΠΡΕΙ ΑΠΟ ΨΕΚΑΣΤΗΡΑ ΥΠΟΒΟΗΘΗΣΗΣ ΑΕΡΑ ΣΕ ΚΑΘΕΤΗ ΡΟΗ

ΚΩΝΣΤΑΝΤΙΝΟΣ ΤΙΓΓΟΣ

Τμήμα Μηχανολόγων Μηχανικών, Πανεπιστήμιο Θεσσαλίας, 2022

Επιβλέπων Καθηγητής: Δρ. Γεώργιος Χαραλάμπους,

Επίκουρος Καθηγητής, Θερμορευστομηχανικές Διεργασίες με Ενεργειακές Εφαρμογές

Περίληψη

Το κύριο ερευνητικό ενδιαφέρον αυτής της εργασίας είναι η διερεύνηση των χαρακτηριστικών μιας δομής σπρέι (spray) ή δέσμης (jet), που εγχέεται σε ένα ρεύμα αέρα εγκάρσιας ροής. Τα φαινόμενα που εξετάζονται είναι ο ψεκασμός του υγρού και η αλληλεπίδραση μεταξύ υγρής/αέριας φάσης. Το πρόβλημα διέπεται κυρίως από τις ακόλουθες παραμέτρους: τον Reynolds Re του υγρού, τον Weber We της εγκάρσιας ροής, τον λόγο ορμής q του υγρού/εγκάρσιας ροή και την ροή αέρα του ψεκαστήρα προς το υγρό GLR. Οι μεταβλητές κυμαίνονται περίπου στις ακόλουθες τιμές: Re=1200-2700, We=0-0,68, q=340-1750 και GLR=0,25-0,41. Η πειραματική διάταξη που χρησιμοποιήθηκε φέρει έναν ψεκαστήρα δύο-ρευστών με υποβοήθηση αέρα για τον ψεκασμό του υγρού. Η ροή του εγκάρσιου αέρα είναι ομοιόμορφη και παράγεται από έναν φυγοκεντρικό φυσητήρα. Ως πειραματική μέθοδος, αξιοποιήθηκε η τεχνική σκιογράφησης (shadowgraphy), χρησιμοποιώντας μια κάμερα CCD για τη συλλογή εικόνων. Οι ληφθείσες εικόνες υποβάλλονται σε επεξεργασία προκειμένου να αποκτηθούν τα χαρακτηριστικά του spray. Τα κύρια χαρακτηριστικά ενδιαφέροντος είναι: η τροχιά του spray/jet (μέση γραμμή), το σημείο διάσπασης (CBL) του jet και τα όρια του spray. Η τροχιά και τα όρια προβλέπονται με παρεμβολή ενός εκθετικού κανόνα, ενώ το CBL ελέγχεται στατιστικά. Στην παρούσα μελέτη, αποδεικνύεται ότι ο εκθετικός κανόνας μπορεί να περιγράψει αποτελεσματικά την τροχιά, καθώς και τα όρια του spray. Στο τελευταίο κεφάλαιο, συνοψίζονται τα συμπεράσματα, τα οποία καταδεικνύουν συσχετίσεις μεταξύ χαρακτηριστικών του σπρέι

και ορισμένων μεταβλητών, σε συνδυασμό με ορισμένα μοτίβα συμπεριφοράς του προβλήματος.

Λέξεις-κλειδιά: spray, jet, διασταυρούμενη ροή, ψεκασμός, σκιογράφηση, τροχιά, CBL, όρια spray, εκθετικός κανόνας

CONTENTS

Chapter 1 Introduction 15

1.1 Fundamental Principles and Applications 15

1.2 Atomizers – Spray Nozzles 17

1.2.1 Hydraulic Atomizers 19
1.2.2 Rotary and Swirl Atomizers 20
1.2.3 Twin-Fluid Atomizers 22

1.3 Atomization Theory Considerations 25

1.3.1 Disintegration of Capillary Liquid Jets 25
1.3.2 Liquid Jet in Crossflow (LJICF) 34

1.4 Spray Characteristics 46

1.4.1 Droplet Size Distribution 46
1.4.2 Dispersion 47
1.4.3 Penetration 48
1.4.4 Spray Angle and Coverage 48
1.4.5 Spray Pattern – Liquid Distribution 49

Chapter 2 Experimental Set-up: Equipment and Procedures 51

2.1 Experimental Conditions 51

2.2 Experimental Arrangement 53

2.2.1 Blower and Circular Duct 54
2.2.2 Atomizer and Liquid Supply 55
2.2.3 Shadowgraphy: Camera and Illumination 57

2.3 Calibration Procedures: Liquid Supply and Air Crossflow 63

2.3.1 Liquid Supply Calibration 63
2.3.2 Crossflow Air Calibration 66

Chapter 3 Results and Discussion 72

3.1 Liquid Jet in Crossflow 72

3.1.1 Jet Data Processing: Binary Images Method 72
3.1.2 Jet Trajectory 73
3.1.3 Column Breakup Location 77

3.2 Liquid Spray in Crossflow 86

3.2.1 Spray Data Processing: Liquid Mass Contours 86
3.2.2 Spray Trajectory-Centerline 87
3.2.3 Spray Boundaries 98

Chapter 4 Conclusions 103

Chapter 5 References 106

LIST OF TABLES

Table 1.1 LJICF parameters that affect crossflow and atomization characteristics..... 36

Table 2.1 Fluid properties and ambient conditions. 52

Table 2.2 Atomization conditions (liquid and atomizing air). 52

Table 2.3 Crossflow Conditions. 53

Table 2.4 Momentum flux $\boldsymbol{q}$ values, for every crossflow case. 53

Table 2.5 Pressure difference and volumetric supply average values, with their corresponding standard deviations. 65

Table 2.6 Discharge coefficient average values and standard deviations. 66

Table 2.7 Crossflow air calibration results 71

LIST OF FIGURES

Figure 1.1 Few mechanisms of primary atomization formation, each one relying on different methods of generating instabilities in the liquid bulk. (https://www.researchgate.net/figure/Mechanisms-of-primary-atomization-Aerodynamic-breakup-is-caused-by-interaction-with_fig2_272063743) 16

Figure 1.2 Atomization process. The primary and secondary stages are illustrated, as well the area of development of the spray, and the formed spray region (Berrocal & Jönsson, n.d.; modified). 17

Figure 1.3 Atomizers Classification: (a) Hydraulic Atomizers, (b) Rotary & Swirl Atomizers, (c) Twin-Fluid Atomizers (Lefebvre & Mcdonell, 2017). 18

Figure 1.4 Schematics of two types of swirl atomizers (a) swirl nozzle with axial flow, (b) swirl nozzle with tangential flow (Ashgriz, 2011). 21

Figure 1.5 Illustration of rotary atomizer operation. Fluid enters the rotating part of the device and is discharged peripherally (https://commons.wikimedia.org/wiki/File:Rotary_atomization_concept.gif). 22

Figure 1.6 (a) Plain Jet airblast nozzle (b) Prefilming airblast nozzle (https://www.researchgate.net/figure/Sketch-of-plain-jet-a-and-prefilming-b-airblast-atomizers-from-Lefebvre-1989_fig7_285674175) 24

Figure 1.7 Illustration of wave formation upon an unstable jet (Ashgriz, 2011). 28

Figure 1.8 Nondimensional growth rate of the disturbance, depending on the wavenumber $\boldsymbol{k}$ and the initial jet radius $\boldsymbol{Ro}$ (Ashgriz, 2011). 29

Figure 1.9 (a) Jet breakup with satellite droplets (b) Uniform breakup to almost spherical droplets with average diameter of $\mathbf{1.89}\boldsymbol{d}$ (Ashgriz, 2011). 30

Figure 1.10 Nondimensional disturbance growth rate in relation to wavenumber and liquid viscosity $\boldsymbol{Oh} = \boldsymbol{\mu\rho\sigma Ro}$ (Ashgriz, 2011). 31

Figure 1.11 Jet breakup regimes (Lefebvre & Mcdonell, 2017). 33

Figure 1.12 Ohnesorge chart: Jet breakup mechanism in subject to $\boldsymbol{Re}$ and $\boldsymbol{Oh}$ (Lefebvre & Mcdonell, 2017). 34

Figure 1.13 Jet deflection caused by the aerodynamic interaction with the airflow (Ashgriz, 2011). 38

Figure 1.14 Formation of axisymmetric perturbations in LJICF. 40

Figure 1.15 Growth rates of instabilities for different azimuthal models (a) q=0.0 (b) q=0.01 41

Figure 1.16 Shadowgraph technique illustrated. The light ray is deflected by passing through the dense fluid, creating a brighter spot in the deflected ray point, and a dark spot in the undeflected one (https://thermopedia.com/content/1117/). 42

Figure 1.17 (a) Force balance on a small element with thickness $\boldsymbol{h}$ (b) Deformation of the cross-section area of the jet due to crossflow (Ashgriz, 2011). 44

Figure 1.18 Jet deformation over time. $\boldsymbol{AR}$ is decreased as the shape becomes more eliptical (Ashgriz, 2011). 45

Figure 1.19 Cone angle and theoretical coverage of a spray for a specified distance (https://www.steinen.com/engineering-information/). 49

Figure 1.20 (a) Schematic of patternator measuring radial liquid distribution (b) Device standards and resulting distribution graph (Lefebvre & Mcdonell, 2017). 50

Figure 2.1 Experimental Arrangement. 54

Figure 2.2 Blower and inverter system. 55

Figure 2.3 Configuration of the duct. 55

Figure 2.4 Atomizer section: configuration, atomizer frontal view and digital flowmeter. 56

Figure 2.5 Liquid Supply: Pressure Tank and Flowmeter. 57

Figure 2.6 Typical Shadowgraph method arrangement (Cameron Tropea et al., 2007). 58

Figure 2.7 CCD sensors, charge transmission architectures: A) Full-frame transfer B) Frame transfer C) Interline transfer. 59

Figure 2.8 CCD camera with the tripod and A/D signal converter with the PC. 60

Figure 2.9 Shadowgraph experiment arrangement. 61

Figure 2.10 Background Images of the camera frame, for the nozzle orientation at $0o$ and $90o$ respectively. 61

Figure 2.11 Background Image calibration ($\boldsymbol{0o}$ and $\boldsymbol{90o}$) 62

Figure 2.12 Electrical Scale. 63

Figure 2.13 Volumetric supply calibrated with the average pressure differential $\boldsymbol{Q = Q\Delta P}$. 65

Figure 2.14 Discharge coefficient in relation with the Reynolds number. 66

Figure 2.15 Anemometry device and the hot-wire sensor. 68

Figure 2.16 Numerical grid for velocity integration (constant areas). 69

Figure 2.17 Crossflow velocity profiles for every inverter frequency. 70

Figure 2.18 Volumetric supply of air as a function of blower's frequency. 71

Figure 3.1 Data processing procedure. 73

Figure 3.2 Average jet images Re=1200. 74

Figure 3.3 Average jet images Re=2150. 74

Figure 3.4 Average jet trajectories for every Weber number, for Re=1200. 76

Figure 3.5 Average jet trajectories for every Weber number, for Re=2700. 76

Figure 3.6 Mean b in relation to Weber and Reynolds numbers. 77

Figure 3.7 Penetration distribution in comparison to We and Re 79

Figure 3.8 Deflection distribution in comparison to We and Re. 79

Figure 3.9 Average penetration and deflection in relation to the Weber number of the airflow, for every liquid flowrate. 81

Figure 3.10 Standard Deviation of the penetration and deflection in relation to the Weber number of the airflow, for every liquid flowrate. 81

Figure 3.11 Jet penetration in quasi-stationary atmosphere for every Reynolds case and atomizer orientation. 83

Figure 3.12 Jet Penetration Comparison for $\boldsymbol{Weg = 0}$. 84

Figure 3.13 Jet Penetration Comparison for $\boldsymbol{Weg = 0.68}$. 84

Figure 3.14 Penetration average trendlines for every crossflow case. 85

Figure 3.15 Mean error trendlines in comparison to Reynolds, for every Weber number. 86

Figure 3.16 Spray Processing. 87

Figure 3.17 Spray structures Re=1660, θ=0°. 88

Figure 3.18 Spray structures Re=1660, θ=90°. 88

Figure 3.19 Spray contour figures; Re=1660, GLR=0.34. 89

Figure 3.20 Spray centerline trajectories; Orientation 0°, Re=1660, GLR=0.34. 89

Figure 3.21 Spray centerline trajectories; Orientation 90°, Re=1660, GLR=0.34. 90

Figure 3.22 Maximum deflection in relation to Weber and atomizer orientation; Re=1660, GLR=0.34. 91

Figure 3.23 Exponent in relation to Weber and Reynolds; 8 L/min atomizing air, 0° orientation..... 92

Figure 3.24 Exponent in relation to Weber and Reynolds; 9 L/min atomizing air, 0° orientation..... 92

Figure 3.25 Exponent in relation to Weber and Reynolds; 1 L/min atomizing air, 0° orientation..... 93

Figure 3.26 Power-law fit credibility; Exponent=1.25..... 94

Figure 3.27 Exponent in relation to Weber and Reynolds; 8 L/min atomizing air, 90° orientation..... 94

Figure 3.28 Exponent in relation to Weber and Reynolds; 9 L/min atomizing air, 90° orientation..... 95

Figure 3.29 Exponent in relation to Weber and Reynolds; 11 L/min atomizing air, 90° orientation..... 95

Figure 3.30 Maximum spray deflection in relation to GLR and We; Re=1200..... 96

Figure 3.31 Maximum spray deflection in relation to GLR and We; Re=2700..... 97

Figure 3.32 Power-law fit for spray boundaries (Re=1200, We-0.0, GLR=0.47); 0° and 90° respectively. 98

Figure 3.33 0° orientation, 8L/min atomizing air; exponent of downstream and upstream boundaries respectively. 99

Figure 3.34 0° orientation, 9L/min atomizing air; exponent of downstream and upstream boundaries respectively. 99

Figure 3.35 0° orientation, 11L/min atomizing air; exponent of downstream and upstream boundaries respectively. 100

Figure 3.36 90° orientation, 8L/min atomizing air; exponent of downstream and upstream boundaries respectively. 101

Figure 3.37 90° orientation, 9L/min atomizing air; exponent of downstream and upstream boundaries respectively. 101

Figure 3.38 90° orientation, 11L/min atomizing air; exponent of downstream and upstream boundaries respectively. 102

Chapter 1 Introduction

1.1 Fundamental Principles and Applications

The phenomenon of atomization occurs when a liquid jet or sheet is disintegrated into a system of miniscule droplets, in a continuous gaseous phase (most commonly air). The basic principle behind this procedure, is imparting the liquid bulk with enough energy, in order to break it down and generate a spray. Following the spray formation, the liquid has extra surface area in contact with the atmosphere. Essentially, the energy needed for the creation of the extra contact area, coincides to the amount of energy required for the spray formation. The typical form of atomizers utilizes nozzle orifices, from where the liquid jet emerges and is dispersed to droplets either by its own kinetic energy or by subjecting it to a high-velocity gas flow.

A large variety of applications exist that utilize the principles of atomization. Internal Combustion Engines (I.C.E.), Gas Turbines, Rocket Engines, more often resort to the controlled fragmentation of fuel using atomizers (fuel injection). There are many industrial manufacturing related applications that also use the technology of atomizers. Additionally, apart from the most recognized implementations in engineering and industrial manufacturing processes, atomization is applicable to many fields such as agriculture, medicine and food technology. Crop spraying, medical sprays, consumer sprays, spray-drying, many cooling systems and fire suppression systems, are some examples of applications that rely on atomization.

The fundamental mechanism that causes liquid jet breakup is related to the development of perturbations of the characteristics of the physical system, such as velocity profiles, pressure gradient, flowrate, turbulence levels and even disturbances in some liquid properties like density, viscosity and surface tension. These disturbances in return, generate fluctuations of the jet surface known as wave instabilities. Though a complex process of wave oscillation dynamics, the liquid jet surface is stripped, producing ligaments, bag-like structures and large droplets. This is known as the primary atomization process, which is modeled

considering growing wave instabilities on the interface of the two fluids, produced by turbulence or several parameter disturbances or by a combination of both. According to that, the attributes of the breakup mechanism and as a result, the spray structure itself, depend on various factors such as velocity profiles, nozzle geometry, ambient gas conditions (Birouk & Lekic, 2009). The turbulence levels of the liquid flow in the atomizer can also potentially provide a large contribution to the jet disintegration, as it promotes wave instabilities. Additionally, the physical properties of the liquid and gaseous atmosphere can influence the formation of spray, like the viscosity of the two fluids, the densities, and the surface tension of the liquid. However, depending on the application, the importance of each property could change to a great extent. For instance, while the viscosity of the liquid generally constitutes an important parameter (Lefebvre & Mcdonell, 2017), it has been stated that the viscosity of the fuel in a direct diesel injection system, was found to have no considerable effect in the atomization process (Seykens et al., 2004). Considering the variety of parameters associated with the physical model of the problem, many methods have been developed over the years, it's one utilizing a different spectrum of the attributes of the physical system to cause atomization. Some of these methods are illustrated in Figure 1.1.

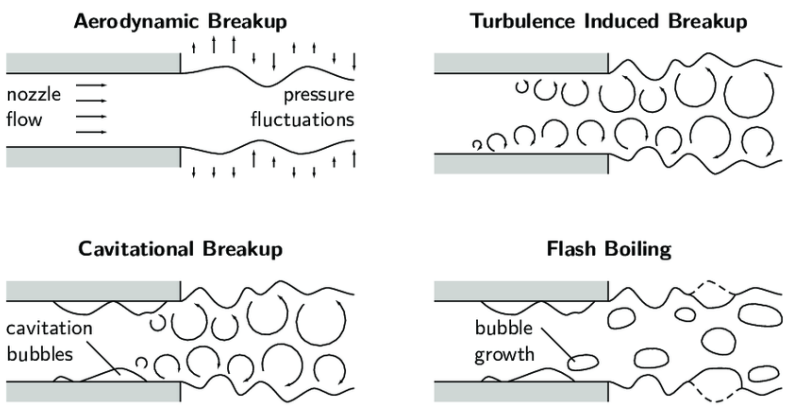

Figure 1.1 Few mechanisms of primary atomization formation, each one relying on different methods of generating instabilities in the liquid bulk.
(https://www.researchgate.net/figure/Mechanisms-of-primary-atomization-Aerodynamic-breakup-is-caused-by-interaction-with_fig2_272063743**)**

Following the first stage of spray formation, comes the secondary atomization, in which the already formed ligaments and droplets of liquid, continuously deform and break apart to even smaller sizes by the aerodynamic interaction with the ambient gas, disintegrating the

spray even further. The consideration and control of the secondary breakup mechanisms is also essential, as those determine the conditions that lead to the desired droplet size distribution in the spray structure (Guildenbecher et al., 2009). The stages of atomization process are visualized in Figure 1.2.

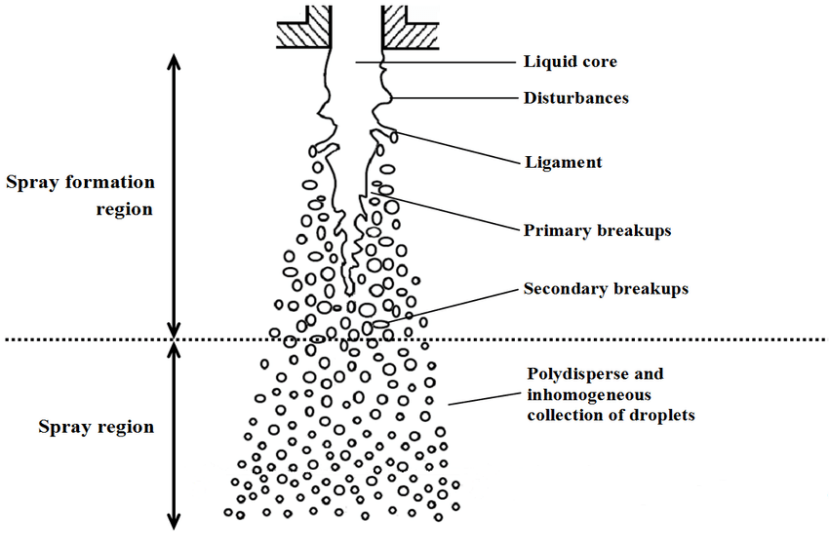

Figure 1.2 Atomization process. The primary and secondary stages are illustrated, as well the area of development of the spray, and the formed spray region (Berrocal & Jönsson, n.d.; modified)**.**

1.2 Atomizers – Spray Nozzles

Atomizers or Spray Nozzles are the devices that possess the ability to induce sufficient energy to the liquid flow and cause instabilities, in order to fragment it to miniscule droplets. Essentially, atomizer apparatuses discharge a liquid into a gaseous atmosphere (stationary or not), developing a fine spray structure. Several types of spray nozzles exist and usually they are classified according to the specific method its type utilizes to cause atomization. The most common types of atomizers are hydraulic (pressure) atomizers, rotary and swirl atomizers and twin fluid atomizers. Its category occupies a variety of nozzle types. Aside from the type of the nozzle, the principle utilized remains the same, the only distinction being usually the geometrical layout and/or the mechanisms used by the device to create the same effect. Different types of atomizers are illustrated in Figure 1.3. While this classification generally is applicable for investigation purposes and to predict the parameters

of the atomization procedure, occasionally a single nozzle may reside to more than one category due to its design, like pressure-swirl (simplex) nozzles.

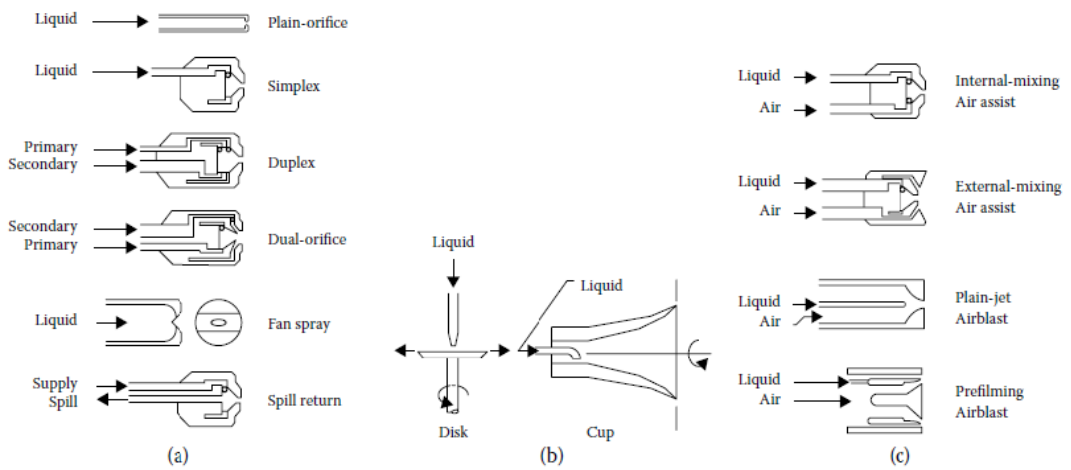

Figure 1.3 Atomizers Classification: (a) Hydraulic Atomizers, (b) Rotary & Swirl Atomizers, (c) Twin-Fluid Atomizers (Lefebvre & Mcdonell, 2017).

Furthermore, atomizers can be categorized based on operating parameters, such as mass flow rate, droplet size and liquid mass distribution, spray angle, spray pattern and spray impact. This classification is essential, as it provides information about the applications an atomizer is suitable for. Based on the design, atomizers process an optimal spectrum of liquid and ambient gas properties, mainly flowrate parameters, that is suited for the device operation. Nonetheless, a well-designed atomizer should be able to operate in a wide variety of liquid and gas flowrates and ambient conditions, while keeping the operation parameters like droplet diameter distribution, size mean diameter (SMD), spray angle etc. to the optimal values (Lefebvre & Mcdonell, 2017). This feature is important for the design of these apparatuses, as in most common applications, a high probability of a shift in the physical system input parameters exists.

Apart from the most common types of atomizers, many other types exist like ultrasonic and electrostatic atomizers. However, these designs belong to a more complex and peculiar category of apparatuses and their implementations and operation are too incompatible with

the experimental layout of this investigation. For that reason, only the common categories of atomizers mentioned above are reviewed.

1.2.1 Hydraulic Atomizers

Atomization process using hydraulic or pressure atomizers, relates to the use of pressurized liquid which flows in the chamber, and is ejected through a specifically shaped orifice. The geometry of the orifice acts as a nozzle which discharges the liquid and rapidly increases its velocity. With this procedure, the energy of the pressurized liquid is converted rapidly to kinetic energy, which causes the liquid to break into droplets. Consequently, hydraulic spray nozzles utilize the kinetic energy of the liquid to induce wave instabilities to the liquid and produce a spray structure. The underlying parameter in pressure atomizers is the orifice geometry, being responsible for the energy conversion and the shape of the spray. The design quality of these atomizers is of critical importance, as the high pressure state the nozzle is subjected to, can eventually cause damage, and decrease the effectiveness of the device (Ashgriz, 2011). The geometry of the orifice being the primary parameter here, these types of atomizers are able to produce a wide variety of spray shapes, depending on the orifice shape itself. A simple circular aperture produces a jet-like spray, a flat one produces a fan spray etc. When swirl motion is added, the hydraulic nozzle (simplex) is capable of producing a full cone or hollow cone spray structure.

When the liquid is forced through the aperture, high pressure drops as the velocity increases, thus, the discharging pressure difference is related to the change in velocity. Specifically, from Bernoulli's equation, it turns out that pressure difference is related to the difference of the squared velocity values. If the velocity of the liquid inside the chamber is considered small in comparison with the exit velocity, we can conclude that the exit velocity is a linear correlation of the square root of the pressure reduction, $U \sim \sqrt{\Delta P}$ (Lefebvre & Mcdonell, 2017). This implies that the entire energy of the pressurized liquid is transformed to kinetic energy without any losses, being an ideal situation. In reality, energy is lost in the form of heat by frictional phenomena during the liquid ejection, and the pressure difference is lower than the ideal one, thus, the velocity and consequently the flowrate are lower. This

phenomenon can be described by the discharge coefficient which for non-compressible flows, is defined as the actual flowrate to the ideal one:

$$C_d = \frac{Q_{exp}}{Q_{ideal}} \tag{1.1}$$

Generally, the discharge coefficient constitutes an important design variable for the most types of atomizers.

Hydraulic atomizers are applicable to many implementations. From simple uses like showers and lawn sprinklers, to engineering and industrial applications like concentrated cleaning, product cooling and fuel injection systems (plain nozzles).

1.2.2 Rotary and Swirl Atomizers

While the designs of these atomizers differ, they both rely on the same principle of producing atomization. In those apparatuses, the fluid inside the chamber rotates at a high velocity, thus experiencing a powerful centrifugal force. This results in the formation of a rotating liquid sheet, as the fluid departs from the center and is attached to the inner chamber periphery. While the rotating sheet exits the device from the orifice, it is discharged to the atmosphere similarly to the pressure atomizers. The swirl added to the liquid usually causes a full or hollow cone spray formation, those being the most common types of these atomizers. Full and hollow cone structures are strongly characterized by the fine droplets, the homogenous mass distribution and high spray angles they provide (Ashgriz, 2011). A large contact area can also be observed in this method of atomization.

Swirl Nozzles

Swirl atomizers, use specific geometry inside the chamber which guides the liquid, thus utilizing the fluid's kinetic energy to add a rotational movement to the flow. Swirl nozzles come in various designs, the most common of them being the axial and tangential flow designs (Figure 1.4) depending on the flow directions in the chamber and the exit. Axial flow devices, possess internal vein structures in order to guide the liquid to produce the swirl. A usual problem axial flow encounters, is clogging of the internal vein. This problem can be partially controlled by the modification of the liquid flow and smoothed internal surfaces (Gutiérrez et al., 2020). However, in these occasions axial flow outmatches in operating performance in contrast to the tangential flow, which undergo no clogging situations.

Tangential flow devices, propel the liquid inside the nozzle perpendicular to the exiting spray flow, generating rotational movement in absence of an internal vein. The latter also provide a very uniform cone spray, although the droplet sizes are not as small as in axial flow. Tangential apparatuses are considered the genuine form of swirl atomizers, since axial flow layouts are often used in twin-fluid and hydraulic atomizers (e.g. simplex nozzles) as it has been shown in Figure 1.3. Applications correlating to swirl atomization includes air pollution control with scrubbers, gas cooling, fuel inducing in chemical reactors and many more.

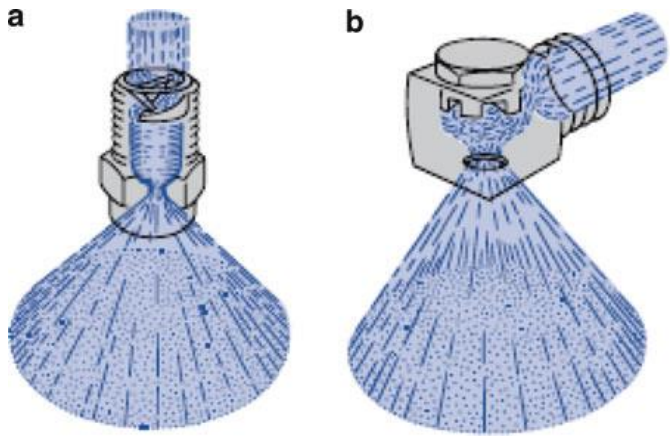

Figure 1.4 Schematics of two types of swirl atomizers (a) swirl nozzle with axial flow, (b) swirl nozzle with tangential flow (Ashgriz, 2011)**.**

Rotary Nozzles

Similarly to swirl nozzles, rotary atomizers utilize centrifugal phenomena to disintegrate the liquid. However, in contrast to swirl apparatuses, rotary nozzles usually employ a high-speed rotating disk, which surface comes in contact perpendicular to the liquid flow. The fluid experiences centrifugal force, flowing radially outward in contact with the disk and is discharged to the atmosphere from the periphery of the layout (Figure 1.5). The classification of these devices is often based on the type of rotating surface the liquid encounters. Most common types include smooth flat disk and disk with carved veins while other surfaces exist like slotted wheel and rotating cups. When the liquid flows axially to the spinning disk, different atomization mechanisms can be observed, with the principal parameter being the flow rate of the liquid. At relatively low flow rates, the centrifugal force induced causes the liquid to immediately form ligaments which are later broken down to droplets. This phenomenon advances rapidly, resulting in the formation of droplets inside the chamber. At high flow rates, ligaments continuously from along the disk surface and

gradually, droplets are segregated from them. The ligament size though remains constant, as the liquid on the disk replenishes the lost mass from after the departure of each droplet. The main characteristic and also an advantage of these mechanisms is that they tend to create a spray with mostly uniform droplet sizes (Ashgriz, 2011). A common problem encountered when using a flat disk, is the existence of slipping effects between the liquid/solid interface, tangentially to the radius. To compensate for that, a disk with vein structures can be used in order to guide the liquid radially. When the liquid reaches exceedingly high velocities, ligaments are unable to form on the disk surface and instead a fine liquid sheet is established peripherally, from which droplets break out gradually. While the atomizer is still functional, this promotes the generation of inconsistent droplet sizes. Compromising for this, a windmill disk (slotted wheel) shall be introduced, which increases the rotational speed allowing the formation of ligaments. Many implementations of rotary atomization exist such as inducing liquid in a boiler, fire extinguishing systems and lawn sprinklers.

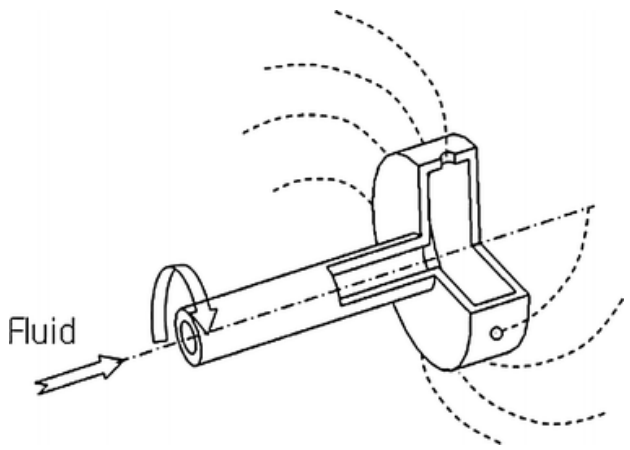

Figure 1.5 Illustration of rotary atomizer operation. Fluid enters the rotating part of the device and is discharged peripherally
(https://commons.wikimedia.org/wiki/File:Rotary_atomization_concept.gif **).**

1.2.3 Twin-Fluid Atomizers

Twin-fluid nozzles employ a high velocity flow steam of gas, most commonly air, which is mixed with the liquid flow, imparting the energy needed for atomization. These apparatuses are capable of producing very fine droplets, usually in a conical or a flat fan spray, while the liquid distribution is usually uneven. Typically, spray angles vary from 20° to 60°. The liquid

in the chamber can be controlled either by the pressurized method or using gravity. The syphon principle can also be used in some cases. The mixing of liquid and gas flows can be performed inside or outside the nozzle, resulting in the characterization of internal and external mixing. An important parameter in twin-fluid nozzles, along with the discharge coefficient which has been discussed in hydraulic atomizers, is the gas-to-liquid mass flowrate ratio (Ashgriz, 2011), defined as:

$$GLR = \frac{\dot{m}_G}{\dot{m}_L} \tag{1.2}$$

Various designs exist utilizing the twin-fluid atomization principles including airblast, air-assist and effervescent nozzles. The basic distinctions among these configuration variants, relates to the gas flowrate spectrum and the method of creating contact between the two fluids. Generally, twin-fluid nozzles are used in dust control, combustion engines, gas cooling, humidification, precision coating and spray dying.

Airblast Nozzles

This configuration implements internal mixing involving two eccentric tubes, in the inside being the liquid flow and in the surrounding one the gas flow (Figure 1.6). After the liquid is ejected into the gas chamber and is mixed with the gas, the liquid is discharged to the atmosphere. The air is supplied continuously and, in most cases, a large amount of air is induced in order to produce effective atomization, with relatively low air velocities. Airblast atomizers can be distinguished in plain jet and prefilming nozzles, relating to the form of the liquid bulk before disintegration. The two designs can be observed in Figure 1.6. Generally, the prefilming configuration is superior to the plain jet one, in terms of energy efficiency (Lefebvre & Mcdonell, 2017). Before the liquid is released to the high-flowrate gas stream, it is reduced into a thin film. This increases the contact area of the liquid; thus, a larger amount of energy is transferred from the gas stream. The thickness of the stream constitutes a significant design parameter here. Inconsistent film thickness, results in corresponding inconsistent droplet sizes (Ashgriz, 2011). This makes the design and construction of prefilming airblast atomizers demanding and they process reduced accuracy over long distances, in contrast to the plain jet ones. Airblast atomizers are commonly implemented in combustion systems. Specifically, their design is optimal for continuous combustion systems, like gas turbines, where the large air flowrate requirement is satisfied.

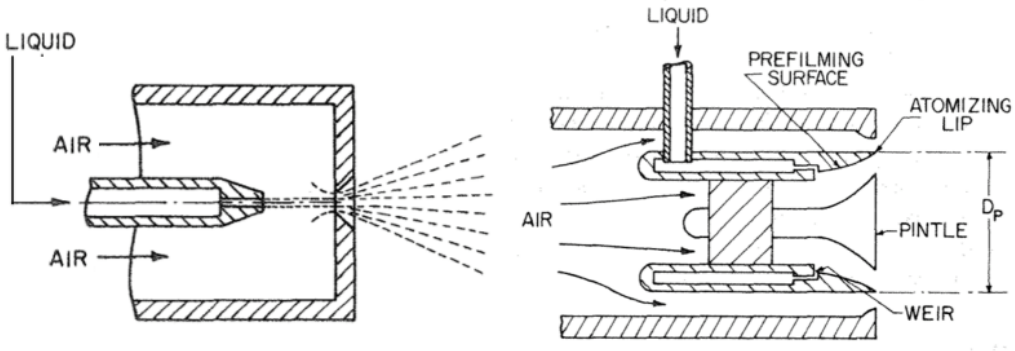

Figure 1.6 (a) Plain Jet airblast nozzle (b) Prefilming airblast nozzle
(https://www.researchgate.net/figure/Sketch-of-plain-jet-a-and-prefilming-b-airblast-atomizers-from-Lefebvre-1989_fig7_285674175**)**

Air-Assist Nozzles

These types of twin-fluid atomizers function similarly to airblast configuration, as they both mix liquid and gas streams to produce spray. In contrast to airblast nozzles, these devices sustain a pressurized air which is supplied only when needed and not continuously. According to this, air-assist nozzles employ high-velocity gas stream with low flowrate in comparison to airblast ones which require a large amount of air to atomize the liquid. The mixing configuration could be eternal or external. In the former, air is brought in contact with the liquid flow before it is discharged to the atmosphere, while in the latter air is mixed after the discharge sequence. While the internal mixing layout is more energy sufficient, the external mixing layout avoids back pressure problems, as there is no communication between the two fluids inside the chamber. Air-assist atomizers are often implemented in combustion systems, boilers, spray drying, cooling systems and crop-spraying.

Effervescent Atomizers

Effervescent, also known as cavitational atomizers, constitute a special type of apparatuses, which utilize twin-fluid atomization atypically, in comparison with the other types analyzed above. A small amount of gas is employed, in order to generate bubbles in the liquid, resulting in a two-phase bubbly flow. As the bubbly flow is discharged through the orifice, the pressure drop causes the bubbles to expand rapidly, disintegrating the liquid into ligaments which later are broken into small droplets by the interplay of gas expansion and their velocity. In addition to that, when the two-phase stream is ejected, the gas phase forces the liquid to exit through a smaller segment of the orifice, decreasing the resulting

droplet sizes even further. The bubbles are generated either by the injection of a small amount of air or by flash-boiling the liquid to topically vaporize it and produce vapor bubbles. The two-phase bubbly flow regime is of major importance to the correct operation of the atomizer. Effective atomization premises stable and uniform bubbly flow which depends on bubble formation and coalescence. Nozzle geometry, air, and liquid flowrates, pressure, and velocity instabilities affect the bubbly flow regime. Effervescent atomizers are implemented or may possibly be used in typical atomizing applications like gas turbine combustors, furnaces, and boilers (Ashgriz, 2011). A good potential even exists in more complex spraying systems like atomization of viscoelastic liquids and liquids with nanoparticles.

1.3 Atomization Theory Considerations

In the present segment, a basic theoretical analysis of atomization processes is presented. Specifically, considering the experimental configuration and procedures, theoretical studies of the jet breakup mechanisms are reviewed, both in quiescent atmosphere and crossflow conditions. In the case of a liquid jet in crossflow (LJICF), there is a greater number of factors that need to be considered, like the deflection and the deformation of the jet, and the trajectory it follows up to the breakup point.

1.3.1 Disintegration of Capillary Liquid Jets

A liquid jet emerging from the orifice of a nozzle can potentially disintegrate into ligaments and consequently, minuscule droplets. As mentioned before, the mechanism behind this procedure, involves the development of perturbations in the system resulting in the establishment of oscillatory motions, due to the unstable flow state. In an ideal situation, oscillations are magnified and the liquid breaks into droplets. The disturbances that promote this phenomenon may occur from; aerodynamic interaction deforming the liquid surface, pressure or velocity fluctuations (in the supply system or topically on the surface), or fluctuations in liquid properties like surface tension and viscosity.

The development of instabilities within a jet, and the dynamics it is subjected to, has been a subject of interest for over a century. Savart performed the first experimental investigation related to jet atomization. He demonstrated that a relation exists, among the column breakup location (CBL), jet diameter and velocity. Specifically, for constant values of diameter or velocity, CBL is proportional to the non-fixed variable (Savart, 1833). Plateau carried out the first theoretical investigation and his analysis came in agreement the experimental data provided by Savart. He proved that a liquid cylindrical column is unstable when its length exceeds its periphery (Plateau J, 1873). Plateau's work provided the principles where upon Rayleigh based his analysis of jet instabilities, which is the most prominent theory on jet atomization (Lord Rayleigh F.R.S., 1878). Weber later expanded upon Rayleigh's investigation, including the effects of the liquid's viscosity and the aerodynamic effects (Weber C, 1931).

Depending on the parameters of the physical system, different breakup regimes can emerge, therefore, different models should be considered in each case. Several theoretical models considering the capillary jet instabilities exist and are mainly developed through perturbation-type analysis. In general, this analysis envisages the problem, as a three-dimensional incompressible liquid/gas interface flow problem. According to this, the continuity equations along with Navier-Stokes equations are employed:

$$\nabla \cdot \mathbf{u_i} = 0 \tag{1.3}$$

$$\frac{D\mathbf{u_i}}{Dt} = \frac{\partial \mathbf{u_i}}{\partial t} + \mathbf{u_i} \cdot \nabla \mathbf{u_i} = -\frac{\nabla P_i}{\rho_i} + \nu_i \nabla^2 \mathbf{u_i} + g + \frac{\boldsymbol{F}}{\rho} \tag{1.4}$$

where $\mathbf{u_i} = (u_i, v_i, w_i)$ are the velocities and their components in x, r and θ directions respectively, P_i the pressure, ν_i the kinematic viscosity, ρ_i the densities, g the gravitational acceleration and F is the body force. The index "i", relates to the two phases of the problem, liquid and gas ($i \rightarrow l|g$). The equations describing the problem are partial differential equations (PDEs), in the general form.

Along with the PDEs of the problem, two boundary conditions are implemented on the interface of liquid/gas phases, being the stress balance and kinematic conditions:

$$\left(p_l - p_g + \sigma\kappa\right)\mathbf{n} = \left(\boldsymbol{\tau}_\mathbf{l} - \boldsymbol{\tau}_\mathbf{g}\right) \cdot \mathbf{n} \tag{1.5}$$

$$\boldsymbol{u_l} \cdot \boldsymbol{n} = \boldsymbol{u_g} \cdot \boldsymbol{n} \tag{1.6}$$

where $\boldsymbol{\tau}_\mathbf{l}$ and $\boldsymbol{\tau}_\mathbf{g}$ are the stress tensors of liquid and gas phases respectively, σ is the surface tension coefficient and κ is the average curvature of the interface:

$$\kappa = \nabla \cdot \mathbf{n} = \frac{1}{R_1} + \frac{1}{R_2} \tag{1.7}$$

where R_1 and R_2 are the curvature radii of the jet (Figure 1.7).

The implementation of instabilities lies in this variable, as perturbations promote oscillations, therefore the radius (and consequently, the curvature κ) of the cylindrical jet is fluctuating in time and/or along the three jet directions: $R = R(t, x, r, \theta)$.

The PDE's along with the boundary conditions are nondimensionalized and the problem depends on two dimensionless numbers: Reynolds number and Weber number.

$$Re_i = \frac{\rho_i U_i R_o}{\mu_i} \sim \frac{inertia}{viscosity}$$

$$We_i = \frac{\rho_i U_i^2 R_o}{\sigma} \sim \frac{inertia}{surface\ tension}$$

The Reynolds number depicts the ratio of inertia forces to viscous forces and provides information about the flow regime (laminar or turbulent). Weber number is the ratio of inertia forces to surface tension forces.

In addition to the perturbation-type studies, some models have been developed using quasi-one-dimensional analysis, where the liquid jet is considered as a long, linear continuum with no lateral dimension. Theoretical studies can be classified in two main categories: temporal and spatial analysis. Temporal investigations consider an infinite length jet, existing in an inertial state of reference. The growth rates of the disturbances remain the same along the jet (stationary perturbation waves) and their fluctuation in time variable can be exponential or oscillatory. Spatial analysis on the other hand, considers a semi-infinite jet (e.g., nozzle ejection). The growth rates of perturbations are considered along the semi-infinite jet and may be periodic in time, and oscillatory or exponential in space.

Atomization of Inviscid Liquid Jets – Rayleigh Model

In this regime, the liquid jet and the ambient gas are considered to have zero viscosity, therefore, $\nu_i = 0$. Additionally, the gaseous atmosphere effects are neglected, as they are assumed to have no considerable consequence. Assuming a periodic disturbance, the jet is supposed to produce axisymmetric surface waves (Figure 1.7). A small surface perturbation is considered upon the jet, which disturbs the velocities (u', v', w'), the pressure (P'), and radius of the jet. The radius of the jet fluctuates; accordingly, $R = R_o + \zeta$, where R_o is the initial radius and ζ is the small perturbation. Equations (1.3) and (1.4) are linearized around the average values point $(\bar{u}, \bar{v}, \bar{w}, \bar{P})$ accordingly: $X = \bar{X} + X'$ $(X \equiv u, v, w, P)$.

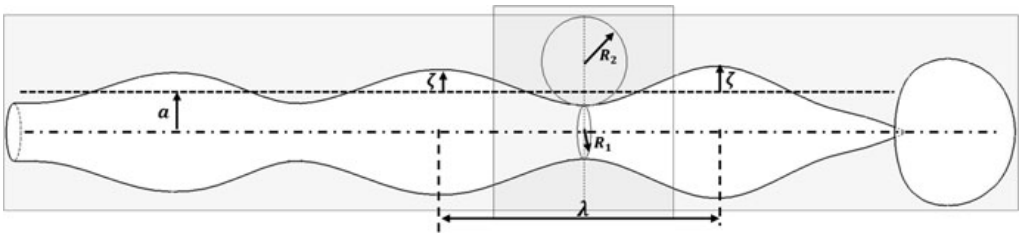

Figure 1.7 Illustration of wave formation upon an unstable jet (Ashgriz, 2011)**.**

Rayleigh used a periodic disturbance on the surface, in both axial and angular dimensions of the jet; $R(x, \theta) = R_o + \zeta(x, \theta)$. However, he established in his analysis that only axisymmetric disturbances can reduce the surface energy. Therefore, only axial disturbances may conclude to an unstable jet, as the liquid jet is stable for all angular perturbations (Lord Rayleigh F.R.S., 1878). Considering that a stable jet possesses only axial velocity, it can be concluded that the radial velocity on its surface is entirely due to the perturbation ζ; $v = \partial R/\partial t \Leftrightarrow v' = \partial\zeta/\partial t\,|_{r=R_o}$. Therefore, the general form of perturbation is found to be:

$$\zeta = C\frac{k}{R_o} I_1(kR_o)\exp(ikx + \omega t) \tag{1.8}$$

where, ω is the growth rate of the perturbation, $k = 2\pi/\lambda$ the wave number and I_1 is the modified Bessel function of the first kind:

$$I_n(z) = \frac{1}{\pi}\int_0^{\pi} e^{z\cos(\theta)}\cos(n\theta)\,dt - \frac{\sin(n\pi)}{\pi}\int_0^{\pi} e^{-z\cosh(t)-nt}\,dt$$

It is clear that, for every $n \in \mathbb{Z}$, $\sin(n\pi) = 0$, and therefore, for $n = 1$ an $z = kR_o$:

$$I_1(kR_o) = \frac{1}{\pi}\int_0^{\pi} e^{kR_o\cos(\theta)}\cos(\theta)\,dt$$

Utilizing equation (1.8) along with the stress boundary condition, the growth rate solutions can be found:

$$\omega = \frac{\sigma k}{\rho R_o^2}(1 - k^2R_o^2)\frac{I_1(kR_o)}{I_0(kR_o)} \tag{1.9}$$

The growth rate of the disturbance is related to the wave number k and the initial radius R_o. Figure 1.8 illustrates the spectrum of the disturbance growth rates.

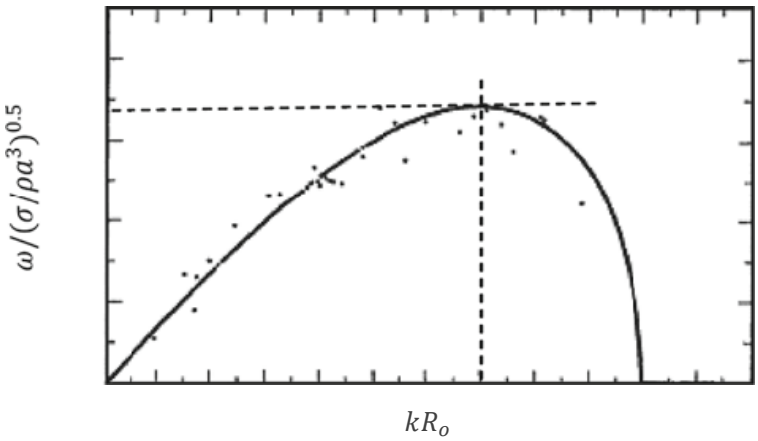

Figure 1.8 Nondimensional growth rate of the disturbance, depending on the wavenumber k and the initial jet radius R_o (Ashgriz, 2011)**.**

The interest coincides to the disturbance with the fastest growth rate, as it is the one which will finally cause the breakup of the jet. As Rayleigh proved, and as it can be concluded using Figure 1.8, the rate of the fastest-growing disturbance is given by:

$$\omega_{max} = 0.34\left(\frac{\sigma}{\rho R_o^3}\right)^{0.5} = 0.97\left(\frac{\sigma}{\rho d^3}\right) \tag{1.10}$$

The optimal wavelength corresponding to the maximum growth rate, results as:

$$\lambda_{opt} = 4.51d \tag{1.11}$$

After the breakup, a single wave becomes a droplet (Figure 1.7). The principle used to calculate the droplets diameter D is that the volume of the liquid remains the same. The departing liquid mass is cylindrical when the jet is whole, and the droplets are considered to be of spherical shape. Therefore:

$$\lambda_{opt} \times \frac{\pi}{4}d^2 = \frac{\pi}{6}D^3 \Longrightarrow D = 1.89d \tag{1.12}$$

Thus, for the Rayleigh breakup model the droplet size is 1.89 times bigger than the jet diameter. This model is based upon an ideal situation where the disturbance is axisymmetric, and all the droplets are spherical and of identical shape. In reality, when the detachment of the drop occurs, a small part of the jet is also striped at the end, which later breaks into very tiny droplets. For these, a high chance exist that they coalesce once more, and create a satellite droplet. The ideal and the real jet breakup can be observed in Figure 1.9. Even if the satellite formation is avoided, the droplets are never exactly of spherical shape, due to the deformation from the aerodynamic interaction with the atmosphere. It is considered that the average droplet diameter is $D = 1.89d$.

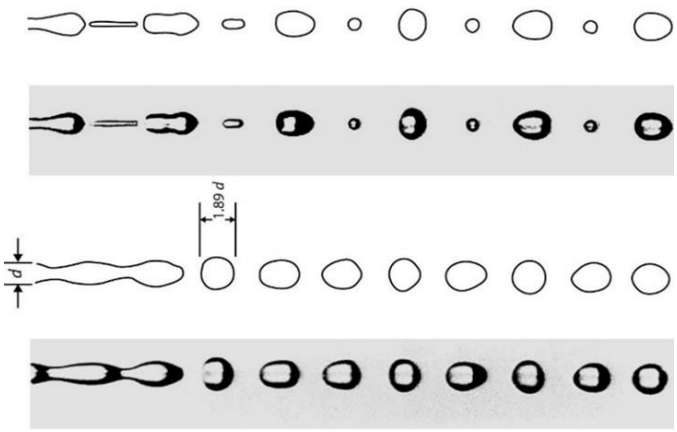

Figure 1.9 (a) Jet breakup with satellite droplets (b) Uniform breakup to almost spherical droplets with average diameter of $\mathbf{1.89d}$ (Ashgriz, 2011)**.**

Atomization of Viscous Liquid Jets – Weber Model

Weber provided a more general model, as he extended Rayleigh's theory on inviscid jets, by including the effects of viscosity on the developed wave instabilities; $v = \mu/\rho$. He also, assumed axisymmetric disturbances on the jet. According to the superposition principle, the solution of the axisymmetric velocity components of the jet, is the sum of the inviscid solution and the viscous jet solution: $(u, v) = (u_o + u_v, v_o + v_v)$. These are substituted into equations (1.3) and (1.4) and their new form is obtained. Solving the problem along with the boundary conditions (1.5) and (1.6), Weber obtained the disturbance growth rate spectrums, for different liquid viscosities as shown in Figure 1.10.

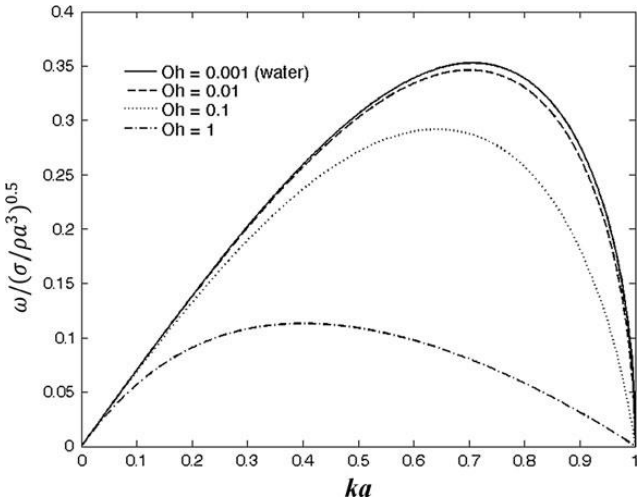

Figure 1.10 Nondimensional disturbance growth rate in relation to wavenumber and liquid viscosity $\left(\boldsymbol{Oh} = \boldsymbol{\mu}/\sqrt{\boldsymbol{\rho\sigma R_o}}\right)$ (Ashgriz, 2011)**.**

The fastest-perturbation growth rate is found to be:

$$\omega_{max} = \left[\left(\frac{8\rho R_o^3}{\sigma}\right)^{0,5} + \frac{6\mu R_o}{\sigma}\right]^{-1} = \left[\left(\frac{\rho d^3}{\sigma}\right)^{0,5} + \frac{3\mu d}{\sigma}\right]^{-1} \tag{1.13}$$

and the optimal wavelength is:

$$\lambda_{opt} = \sqrt{2\pi} d \left(1 + \frac{3\mu}{\sqrt{\rho\sigma d}}\right)^{0.5} \tag{1.14}$$

where μ and ρ are the dynamic viscosity and density of the liquid respectively.

If $\mu = 0$ is substituted in equation (1.14), $\lambda_{opt} = 4.44d$ is obtained, which is close to the wavelength/jet diameter ratio of 4.51 given by Rayleigh. Weber also investigated the effect surface tension has to the developing perturbation. He found out that there is a minimum wavelength value λ_{min}, below which, surface forces tend to damp the caused oscillation. For $\lambda > \lambda_{min}$ wave oscillations are amplified by surface tension, leading to the disintegration of the jet. For both viscous and non-viscous fluids, this barrier is given by $\lambda_{min} = \pi d$.

Consideration of Aerodynamic Effects

Weber later considered the effects ambient atmosphere has to the mechanisms of the jet breakup. These effects should be taken into consideration when the relative velocity between liquid and gas phase is high enough, or when the liquid/gas density ratio is relatively small (<500), (P.-K. Wu & G. M. Faeth, 1993). Generally, an increase in the relative gas velocity provides a corresponding decrease in the optimal and minimum wavelength and

the breakup location (Lefebvre & Mcdonell, 2017). The relative motion on the non-mixing liquid/gas interface produces a shear stress on the liquid surface, further promoting the production of wave instabilities. For Newtonian fluids, shearing force is heavily depended on the relative velocity between the interfaces of liquid and gas phases, thus, it becomes relevant only on high relative velocities. Moreover, the consideration of the density ratio is reasonable, provided that high density liquids appear to have high inertia and therefore, aerodynamic forces have no considerable effect. Another considerable effect caused by aerodynamic interaction, is the possible production if sinuous waves instead of axisymmetric ones. This effect can occur at increasing relative velocities and/or lower surface tension effects.

Comparison of breakup regimes – overview

The different breakup regimes can be summarized as follows (Lefebvre & Mcdonell, 2017).

1. Disintegration of liquid jet without aerodynamic forces. Axisymmetric oscillations can be observed, which eventually cause the breakup. Described by Rayleigh's model for non-viscous liquids, and Weber's model for viscous ones. Weber's model can also provide more accurate results for non-viscous breakup, very close to what Rayleigh predicted.
2. Disintegration of liquid jet with aerodynamic effects. At high velocities, the shear stress/friction caused by the surrounding gas can no longer be neglected. Aerodynamic forces tend to amplify the axisymmetric waves, disintegrating the jet faster.
3. Disintegration of liquid jet with sinuous waves. These oscillations can be produced by increasing aerodynamic effects, when the surface tension influence is overshadowed up to a point.

The jet disintegration regimes can be observed in Figure 1.11.

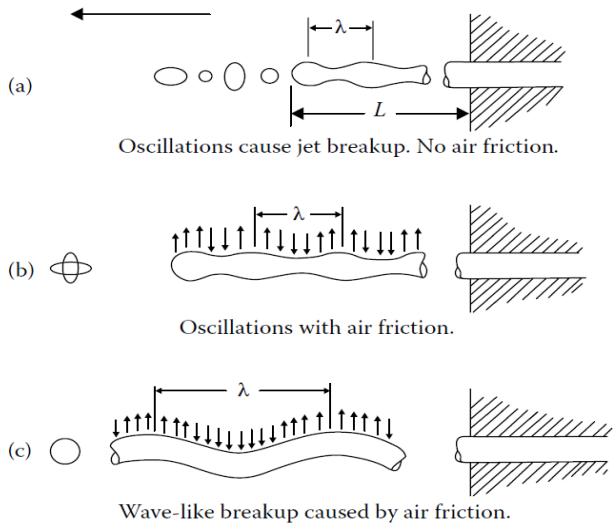

Figure 1.11 Jet breakup regimes (Lefebvre & Mcdonell, 2017).

Ohnesorge provided a useful correlation for the mechanism of the breakup, taking into account surface tension, viscosity, gravitational and inertial forces. The breakup regime mainly depends on two dimensionless numbers:

- Reynolds number: $Re = \rho_L U d_o / \mu_L \sim \frac{inertia\ forces}{viscous\ forces}$
- Ohnesorge number: $Oh = \mu_L / \sqrt{\rho_L \sigma d_o} \sim \frac{viscous\ forces}{\sqrt{inertia \cdot surface\ tension}}$

The Ohnesorge number describes the ratio of viscous forces to inertia and surface tension forces. Obviously, a correlation exists between these two numbers as they both depend by the same two physical parameters (inertia and viscosity), with the only different parameter being the surface tension in Oh. By introducing the corresponding Weber number, the correlation can be found as:

$$Oh = \frac{Re}{\sqrt{We}}$$

Ohnesorge chart is a useful method to verify the jet disintegration regime, in dependence of Reynolds and Ohnesorge number. This chart is illustrated in Figure 1.12.

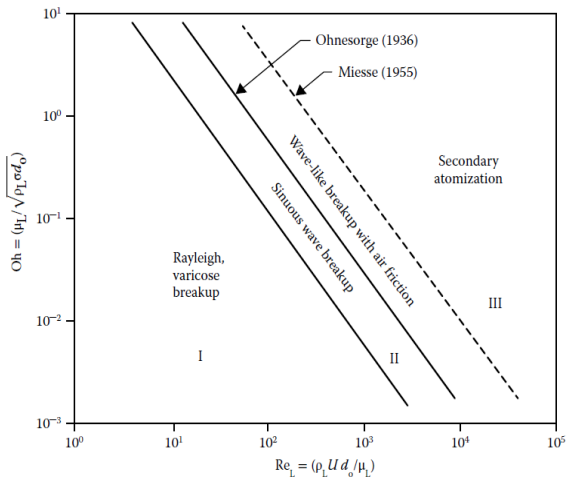

Figure 1.12 Ohnesorge chart: Jet breakup mechanism in subject to Re and Oh (Lefebvre & Mcdonell, 2017).

1.3.2 Liquid Jet in Crossflow (LJICF)

Liquid Jet in Crossflow or LJICF for abbreviation, refers to the mixing of liquid jet and a gas phase flow, perpendicular to each other. This procedure is implemented in various engineering applications and technologies, mainly revolving around fuel injection systems, like I.C. engines, gas turbines, afterburners, ramjet and scramjet combustors. The injection of fuel in crossflow improves fuel atomization and vaporization into the air flow, providing increased combustion efficiency. In return this provides higher power and lower pollutant emissions resulting from inefficient combustion processes (carbon monoxide, methane, VOCs, etc.).

Many theoretical, experimental, and computational studies involving LJICF atomization have been conducted over the years. The complexity of the physical system lays out many difficulties (e.g. vortex formations, wave formations, liquid mass stripping due to the aerodynamic disturbance) for the development of a three-dimensional, complete, theoretical model. Therefore, most of the studies analyze the problem with the assumption of a two-dimensional fluid mechanics system. Theoretical models mainly focus on the deformation of jet due to the aerodynamic interaction with the gas flow and the resulting trajectory before the disintegration. Experimental investigations are mainly used to obtain

information also for the jet path, the maximum penetration of the jet, and for the breakup mechanisms involved in the atomization process. The disintegration processes involve complex liquid/gas interface physics, that sometimes are hard to visualize with experimental investigations. For this purpose, computational models have been developed to provide additional information and visualize the atomization process along with the jet deflection more accurately.

General Considerations

In the injection of a liquid jet into an air crossflow, the flow regimes of both the jet and the airflow can affect the jet trajectory and the atomization process. In the simplest form of the problem, both flows are considered to be laminar, and the airflow has uniform velocity profile. When the jet is injected, the aerodynamic forces caused by the gas deflect its trajectory (from the y-direction of a jet in static gas, to the x-direction of the gas flow). The aerodynamic interaction also causes the deformation of the jet, from a circular cross-section to a sheet-like, elliptic one. These parameters, mainly depend on the relative momentum of the airflow in comparison to the liquid. The atomization of the liquid behaves in similar manner to the jet in static atmosphere, for relatively weak gas flows. When the relative momentum of the gas flow is strong, the aerodynamic interaction is increased, amplifying the instabilities upon the jet, causing more efficient atomization (Ashgriz, 2011). As the trajectory of the jet is deflected in this case, the column breakup location is constituted by the breakup position in relation to the two primary axes: $CBL = (x_b, y_b)$, where x_b and y_b are the location of the breakup in the x and y axis respectively. After the CBL, the ligaments formed undergo secondary atomization, which rate is also increased due to the airflow.

In addition to the final disintegration, the jet can potentially lose liquid mass as it follows its trajectory before the CBL if the airflow is strong enough. The aerodynamic forces acting upon the jet, strip liquid particles from its surface, which themselves can undergo secondary breakup. These liquid droplets along with the ones formed after the CBL constitute the atomized part of the liquid or the spray structure. By this point, the benefits of LJICF in comparison to simple jet atomization, become clear:

1. Airflow amplifies instabilities on the jet, increasing the efficiency of the primary atomization.

2. Airflow atomizes additional liquid mass before the primary breakup; therefore, more liquid is disintegrated in comparison to jet in quiescent gas, at any given time.

In order to increase the efficiency of the second mechanism, the contact area of the airflow with the jet needs to be as large as possible. Consequently, the y_b needs to be large enough to increase the trajectory of the jet before the CBL, and thus, the contact surface with the airflow. This parameter is known as maximum penetration of the jet and constitutes an important role in the atomization of LJICF.

In order to investigate the LJICF, the principal parameters that affect the crossflow and atomization regimes need to be determined. Those include fluid properties of the two fluids (liquid and gas), as well as the geometry of the configuration. The variables are categorized in Table 1.1.

Table 1.1 LJICF parameters that affect crossflow and atomization characteristics.

Fluid Properties	Geometry
Densities: ρ_j, ρ_g	Nozzle Diameter: d
Viscosities: μ_j, μ_g	Nozzle Length: L
Velocities: u_j, u_g	Injection Angle: a
Liquid Surface Tension: σ	

The importance of these properties can change to a considerable extent for a specific application. The length and diameter of the nozzle affect the entry conditions of the jet, through the dimensionless number of L/D (Surya Prakash et al., 2018). This dependence is not considered however, since the apparatus used in the experiment remains the same, therefore, the entry conditions remain constant. Considering the experimental layout of this project, injection angles are not included as well, thus $a = 0^o$. These parameters can be included in a group of dimensionless numbers, from which the physical system depends. According to Buckingham π-theorem, the resulting dimensionless numbers are the following:

1. The momentum ratio of the liquid to gas phase: $q = \rho_j u_j^2 / \rho_g u_g^2$
2. The Weber number, defined as the inertia forces of the gas phase to the surface tension forces due to the liquid phase: $We_g = \rho_g u_g^2 d / \sigma$
3. The Reynolds number of the jet as it exits the nozzle: $Re_j = \rho_j u_j d / \mu_j$

Therefore, a specific characteristic, let C, of the LJICF system, can be expressed as:

$$C = f(q, We_g, Re_j)$$

These three numbers are of great importance for studying the resulting characteristics of the jet. The momentum ratio q, expresses the relative momentum of the liquid to the gas phase. Jet deflection and penetration heavily depend on this parameter, and as q fluctuates, their values change inversely proportional to its other. Small q values result in high deflection and low penetration of the jet, while in large values the jet deflects less, and penetrates more. The Weber number measures the importance of the gas inertia forces in comparison with the surface tension forces of the liquid. The sizes of the formed ligaments and droplets after the breakup, mainly depend on this parameter. Reynolds number provides information about the turbulence levels of the system, and thus, the secondary instabilities of the breakup regime. In a laminar gas flow, Reynolds number mainly affects droplet sizes, developed velocity profiles, and CBL values. However, if the flow of the gas is not laminar, a comprehensive study of the breakup regimes should investigate both the turbulence levels of the jet and the gas flow, hence, two Reynolds numbers should be taken into consideration (Ashgriz, 2011).

Jet Trajectory

In order to investigate the trajectory, the jet is considered to be of cylindrical shape and non-deformable, thus, the diameter of the jet remains constant. In addition, no liquid mass is considered to be stripped of the jet. A small cylindrical element is considered upon the jet, with diameter d (same as the rest of the jet) and heigh h (Figure 1.13). As mentioned above, jet deflection is caused by the aerodynamic interaction with the airflow (Ashgriz, 2011).

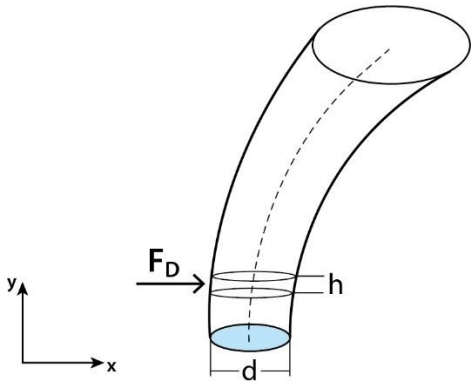

Figure 1.13 Jet deflection caused by the aerodynamic interaction with the airflow (Ashgriz, 2011)**.**

Therefore, the only force acting horizontally upon the cylindrical surface of the jet is the aerodynamic drag force F_D, which is expressed as:

$$F_D = \frac{1}{2}\rho_g u_g^2 A_F C_D \tag{1.15}$$

where, C_D is the drag coefficient and $A_F = d \times h$ is the frontal cylindrical area. Since the deformation is neglected, the cross-sectional area of the jet remains constant and circular, thus, $A_C = \pi d^2/4$.

Force balancing the element on the x-axis, results in:

$$F_D = m_j \ddot{x} \Leftrightarrow \frac{1}{2}\rho_g u_g^2 A_F C_D = \rho_j A_C h \frac{d^2x}{dt^2} \tag{1.16}$$

Substituting A_F and A_C and integrating two times results in:

$$\frac{x}{d} = \frac{1}{\pi} C_D \frac{\rho_g}{\rho_j} u_g^2 \frac{t^2}{d^2} \tag{1.17}$$

When the jet exits the nozzle, it possesses only vertical velocity u_j, since $a = 0^o$. According to the superposition principle, since no forces are acting on the jet in the y-direction, the vertical term of the velocity remains constant. Therefore, the penetration of the jet is calculated as $y = u_j t \Longrightarrow t = \frac{y}{u_j}$. Substituting the time into equation (1.17) results in:

$$\frac{y}{d} = \sqrt{\frac{\pi}{C_D} q \left(\frac{x}{d}\right)} \tag{1.18}$$

or, by solving for the x travel distance:

$$\frac{x}{d} = \frac{C_D}{\pi q}\left(\frac{y}{d}\right)^2 \tag{1.19}$$

where q is the momentum ratio $q = \rho_j u_j^2 / \rho_g u_g^2$, analyzed above.

1.18 and 1.19 resulted while neglecting the deformation of the jet and the reduction of the liquid mass. These results generally provide good results for relatively high momentum ratios, but in this situation, the deflection is relatively low (Ashgriz, 2011). Many experimental investigations have provided empirical correlations for jet penetration. Generally, these correlations come in the form of:

$$\frac{y}{d} = Cq^{\alpha}\left(\frac{x}{d}\right)^{\beta} \tag{1.20}$$

Where α, β and C are constants. This correlation suggests the importance of the momentum ratio, and α is expected to be around 0.5 from the theory. A more general form of empirical correlations is given by:

$$\frac{x}{d} = a\left(\frac{y}{d}\right)^{b} \tag{1.21}$$

Where a and b are constants. These correlations give more accurate results for low momentum ratios, as the phenomena of mass stripping and jet deformation cannot be neglected. Experimental studies have shown that a typical value for the drag coefficient of the jet is $C_D = 1.37$ (Ashgriz, 2011).

Instabilities and Droplet Trajectory

When the liquid is injected in the crossflow, the produced instabilities are amplified by the aerodynamic interaction and generate wave oscillations upon the jet. The principal form of wave formations, similar to the jet in static atmosphere, are axisymmetric and eventually lead to the disintegration of the jet (Figure 1.14). Additionally, in low momentum ratios, the shear effect of the aerodynamic forces produces a secondary form of perturbations, known as azimuthal instabilities, which generate undulations upon the jet surface and strip liquid mass into ligaments and droplets (Amini, 2018).

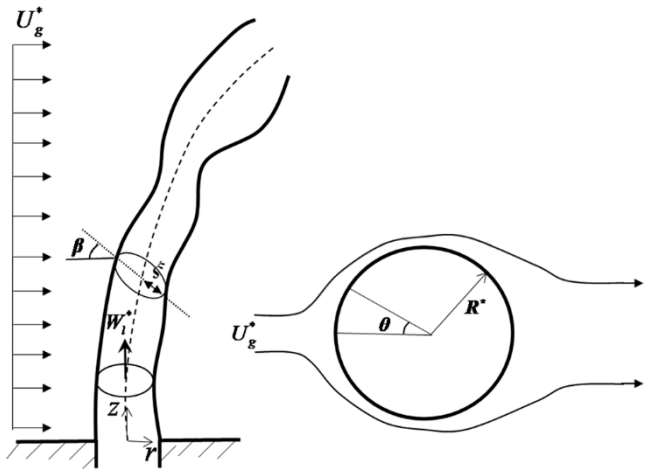

Figure 1.14 Formation of axisymmetric perturbations in LJICF.

The problem is approximated by the perturbation-type analysis as a three-dimensional irrotational flow through the Navier Stokes equations. The resulting equations indicate a discontinuity in the axial and tangential velocity components on the liquid/gas interface, therefore, the solutions are inaccurate on the boundary layer (Amini, 2018). As was discussed above, vortical structures tend to form in LJICF, especially in narrow areas of the jet when the axisymmetric waves are formed. In this case, the vorticity layer is considered to be thin and its effects on the flow are considered minimal, therefore it is neglected (Amini, 2018).

In a similar manner to the static jet, the equations are linearized around an average point. In this case, however, the functions of the flow-field quantities are expanded according to the Fourier modes. The undeformed radius of the jet is R, the initial velocity of the jet is u_j and ω^* is the real-valued frequency of the Fourier series (Amini, 2018). Since there are two wave perturbations on the jet, many different breakup regimes exist in relation to the azimuthal mode. Figure 1.15 shows resulting growth rate spectrums in relation to different azimuthal models, where a is the growth rate of axial perturbations, ω is the Strouhal number $\omega = \omega^* R / u_j$.

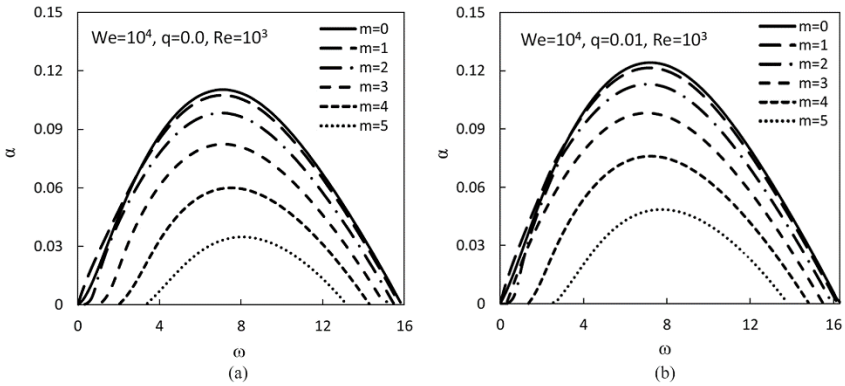

Figure 1.15 Growth rates of instabilities for different azimuthal models (a) q=0.0 (b) q=0.01

Moreover, an important subject for investigation is the trajectory a ligament or droplet follows, after the atomization of the jet. At the breakup point, the formed droplet initially has zero horizontal velocity and only possesses vertical velocity, equal to the initial velocity of the jet, u_j. After the detachment, the droplet losses the vertical velocity and accelerates towards the horizontal direction, as a result of the low mass of the droplet and therefore the low inertia, opposing the aerodynamic forces. Assuming no interaction between droplets and neglecting evaporation phenomena, the differential equations that describe the droplet trajectories are the following:

$$m\frac{d^2x}{dt^2} = A\rho_g\left(u_g - \frac{dx}{dt}\right)^2 C_{dx} \tag{1.22}$$

$$m\frac{d^2y}{dt^2} = -A\rho_g\left(\frac{dy}{dt}\right)^2 C_{dy} \tag{1.23}$$

Assuming spherical droplets with average radius r, the droplet mass is $m = \frac{4}{3}\rho_j\pi r^3$. The frontal area of the droplet is $A = \pi r^2$, and C_{dx} and C_{dy} are the drag force coefficients in the x and y directions respectively. The initial conditions utilized to solve (1.22) and (1.23) are $y|_{t=0} = 0$ and $dy/dt\,|_{t=0} = u_j$. The resulting equations are functions of the y and x direction in relation to time, and by solving the system and eliminating the time variable, the resulting equation for the spray penetration is the following:

$$y = \frac{1}{k_1}\ln\left(1 + \frac{k_1}{k_2}\frac{u_j}{u_g}x\right) \tag{1.24}$$

Where $k_1 = A\rho_g C_{dy}/m$ and $k_2 = A\rho_g C_{dx}/m$. It can be concluded that $k_1/k_2 = C_{dy}/C_{dx}$, noting that the droplet drag coefficients are functions of the corresponding Reynolds

numbers in its direction. By this, it can be written that $k_1/k_2 \propto Re_x/Re_y \propto u_g/u_j$ and therefore $k_1 u_j/k_2 u_g \propto 1$. Additionally, $1/k_1 \propto C_{dy}\rho_g/\rho_j$ and C_{dy} is proportional to u_j and u_g, thus it is expected that $1/k_1 \propto q$. According to these relations, many experimental studies have used the following general logarithmic equation for the penetration:

$$y = Cq^{\alpha} \ln(1 + \beta x) \tag{1.25}$$

Where according to the relations above, it is expected that $\beta \sim 1$ and that α takes values around 0.3 and 0.5 (Ashgriz, 2011). Along with the logarithmic functions, some studies have also used other relations for the penetration of the spray. Aside from the relation, most experimental studies are compatible with $\alpha \sim 0.3 - 0.5$. In the case of a jet in static gas, α was expected to be around 0.5. The possibly lower power of q in this case is reasonable, as the droplets lose their initial velocity almost instantly after their department from the jet column.

Several experimental methods have been developed over the years to provide information about the jet trajectory and spray plume, usually by tracking the upper boundary layer of the spray plume. Shadowgraph technique is the most common method, as it is the simplest form of an optical system observing density fluctuations in a fluid. This technique relates to the reflectivity of a light source when it passes through a dense fluid. The light is deflected in relation to the density of the fluid, generating visible variations of the contrast (Figure 1.16).

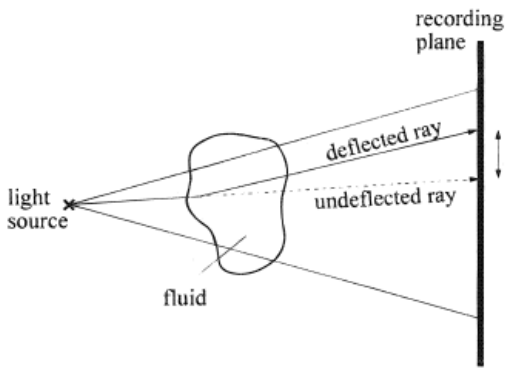

Figure 1.16 Shadowgraph technique illustrated. The light ray is deflected by passing through the dense fluid, creating a brighter spot in the deflected ray point, and a dark spot in the undeflected one (https://thermopedia.com/content/1117/).

Point particle techniques are also utilized to obtain the penetration, by measuring the highest point the droplets can penetrate. Pulse laser imaging is also a useful method, where

droplets are detected using a pulse laser in its frame. The capability of its experimental method differs to a great extent. This causes relatively big discrepancies among experimental studies. Another factor contributing to disagreements in the results, is the test conditions, as they can greatly affect the fluid properties. Turbulence levels of the liquid inside the atomizer and the gas also constitute important parameters, strongly affecting the discrepancies. In addition, the liquid mass reduction phenomena due to stripping can greatly affect the results and should not be neglected. This effect decreases the total liquid mass of the jet and changes the roughness of the liquid surface, therefore, alternating the drag coefficient. Some studies have considered correlations for the Weber number in order to include this effect in the procedure (Ashgriz, 2011).

Jet Deformation and Deflection

Along with the deflection of the trajectory of the jet, the aerodynamic interaction deforms it from a circular to an elliptical cross-section with radii a and b (Figure 1.17b). The deformation of the jet depends on the interplay of the aerodynamic forces along with the surface tension and viscous forces (Ashgriz, 2011). A small element with thickness h is considered upon the jet and ξ is the distance between the geometrical center and the center of mass on the cross-sectional area according to Figure 1.17b. The force balance of the element in the cross-section is the following:

$$F_a + F_v + F_s = m\frac{d^2\xi}{dt^2} \tag{1.26}$$

Where F_a is the inertial, F_v the viscous and F_s the surface tension forces.

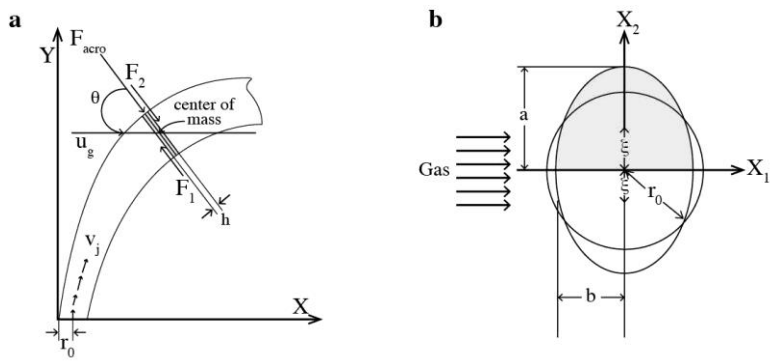

Figure 1.17 (a) Force balance on a small element with thickness h (b) Deformation of the cross-section area of the jet due to crossflow (Ashgriz, 2011)**.**

Inserting the corresponding expression for each force, and including the element deflection angle θ the resulting differential equation governing the jet deformation is:

$$c_1\left(\frac{d^2\xi}{dt^2}\right)+c_2\left(\frac{d\xi}{dt}\right)+c_3=c_4 \tag{1.27}$$

Where,

$$c_1=\frac{1}{2}\pi\rho_j ab, \qquad c_2=2\pi\mu_j ab/\xi^2,$$

$$c_3=\frac{3\pi}{8}\sigma\left[4(1-r^2a^{-2})+\frac{c}{d}\right], \qquad c_4=\frac{1}{2}\rho_g b\left[u_g\cos(\theta)\right]^2$$

In order to obtain results about the deflection angle of the jet, forces are balanced in the x-y plane:

$$F_{aero}\cos(\theta)-F_{shear}\cos(\theta)=m\frac{d^2x}{dt^2} \tag{1.28}$$

Where $F_{aero}=\frac{1}{2}C_D\rho_g u_{rel}A=C_D ah\rho_g\left[u_g\cos(\theta)\right]^2$ is the aerodynamic force upon the element. The area A is equal to $2ah$ and u_{rel} is the relative gas velocity to the element and can be approximated by $u_{rel}=u_g\cos(\theta)$. As it is shown in Figure 1.17a, the total shear force is the result of the two shear forces of the liquid masses in contact with the element. Therefore, it can be concluded that $F_{shear}=F_1-F_2$. This relation provides a small value for calculation purposes, so the shear force can be approximated by $F_{shear}=\pi ab\mu_j u_j\kappa$, where κ is the local curvature of the jet. Assuming the jet velocity is constant along the jet trajectory, and equal to the initial value, for the velocity of the element it can be written that:

$$u_x = u_j \sin(\theta)\,, \qquad u_y = u_j \cos(\theta)$$

Therefore, $dx/dt = u_x = u_j \sin(\theta)$. Inserting this condition to the above equation results in the equation governing the deflection of the jet:

$$\frac{d\theta}{dt} = \frac{F_{aero} - F_{shear}}{\pi \rho_j abhu_j} \tag{1.29}$$

Considering the aspect ratio $AR = b/a$ of the cross-sectional area radii of the jet, it is inferred that, as the jet follows its trajectory it is deformed and the AR decreases over time (Figure 1.18). As the jet gets deformed, the surface in contact with the gas flow changes, thus, the value of the drag coefficient changes. According to this, a correlation can be derived, that provides values for C_D in depenece of AR. For $AR < 0.25$ the shape of the jet becomes very thin, close to a flat plate, and it can be assumed that $C_D \cong 2$. Generally, average values of $1.6 < C_D < 1.7$ are good aproximations and very close to empirical results (Ashgriz, 2011).

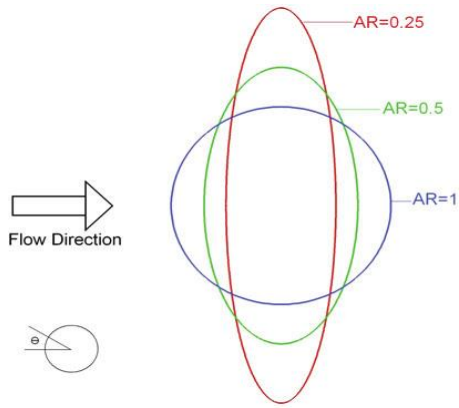

Figure 1.18 Jet deformation over time. AR is decreased as the shape becomes more eliptical (Ashgriz, 2011)**.**

While these correlations provide adequate results, the phenomenon of mass reduction as the jet follows its trajectory is not included, which is the reality in most cases. In situations where the stripped liquid is minimal, neglecting this effect does not produce a large error, however, there are cases where up to 80% of the initial liquid mass can be lost on the trajectory. Mass reduction can be modeled as a decrease in the cross-sectional area of the jet $A = \pi ab$. According to this, it is inferred that when liquid is stripped from the jet the value of C_D decreases, since the contact surface is decreased. Without taking into account

the mass reduction phenomenon, the C_D and therefore the deflection of the jet can be overestimated.

1.4 Spray Characteristics

As it has been discussed, the process of transformation of a liquid jet or sheet into a spray, involves complex dynamic mechanisms. Aside from the atomization process, a well-designed atomizer discharges the droplets into the gaseous atmosphere in the form of a spray structure. For example, the spray produced by a plain-orifice atomizer is characterized by narrow spray angles and evenly distributed liquid mass. This type of spray is commonly referred to as solid. On the other hand, while swirl atomizers may potentially produce a solid spray, the distribution of the droplets tends to concentrate peripherally (hollow cone structure) and the spray angles tend to be larger (Lefebvre & Mcdonell, 2017). According to that, the spray structure may greatly differ, due to the dependance in the method used to atomize the liquid and the device itself. Therefore, in order for a spray to be effective in an application, its characteristics have to be investigated and controlled during the operation. Several attributes of the spray can be observed, and their relative importance depends on the application itself. After the atomization occurs, the behavior of the spray is chaotic in nature, and therefore, there is no deterministic way to investigate them (Lefebvre & Mcdonell, 2017), thus, spray aspects are mainly studied through experimental methods, providing empirical correlations. Additionally, in recent years, simulations have been developed that are utilized alongside the instrumental measurements, to provide a wider picture of the spray behavior after the breakup. In the following segment, spray characteristics and some of their measurement methods are analyzed.

1.4.1 Droplet Size Distribution

The interest of measuring the droplet sizes of a spray has increased in recent years. When a liquid bulk is atomized, a multitude of droplet sizes exist in the spray, mainly depending on the method used in the atomization process. Several ways exist to define the average diameter of the droplets. The Sauter Mean Diameter (SMD or D_{32}) is the most common definition used. SMD is defined as the ratio of the sum of D^3 to the sum of D^2 of the

measured droplets. Other commonly used representatives of the droplet diameter are the Arithmetic Mean Diameter (D_{10}), the Volume Median Diameter (D_{30}) and the de Brouckere Mean Diameter (D_{43}). After the diameters of the droplets are measured the droplet size distribution is obtained and the average diameter is defined according to one of the representative definitions.

There are many instrumental techniques that can be utilized to provide information about the size distribution. The method used to measure the droplet sizes heavily depends on the application itself in order to provide adequate results (Lefebvre & Mcdonell, 2017). One typical method is the impaction technique, in which the droplets are collected on slides for measurement. Depending on its size, a droplet impacts a solid surface with different force and those that do, are considered as solid particles. Some droplets may fail to impact the surface or follow a different trajectory. In conclusion, the droplet size distribution results from measured inertia differences (Lefebvre & Mcdonell, 2017). Furthermore, high speed imaging techniques, such as microphotography, cinematography, and holography, can also be used to collect images of the spray for the measurement of the droplet sizes through further processing. In addition, laser diagnostic methods have been developed in recent years for measuring droplet sizes along with the velocity distribution.

1.4.2 Dispersion

Dispersion is the characteristic that measures the plentitude of liquid within the spray structure. According to this, the dispersion can be defined as the ratio of the volume of the entire spray to the liquid volume contained within it. High dispersion values imply a sparse spray structure, promoting mixing and evaporation phenomena, while low dispersion values constitute a more solid spray, as it is the case with plain-orifice atomizers (Lefebvre & Mcdonell, 2017). In the case of swirl atomizers, the dispersion values can vary, mainly depending by other spray characteristics such as spray angle, average droplet size, and drop size distribution, while the physical properties of the liquid are of lesser importance.

1.4.3 Penetration

Penetration is defined as the maximum vertical distance the spray advances, either in quiescent environment or in crossflow. In the case of static atmosphere, penetration can be described entirely as a function of time. Penetration depends by two opposing forces, the kinetic energy of the initial jet and aerodynamic phenomena. While the initial velocity of the jet is usually high, as atomization phenomenon progresses, the contact area of the liquid to the surrounding gas increases, amplifying aerodynamic interaction and increasing the deceleration of the droplets. Eventually, when the velocity of the droplets is low enough, their movement and trajectory is entirely governed by gravity and the movement of the gaseous phase (Lefebvre & Mcdonell, 2017). Generally, solid sprays penetrate more than sparse well-atomized sprays, as in the latter, the surface area in contact with the gas is larger, increasing the aerodynamic interaction. According to this, it is inferred that penetration depends on the dispersion of the spray. After the atomization, the first droplets transmit their energy locally to the surrounding gas, which tends to follow their trajectory, providing less resistance, hence, these droplets penetrate more (Lefebvre & Mcdonell, 2017). In the case of crossflow, the trajectory of the droplets will bend in the direction of the gas flow, due to the aerodynamic interaction between droplets and gas, with the principal parameter being the gas to liquid momentum ratio. The aerodynamic interaction in this case is increased, and thus, the droplets lose their kinetic energy faster. Generally, sprays in crossflow have less penetration than the corresponding spray in quiescent atmosphere. High-speed imaging is the most efficient way to identify the spray penetration, as it is a macroscopic characteristic.

1.4.4 Spray Angle and Coverage

As the spray travels through the gaseous medium, the aerodynamic interaction causes the boundary layers of the spray to bend and deform. This provides an issue with the definition of the spray angle since the actual angle increases as the spray penetrates through the gaseous atmosphere. To overcome this problem, the spray angle or cone angle, is usually defined as the angle of two straight lines with the same starting point at the discharge orifice, that osculate the spray boundaries at some specified point down the spray stream

(Lefebvre & Mcdonell, 2017). The coverage of the spray is the cross-sectional area that it covers, on a specified distance from the nozzle. Spray coverage is heavily depended by the spray angle. However, with the way spray angle is defined, the aerodynamic interaction is neglected, resulting in an overestimation of the coverage of the spray. Figure 1.1 illustrates the spray angle and theoretical coverage for a fixed spray distance. As the spray distance increases, the cone angle diverges from the actual angle of the spray, and the error between the theoretical and the actual coverage increases.

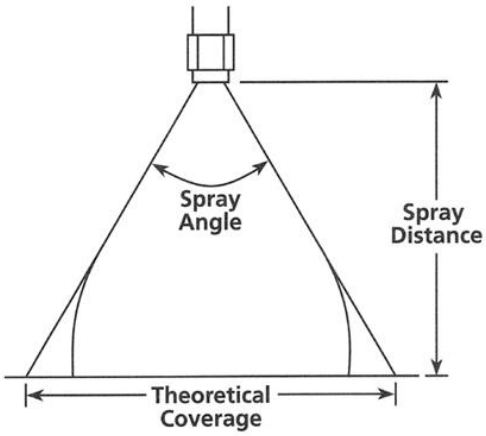

Figure 1.19 Cone angle and theoretical coverage of a spray for a specified distance (https://www.steinen.com/engineering-information/).

A usual method to measure cone angle is to image the spray in a fitting magnification. Another common technique is the usage of probes to define the spray profile, at several distances. The probes can be placed in equal distances from the center of the spray and moved until they collide with the edges of the spray. For swirl nozzles, linear variable displacement transducers are used to determine the probe positions. The importance of spray angle has produced efforts to generate standard protocols about the determination of spray angle. Such protocols have not been established, which indicates the difficulty in quantifying the measurement of spray angle (Lefebvre & Mcdonell, 2017).

1.4.5 Spray Pattern – Liquid Distribution

The pattern of the produced spray refers to the distribution of the liquid within the spray structure. In most applications, the pattern needs to be symmetrical while changes in the

symmetry can affect the operation negatively. For instance, in spray drying an asymmetrical spray pattern results in insufficient liquid/gas mixing, which in return, degrades the quality of the final product. Symmetrical spray patterns are also important in combustion engines. The fuel in a combustion engine needs to be uniformly distributed, as it promotes high efficiency combustion and less pollutant emissions. Minor pattern asymmetries are hard to be detected by visual methods, while their negative effects on the operation could be considerable (Lefebvre & Mcdonell, 2017). According to this, quantitative determination of the spray pattern needs to be achieved by instrumental measurements for the design and operation of the atomizer. Spray pattern can be measured both radially and circumferentially in order for the liquid distribution to be defined. The apparatuses used to obtain the liquid distribution are called patternators.

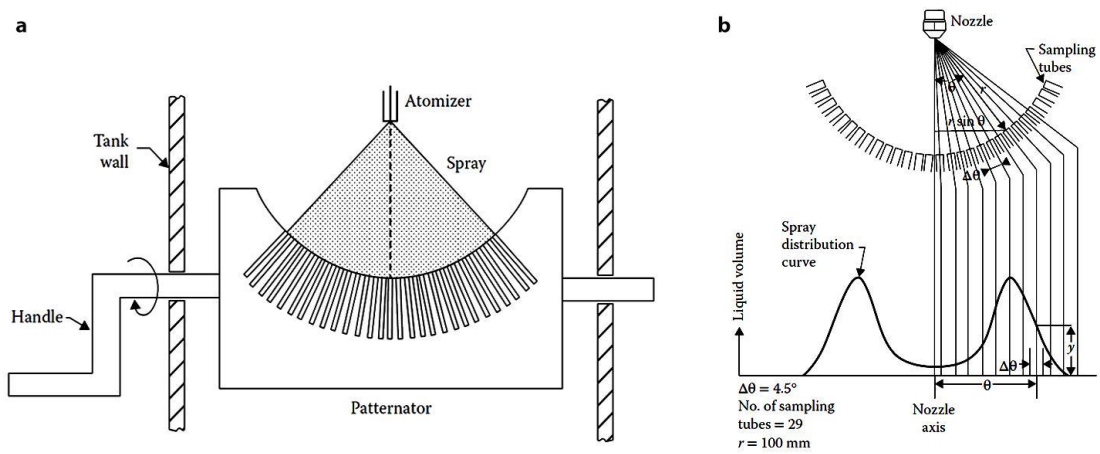

Figure 1.20 (a) Schematic of patternator measuring radial liquid distribution (b) Device standards and resulting distribution graph (Lefebvre & Mcdonell, 2017).

Chapter 2 Experimental Set-up: Equipment and Procedures

In this section, the experimental arrangement, procedures, and methods undertaken in this investigation are presented, along with the devices and equipment that are utilized. The experiments were conducted in the Fluids and Turbomachinery Lab of the Department of Mechanical Engineering, University of Thessaly. The experimental investigation involves the injection of a spray by an air-assist atomizer, into an airstream crossflow, produced by a blower. The exit of the blower is connected with a circular duct, that guides the airstream to the injection point. The liquid flowrate is achieved by compressed air and is controlled by a flowmeter, that adjusts the flowrate. The air flowrate is controlled from the inverter of the blower, regulating the frequency of the device. Both the liquid and air flows need to be calibrated, for the actual flowrates to be derived. In order to obtain the data for subsequent investigation, the shadowgraph technique is employed. With according processing of the acquired data, the spray characteristics can be obtained, such as the spray angle, the penetration, the CBL and the trajectory.

2.1 Experimental Conditions

The gas and liquid properties are presented in Table 2.1. The liquid used is deionized water as an alternative of hydrocarbon fuels. Ambient air is utilized as the crossflow gas. The resulting spray shape is of elliptical shape, and thus the results should differ depending on the orientation. The following convention is used; when the major axis of the ellipse is normal to the crossflow axis, the atomizer is considered to be at $\theta = 0^o$ and when the major axis is parallel to the crossflow, the atomizer is at $\theta = 90^o$. Both of those orientation cases are investigated.

Table 2.1 Fluid properties and ambient conditions.

Properties	Purified Water	Ambient Air
Density ρ (kg/m^3)	1000	1.204
Viscosity μ (Pa·s)	10^{-3}	$1.83 \cdot 10^{-5}$
Surface Tension σ (N/m)	$7.28 \cdot 10^{-2}$	-
Temperature T (°C)	20	
Ambient Pressure P (bar)	1.01	

The atomization conditions are summarized in Table 2.2. The maximum Reynolds number the liquid flow achieves is about 2700, which is considered to be in the transitional flow regime. The extend of turbulence levels may affect the results in this situation. This is investigated in the section of 3.1. The atomizing air takes the values of 8,9 and 11 L/min. However, in the case of the lowest liquid supply the case of 11 L/min is not taken into consideration, due to the excessively dilute spray produced. Another important parameter is the gas-to-liquid mass flowrate ratio (GLR) which indicates the level of atomization in twin-fluid atomizers.

Table 2.2 Atomization conditions (liquid and atomizing air).

Flowmeter	ΔP_l (bar)	Q_l (cc/min)	U_l (m/s)	Re_l	We_l	Air (L/min)			GLR		
20	0.08	23.20	2.9	1201	48.40	8		9	0.41		0.47
30	0.14	32.10	4.1	1661	92.60	8	9	11	0.30	0.34	0.41
40	0.22	41.75	5.2	2161	154.6	8	9	11	0.23	0.26	0.32
50	0.33	52.25	6.4	2704	229.1	8	9	11	0.18	0.21	0.25

In Table 2.3, the crossflow conditions are summarized. The most important data from the crossflow conditions is the velocity of the air flow. This governs the momentum of airflow, and consequently the liquid-to-gas momentum flux ratio ($q = \rho_j U_j / \rho_g U_g$), which indicates the level of deflection of the jet/spray. The different values of q are observed in Table 2.4.

Table 2.3 Crossflow Conditions.

Frequency	U_g (m/s)	Q_g (m^3/s)	Re_g (×10^4)	We_g
10	2.0	0.021	1.51	0.03
20	4.1	0.045	3.18	0.11
30	6.1	0.066	4.73	0.25
40	8.1	0.087	6.22	0.44
50	10.0	0.108	7.72	0.68

Table 2.4 Momentum flux q values, for every crossflow case.

$U_l \backslash U_g$ (m/s)	2.0	4.1	6.1	8.1	10
2.9	1746	416	188	106	70
4.1	3490	831	375	213	140
5.2	5615	1336	604	342	225
6.4	8505	2024	914	519	340

Considering the combinations of liquid, crossflow air, and atomizing air cases, results in a number of 66 total study cases (including the zero crossflow cases).

2.2 Experimental Arrangement

The experimental set-up is illustrated in Figure 2.1. Compressed air is provided from the main air supply of the lab and is with a Y fitting in two branches: the pressurization of the liquid supply in the pressure vessel and for the atomizing air of the atomizer. The blower and the inverter can be observed, along with the circular duct the former is connected to. The duct is supported with 3D printed footings. The atomizer is mounted upon a custom 3D printed base at the exit of the duct. Additionally, the flowmeter controller of the liquid can be observed, and the pressure sensor in the chamber, upstream from the atomizer.

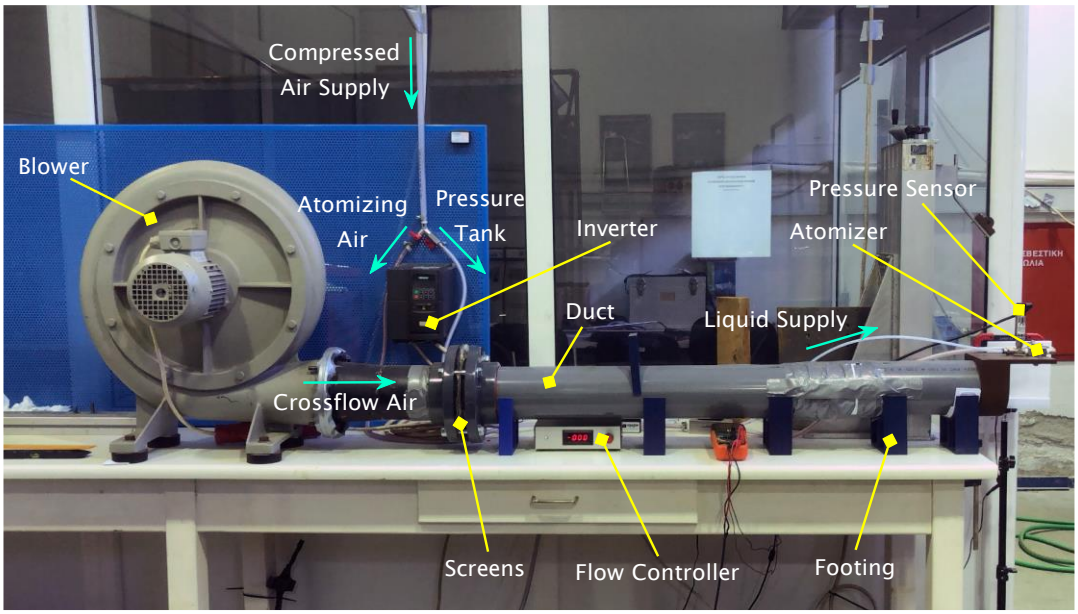

Figure 2.1 Experimental Arrangement.

2.2.1 Blower and Circular Duct

The blower is a Siemens D-97615 model, and the frequency of the motor is regulated through a Siemens Micromaster 420 inverter between 0-50Hz (Figure 2.2). The duct connected to the blower, guiding the airflow, is of total length of 1.5m and 12cm in diameter. The crossflow velocity profiles need to be straight and uniform, in order to provide repeatable results. For that purpose, a total of 7 screens and 1 honeycomb are placed inside the duct to restrict velocity fluctuations and straighten the flow. The screens improve the uniformity of the velocity profile while the honeycomb straightens the flow and reduces turbulence levels, eliminating vortical movements (Bradshaw & Pankhurst, 1964). A triple screen is placed at about 30cm from the exit of the blower and the honeycomb is placed at 70cm from the triple screen. The honeycomb length is about 6cm, and the cells are of circular shape with a diameter of 5.5mm. Following the honeycomb, in a distance of 12cm, the four remaining screens are placed with a distance of 3.5mm between them. With this arrangement, swirl motions produced by the blower are eliminated, resulting in a laminar uniform flow.

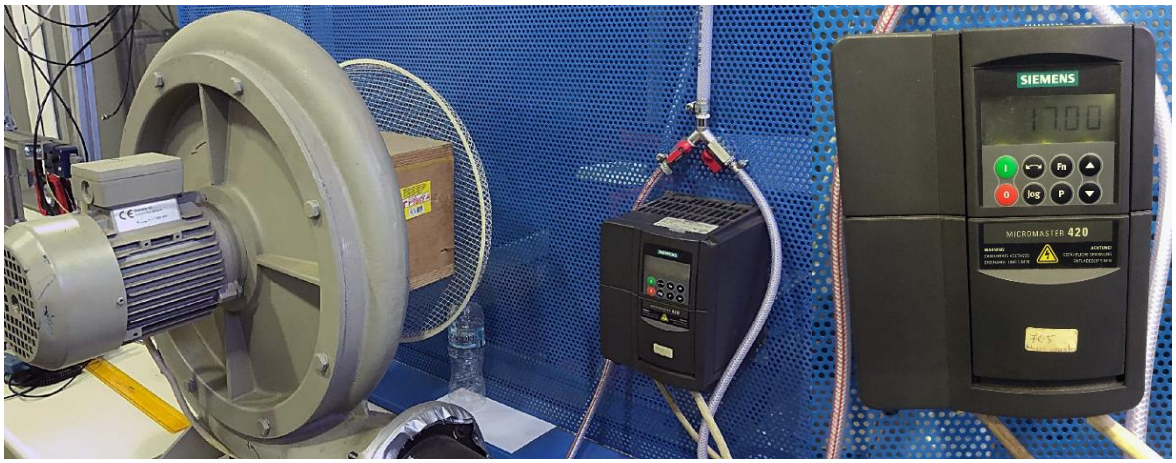

Figure 2.2 Blower and inverter system.

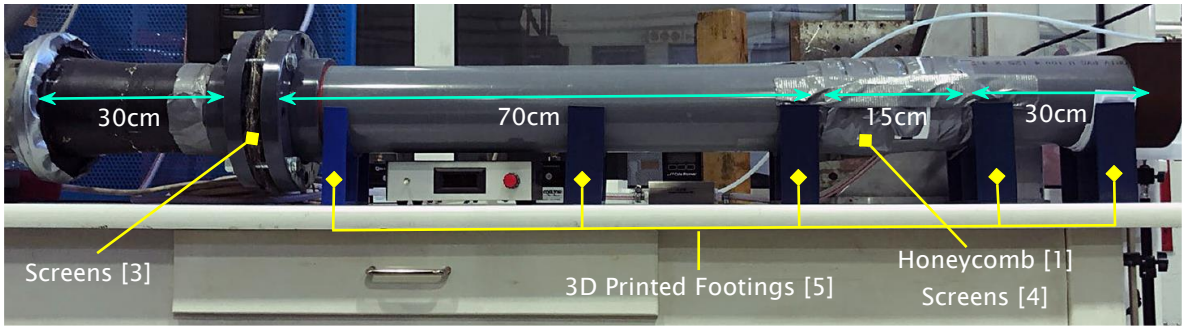

Figure 2.3 Configuration of the duct.

2.2.2 Atomizer and Liquid Supply

The atomizer used in this study, is a Spraying Systems B1/4J-316SS external mixing, air-assist atomizer, with an orifice diameter of 0.41mm. For the restrain of the device, a 3D printed custom base is used, which is mounted to the end of the circular duct. The atomizer, as an air-assist type, discharges the liquid from the main, centrally located orifice and atomizes the liquid utilizing the momentum of compressed air, ejected from the sides of the interface of the device. The configuration is illustrated in Figure 2.4. The airflow of the atomizer is measured through a Cole-Parmer Digital flowmeter (Figure 2.4), in Standard Liters Per Minute (SLPM).

The liquid supply is provided by a pressurized vessel, utilizing the main compressed air supply of the lab. The liquid is placed in a Spraying Systems 22140 pressure tank illustrated in Figure 2.5, operating under an air pressure of 2 bar. The tank is connected with a plastic tubing for the delivery of the liquid to the atomizer. The pressure inside the tank is adjusted by a R27 Precision Pressure Regulator. Along the tubing, an Entegris 6500-T2-F02-B06-M-P2-U1 controller is placed to regulate the liquid flow, and at the end of the tubing, upstream from the atomizer in close distance, an Omega XM319-3.5A10V pressure transducer is placed, for the measurement of the actual discharge pressure (Figure 2.4). The liquid flow regulator controls the liquid flow by adjusting the pressure inside the tubing, as the liquid flow is pressure driven, and therefore $Q = Q(\Delta P)$.

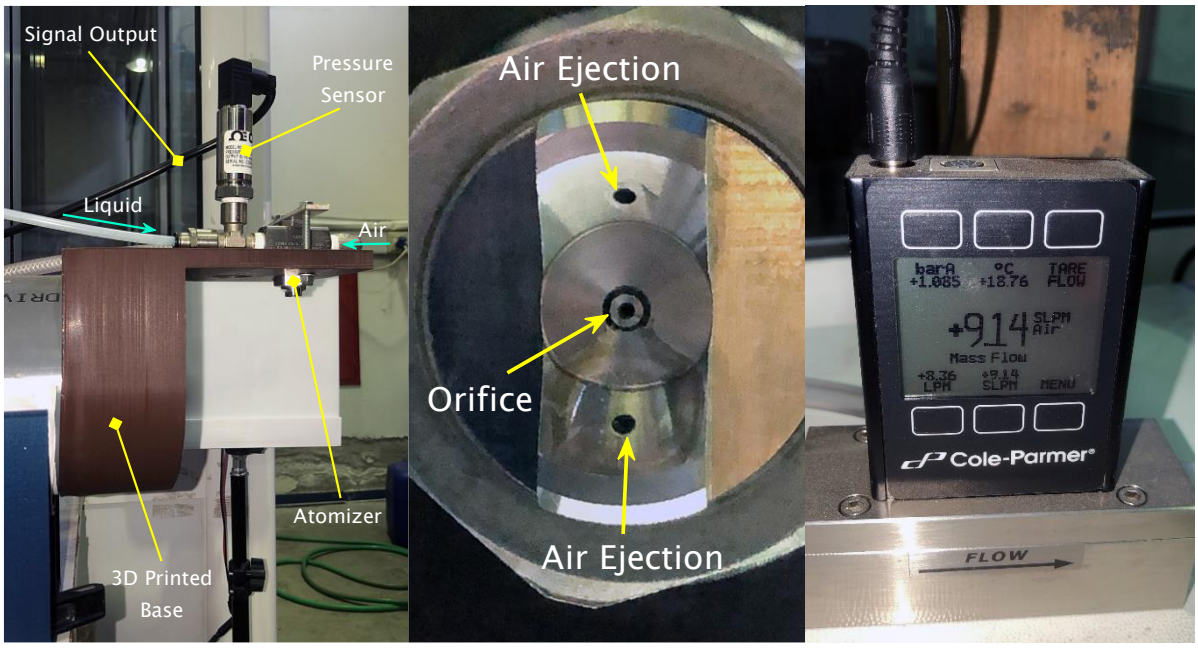

Figure 2.4 Atomizer section: configuration, atomizer frontal view and digital flowmeter.

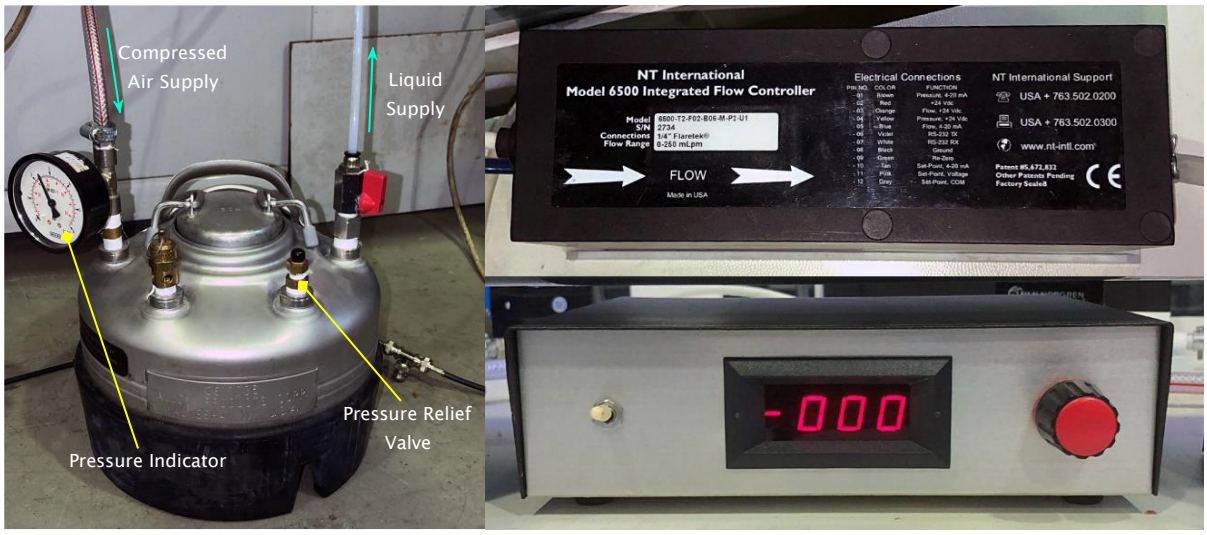

Figure 2.5 Liquid Supply: Pressure Tank and Flowmeter.

2.2.3 Shadowgraphy: Camera and Illumination

The characteristics of the spray are investigated using shadowgraphy. Shadowgraphy is a density-based technique. Density-based techniques visualize flow phenomena based on variations of the fluid density, and therefore, of the index of reflection of light. Along with shadowgraphy, several optical flow visualization techniques have been developed over the years, such as the Schlieren method, the Moiré deflectometry, interferometry, and optical tomography. The distinctive feature of shadowgraphy is the implementation of pointwise light source, along with a diffusive background for uniform illumination. The purpose in this study is to capture the liquid of the spray and investigate its properties through further image processing. The transmission of light through the air in absence of liquid, results in uniform background intensity as it is captured by the camera. In presence of the liquid, the light is deflected from the original direction due to the density difference of the two fluids, resulting in relatively lower intensity in the specific area. The resulting image contains visible contrast variations, which indicate the location of the liquid. The typical instrument layout in shadowgraphy method is illustrated in Figure 2.6.

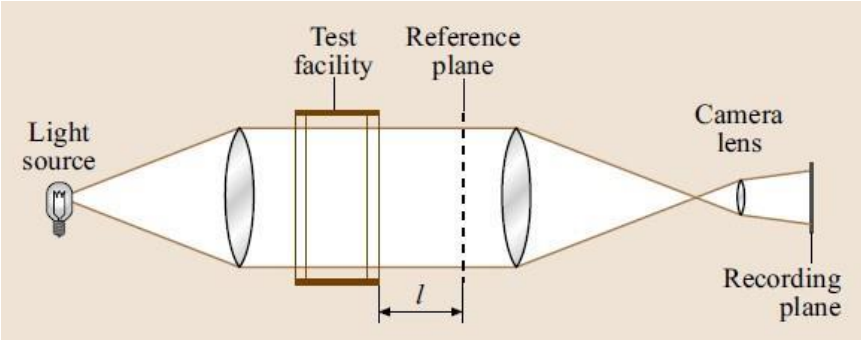

Figure 2.6 Typical Shadowgraph method arrangement (Cameron Tropea et al., 2007)**.**

In terms of data collection, a variety of imaging detectors may be used, most common being CCD and CMOS cameras. The type and model of camera utilized, directly relates to the demands of the application itself. In this particular experiment, a CCD camera is employed. CCD stands for Charged-Couple Device. These imaging detectors operate by implementing a integrated circuit etched upon a surface of silicon material, forming an array of linked capacitors, which constitute the pixels of the device (also called cells or elements). When the sensor is illuminated, the impact of light rays upon its elements, generates electric charge proportional to the radiative energy. The photosensors are separated with a potential barrier, and by utilizing shift registers, employing an appropriate sequence of potential changes, the charges can be transmitted across the sensor. The charges are subsequently transferred to the readout register, generating voltage which conducts electricity (analog signal). The analog signal is amplified and converted to digital signal by the means of an A/D (analog-to-digital) converter. During the total period of the charge transmission, the sensor is isolated from the light source. The time interval of charge accumulation, when the sensor is illuminated, is called the exposure time.

Several archetypes of charge transfer are implemented in CCD devices, most common being the frame and interline transfer. Frame transfer method implements an illuminated capturing array and a light-isolated storage array of pixels. After the charges are generated, the capturing frame is isolated, and they are collectively transmitted from the entire capturing frame to the storage frame. From then, the capturing frame is illuminated again, while the storage frame proceeds to readout the charges row by row, and then continue to be converted to digital signal. The dark time, when the capturing frame is isolated, is approximately equal to the readout time of one row. Another frame transfer architecture is

the full-frame, which works in absence of the storage frame, but it is not widely used, since frame transfer requires lower transmission time. By this procedure, it is inferred that frame transfer sensor are unsuitable for continuous illumination, and the frame rates during operation are relatively low. On account of that, the most used capturing method is the interline transfer. Interline transfer employs storage cells between photosensors. After the exposure time, the charges are transferred to the storage cells, and proceed to the readout register. Since the entirety of the charges are collected by storage cells simultaneously, the pixels require much lesser isolation time, and thus, exposure time can be higher than a full-frame transfer sensor. A comparison of frame, full-frame and interline transfer is illustrated in Figure 2.7.

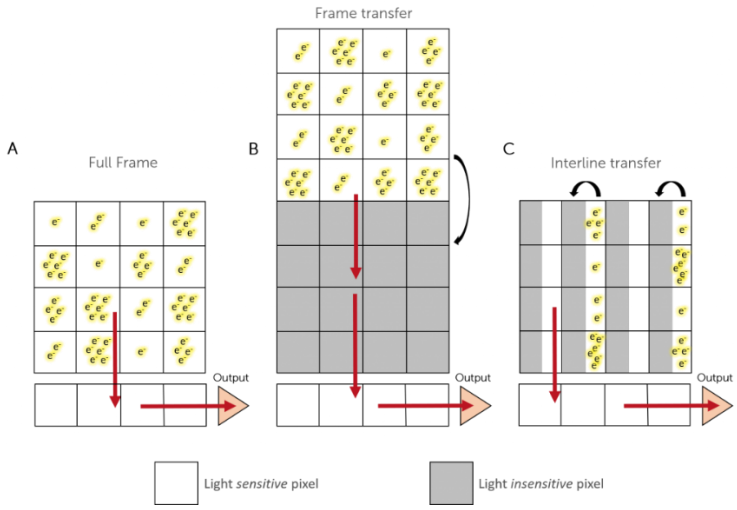

Figure 2.7 CCD sensors, charge transmission architectures: A) Full-frame transfer B) Frame transfer C) Interline transfer.

In the case of CMOS sensors, the conversion of charge to voltage and the voltage amplification, occurs inside the pixels. These pixels are known as Active Pixel Sensors (APS) and contain additional circuits and preamplifiers. Since the charges are being processed by their corresponding APS simultaneously, there is no need for charge transmission and the voltage is retrieved with specific selection circuits (mainly rolling and global shutter). According to that, a CMOS sensor is able to readout a part of the APS array without any speed loss, in contrast to a CCD sensor which requires charge transfer mechanisms.

The CCD camera used in the experiment is the model TSI Powerview plus HS-200 with a SIGMA 70-200mm F.2.8 APO lens attached to it. The charge transmission architecture is an

interline transfer. The camera is mounted on a tripod (Figure 2.8). The electronic triggering is generated by a Laser Pulse Synchronizer Model 610036 (Figure 2.8) connected to a control PC, operated by the TSI Insight 3D program. The camera can capture a maximum resolution of 2048x2048 pixels with a 12-bit dynamic range, although in this investigation, a 512x512 pixel frame is used, in order to minimize the image size while maximizing the illumination. The camera operated at 6fps and an exposure time of 1μs. A LED light of 450 lumens, model XW750 Dekton, is placed directly behind the nozzle of the atomizer to illuminate the frame for the capturing. The LED light is mounted upon a tripod, while a translucent background is placed in front, in order to uniformly distribute the luminosity and protect the camera from high intensity spots. The arrangement of the camera is illustrated in Figure 2.8.

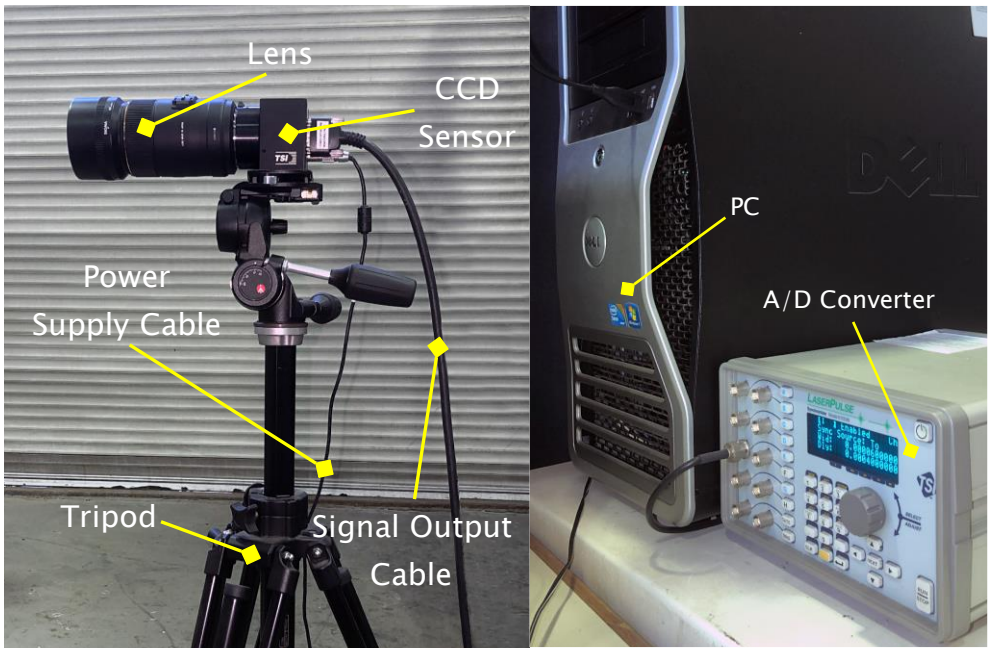

Figure 2.8 CCD camera with the tripod and A/D signal converter with the PC.

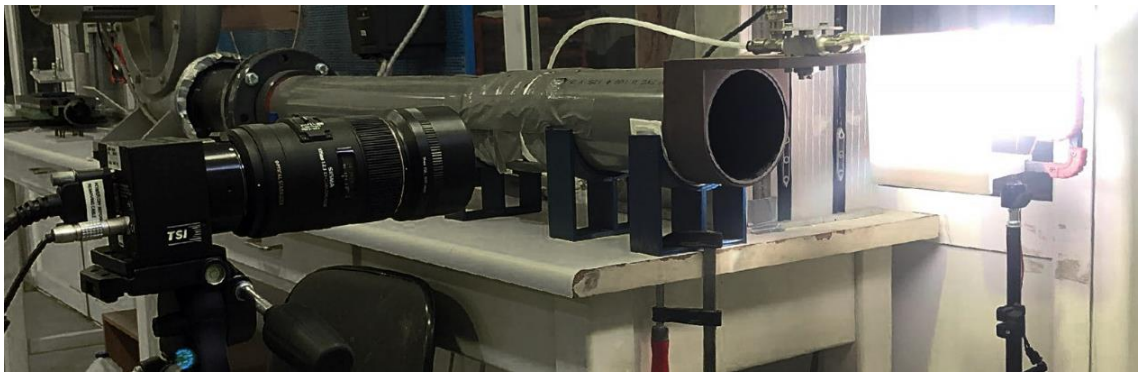

Figure 2.9 Shadowgraph experiment arrangement.

The camera is placed directly across off the injection region, so that both the nozzle and an adequate part of the spray are imaged. The deflection of the jet/spray needs to be accounted, therefore, the nozzle in the camera frame has to be horizontally in opposite direction of the airflow (Figure 2.10). Additionally, the lens should be horizontal, parallel to the ground, and is adjusted with a level for that purpose. It is also critical, that the duct and the camera are parallelly placed and horizontal, in such a manner that the zero crossflow condition data result in zero deflection of the jet after the processing. Otherwise, a slight initial angle of the jet can be observed (either positive or negative), that influences the results.

Figure 2.10 Background Images of the camera frame, for the nozzle orientation at 0° and 90° respectively.

A total of 500 images are collected for each case study. Through subsequent processing using Octave software, statistical data and correlations are obtained for the spray characteristics. Since the spray characteristics are space-dimensional properties, are initially provided in terms of pixels of the image. In order to convert the results in physical dimensions, the background frame is calibrated by measuring a certain interval upon the image with a ruler, and thus, the mm/px coefficient is obtained (Figure 2.11). The calibration procedure is repeated every time measurements are taken, since both the positions of the camera (especially in the direction of the axis vertical to the background) or the atomizer may slightly change. In that case, a different coefficient will emerge from the calibration. This procedure is undertaken prior to the data collection, and therefore, it is important that the relative position of the camera and the atomizer during the measurements, remains the same, which is the main reason the restraint of the duct and the damping of the vibrations is of major concern.

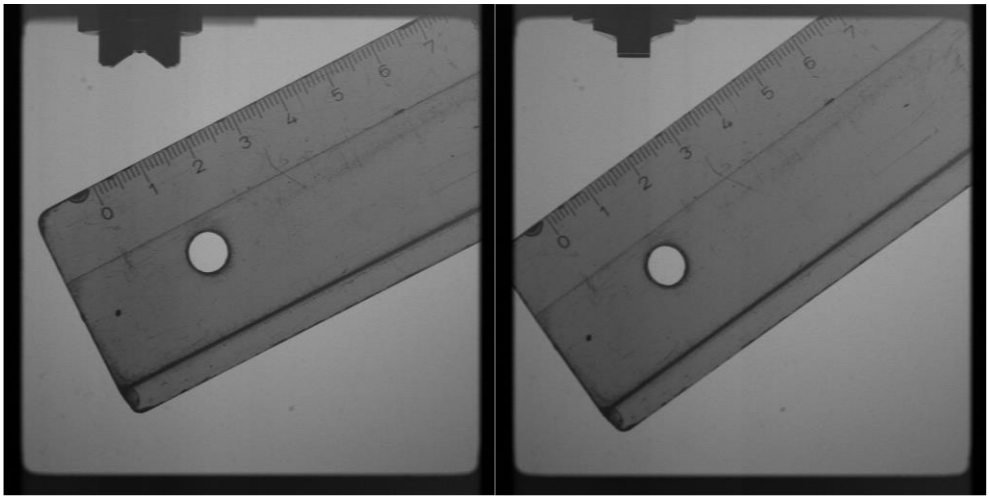

Figure 2.11 Background Image calibration (0° and 90°)

2.3 Calibration Procedures: Liquid Supply and Air Crossflow

2.3.1 Liquid Supply Calibration

The calibration of the flowmeter is important in order to obtain insight about the velocity and flowrate of the liquid. This information is of major concern, since a multitude of important parameters, governing many physical processes in the phenomenon, depend on the initial momentum of the liquid bulk. Essentially the trajectory, dispersion, spray angle, deflection, CBL, and many more spray characteristics variate with regard to the initial liquid momentum.

Methods and Procedure

In order to calibrate the flowrate, liquid sample is collected with a volumetric tube for a certain time interval, for each liquid flowrate case. Considering the flow regime to be steady-state, the mass supply, and hence the volumetric supply should be constant in time. Therefore, mass flowrate can be calculated as: $\dot{m} = dm/dt \Longrightarrow \dot{m} = \Delta m/\Delta t$. The sampling time is about 2 minutes, and the collected liquid mass is measured by a scale (Figure 2.12), after subtracting the weight of the volumetric tube. Following the calculation of the mass supply, the volumetric supply, the velocity and the Reynolds number can be obtained.

Figure 2.12 Electrical Scale.

For the estimation of the pressure drop, the pressure sensor upstream of the atomizer is utilized. The signal output of the sensor is provided in volts. Initially, the pressure is measured with zero liquid flowrate, and the result is the atmospheric pressure since these is no flow inside the chamber. The atmospheric pressure is subtracted by the pressure value of each case to obtain the pressure difference of the liquid injection. With knowledge of the pressure difference, the discharge coefficient is obtained which is also a parameter of major importance. From the values of volumetric supply and pressure differential for each case, the correlation $Q = Q(\Delta P)$ can be obtained.

Results and Discussion

The correlation $Q = Q(\Delta P)$ illustrated in Figure 2.13. It can be observed that it produces accurate and repeatable results. The trendline of every case is approximately the same, and the supply values can produce a maximum error of 5%. It is worth noticing that the standard deviation values of the average supply (calculated for every measurement date), are increasing for decreasing average pressure drop, as a consequence of the flowmeter's operation. The maximum deviation can be observed at 0.08bar (20 flowrate) and is about 5%, while in the case of 0.33bar (50 flowrate) is about 0.2%. The deviations of the average volumetric supply are expected to be corresponding to the pressure drop values. In Table 2.5, volumetric flowrate values, and their corresponding standard deviation percentages are presented. Volumetric supply deviations are about the same range in comparison to the pressure drop ones. According to this, it is inferred that a maximum uncertainty of 5% is expected in the final results, for the smallest volumetric supply case, while for higher liquid flowrates the uncertainty reduces significantly and drops to below 1% for the maximum liquid flowrate.

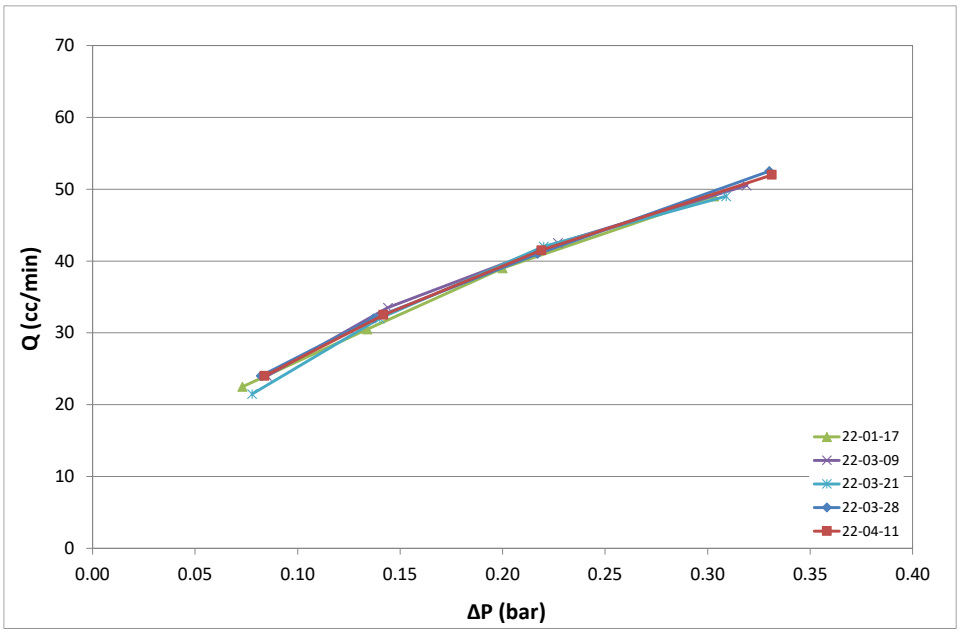

Figure 2.13 Volumetric supply calibrated with the average pressure differential $Q = Q(\Delta P)$.

Table 2.5 Pressure difference and volumetric supply average values, with their corresponding standard deviations.

Pressure Differential (bar)	Volumetric Liquid Supply (cc/min)	Daily St.D. of the Liquid Flowrate
0.080	23.20	4.44%
0.140	32.10	3.02%
0.220	41.75	1.34%
0.330	52.25	0.48%

Obtaining insight about the pressure drop and volumetric supply values, for a liquid with ρ density and μ viscosity, the actual initial velocity and Reynolds number of the liquid at the exit of the orifice is calculated for every case; $u = \frac{4Q}{\pi d^2}$, $Re = \frac{\rho u d^2}{\mu}$,where d is the orifice diameter. Afterwards, the discharge coefficient, can be calculated accordingly:

$$C_d = \frac{Q}{Q_{ideal}} = \frac{uA}{u_{ideal}A} \xRightarrow{Bernoulli} C_d = \frac{u}{\sqrt{2\Delta P/\rho}} \Leftrightarrow C_d = u\sqrt{\rho/2\Delta P} \tag{2.1}$$

The velocity and Reynolds number values produce exactly identical standard deviations with the volumetric supply, since the former are multiples of the latter with constant multipliers. The average discharge coefficient values on the other hand, depend both on the velocity,

and subsequently on the volumetric supply, and the pressure difference, which both constitute measurement variables. As it can be observed at Table 2.6, the maximum deviation of the discharge coefficient is about 3% which is negligible. Figure 2.14 Illustrates the discharge coefficient in relation with the Reynolds number.

Table 2.6 Discharge coefficient average values and standard deviations.

Discharge Coefficient	Daily Standard Deviation
0.73	2.99%
0.77	1.87%
0.79	0.70%
0.81	0.58%

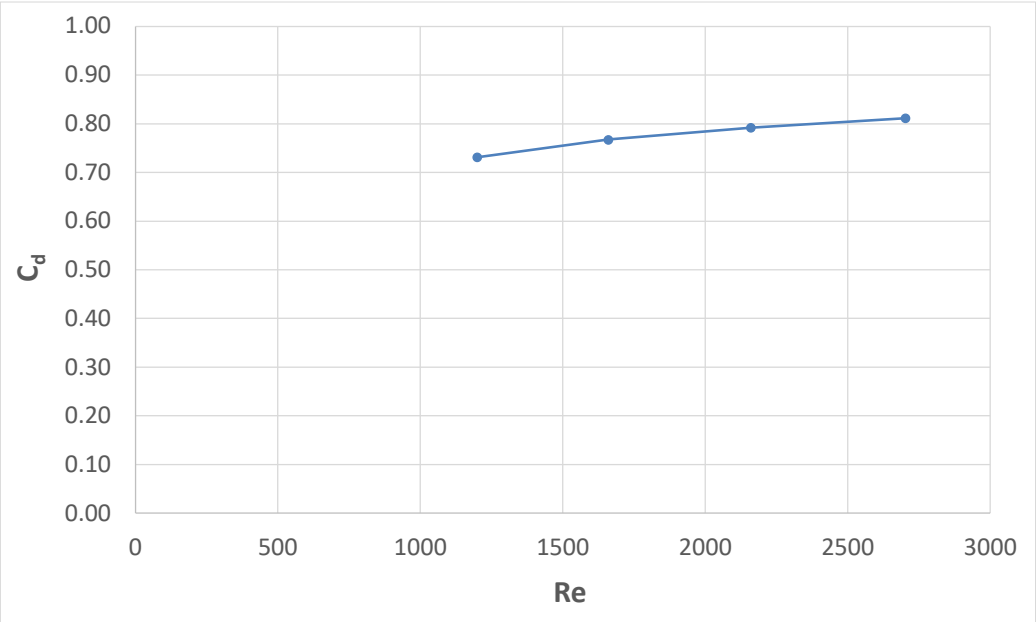

Figure 2.14 Discharge coefficient in relation with the Reynolds number.

2.3.2 Crossflow Air Calibration

In the crossflow cases, the behavior of the air is of major concern. The average velocity, the velocity profile, and the airflow regime are the main variables governing the aerodynamic

interaction with the liquid. Variations in the interplay of the aerodynamic forces, can greatly affect atomization of the liquid, as well as the spray behavior after the atomization occurs (trajectory, boundary layers, dispersion, spray angle).

Methods and Procedure

The objective of the airflow calibration involves the determination of the velocity profile at the exit of the duct. For this purpose, a TSI VelociCalc anemometer is utilized (Figure 2.15), that provides the exact value of the airflow in m/s. The device is based on the hot-wire anemometry method. This technique is widely implemented for the quantification of air velocity, in subsonic and supersonic flows. The operation principle of this technique relies on the dependance of the specific electrical resistance of a conductor, on its temperature: $R(T) = R_o(1 + \alpha T)$, where α is a constant and R_o the resistivity at standard conditions. The sensor element is a conductor of cylindrical shape (Figure 2.15) and possesses low thermal inertia, in order to provide rapid dynamic response. Most common operating archetypes involve the constant current (CCA), constant temperature (CTA), and constant voltage (CVA) techniques. This apparatus employs the CTA method. When the sensor is exposed to a gas stream, convection heat transfer decreases the temperature, hence the resistivity of the sensor. The device operates with a control feedback loop, which provides the conductor with a corresponding voltage, which produces heat, in order to stabilize the resistivity of the sensor at its initial value. The amount of voltage required to stabilize the resistivity, relates to the convective heat transfer coefficient with a simple energy balance on the element. The convective coefficient is governed by the velocity of the air stream. Therefore, an indirect relation between the voltage and the velocity exists. The device utilizes this relation to provide the velocity of the air stream at a specific point.

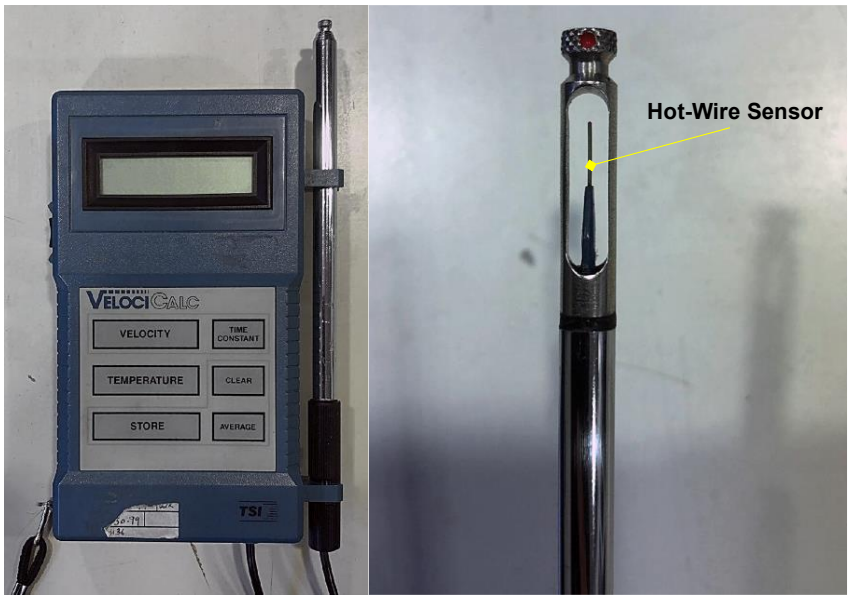

Figure 2.15 Anemometry device and the hot-wire sensor.

The hot-wire sensor is placed and restrained, with a 3-D printed base, on a table with one degree of freedom, for movement at the vertical axis. The sensor is placed directly at the end of the duct, at the vertical axis which intersects the center of the cross-sectional area of the duct. In order to obtain the velocity profile, measurements are taken from the highest point which coincides with the duct's wall, to the lowest corresponding one, with a specific step. The flow regime is considered to be 1D and radially distributed, thus for every given point at the duct's area, $U = U(r)$. Following the acquisition of the velocity profile, the average velocity can be obtained, by mean of numerical integration. There are two basic approaches in this procedure: measuring the velocity along constant intervals or with intervals that correspond to equally devided sub-areas, as illustrated in Figure 2.16.

If A is the total cross-sectional area of the duct, for N number of measurements, the total circular area is divided into N equal sub-areas with values of $A_N = A/N$. From the first measurement at the center, for $r = 0$, the area is of circular shape, therefore:

$$A_o = \pi r_o^2 = A_N = A/N \Longrightarrow r_o = \sqrt{A/\pi N} \tag{2.2}$$

The second sub-area is of ring shape, enclosed by the initial radius r_o and the upcoming radius r_1. Obtaining the value of the former, the latter can be derived:

$$A_1 = \pi(r_1^2 - r_o^2) = A_N = A/N \Longrightarrow r_1 = \sqrt{A/\pi N + r_o^2} \tag{2.3}$$

Obtaining the radius r_1, the next radius r_2 can be obtained by the same method, and so forth. According to this, it can be inferred that:

$$r_j = \sqrt{A/\pi N + r_{j-1}^2} \tag{2.4}$$

Where, $j = 1,2, \dots, N-1$. The representative distance for the measurement for a specific area, is defined to be the semi-sum of the two radii of the ring area; $r = \frac{r_j + r_{j-1}}{2}$.

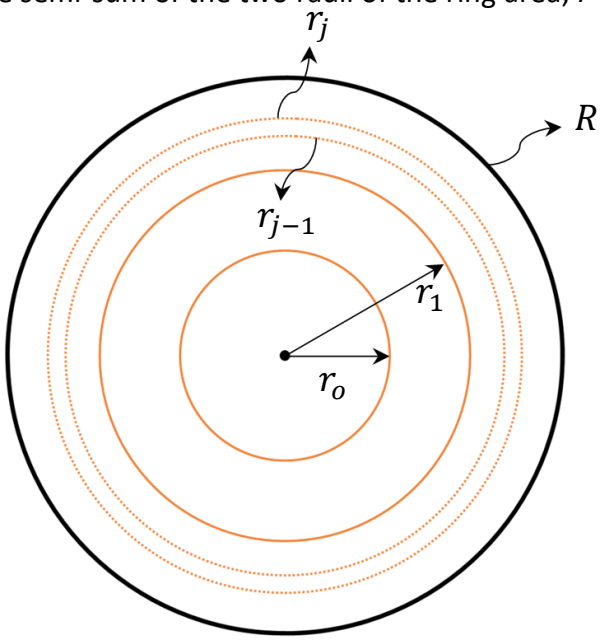

Figure 2.16 Numerical grid for velocity integration (constant areas).

In this method, the flow is considered to be axisymmetric (1D) and the resulting measurement distances are in the form of radial values r. By this consideration, the velocity profiles are the same in every axis that coincides with the center of the duct. Measurements are taken at the vertical axis, parallel to the injection axis. To produce a complete velocity profile the measurement points are doubled, for the upper and the lower halves of the duct respectively. The two sets of points are axisymmetric, and each pair of points represents the velocity value at the same radial distance. According to this, the velocity values for each pair of axisymmetric points must be about the same value. The diameter resulting radial distances are non-dimensionalised using the duct's radius (R); $r_{norm} = r/R$. The average profile velocity is obtained, as the mean value of the velocity measurements, and therefore the air supply can be acquired. By utilizing this numerical grid, the measurement points are denser near the duct wall and sparser near the center. This is beneficial for the visualization of the velocity profile, as the velocity experiences the highest changes near the duct wall,

due to the development of boundary layers. Beyond the boundary layers, the velocity values are expected to be about constant.

Results and Discussion

In Figure 2.17, the velocity profiles are illustrated for every inverter frequency case, as a function of the non-dimensional radius. A number of 11 measurements are taken inside the area of the duct, plus two additional at the wall duct; thus 13 measurements in total. It can be observed that the velocity profiles are about linear, apart from the boundary layer regions. Especially, as it is expected, the extend of the boundary layers is directly related to the velocity of the airflow, as higher velocities produce noticeably stronger boundary layers. The longer boundary layers are observed in the case of 50Hz, while at 20Hz the boundary layers remain the shortest. The graph curves are approximately symmetrical to the horizontal axis; thus, the velocity profile is axisymmetric as it is expected.

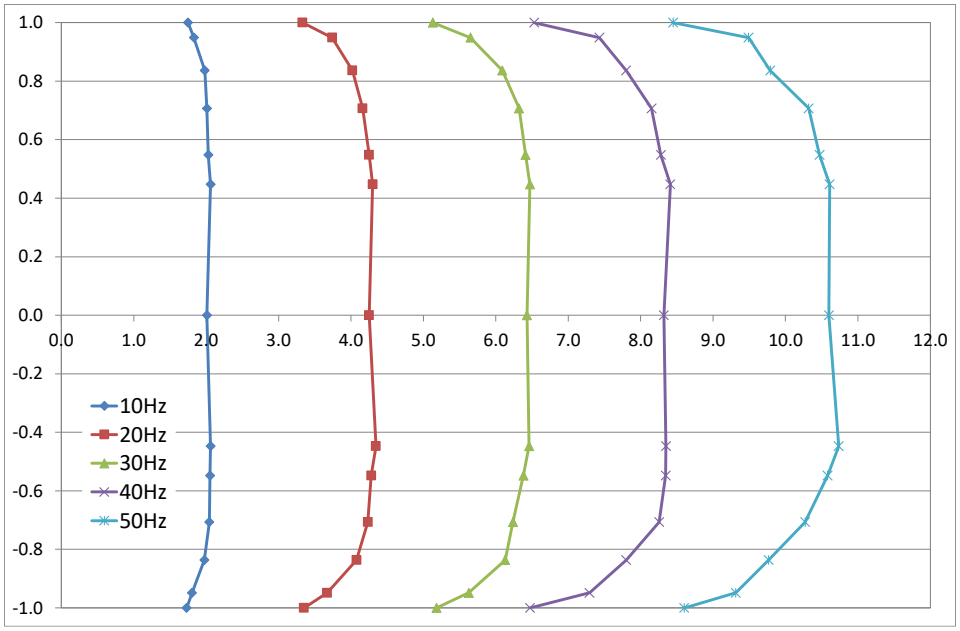

Figure 2.17 Crossflow velocity profiles for every inverter frequency.

The crossflow calibration results are shown in Table 2.7. The volumetric air supply is calculated as $Q_{air} = \bar{U}A = \pi\bar{U}D^2/4$, where D is the diameter of the duct. Another parameter that is addressed is the Weber number of the gas phase, which provides important information about the crossflow interaction between the gas and liquid flows. The primary liquid used is water and the environmental temperature is about 20 ^{o}C, the surface

tension is calculated at about $\sigma = 0.0728\ N/m$. According to that, the Weber number is given by $We_g = \rho_g \bar{U} d/\sigma$, where ρ_g is the density of the gas phase and d nozzle orifice (characteristic length).

Table 2.7 Crossflow air calibration results

Frequency (Hz)	Average Velocity (m/s)	Air Supply (m^3/s)	Weber Number	Daily Standard Deviation
10	2.0	0.021	0.03	1.39%
20	4.1	0.045	0.11	1.76%
30	6.1	0.066	0.25	0.99%
40	8.1	0.087	0.44	1.82%
50	10.0	0.108	0.68	0.50%

Obtaining the data for the air supply, the calibration type $Q_{air} = Q_{air}(I)$ can be derived, if I is the inverter's frequency. This relation can be observed at Figure 2.18. The volumetric supply is increasing for increasing frequency, with an approximately linear relation.

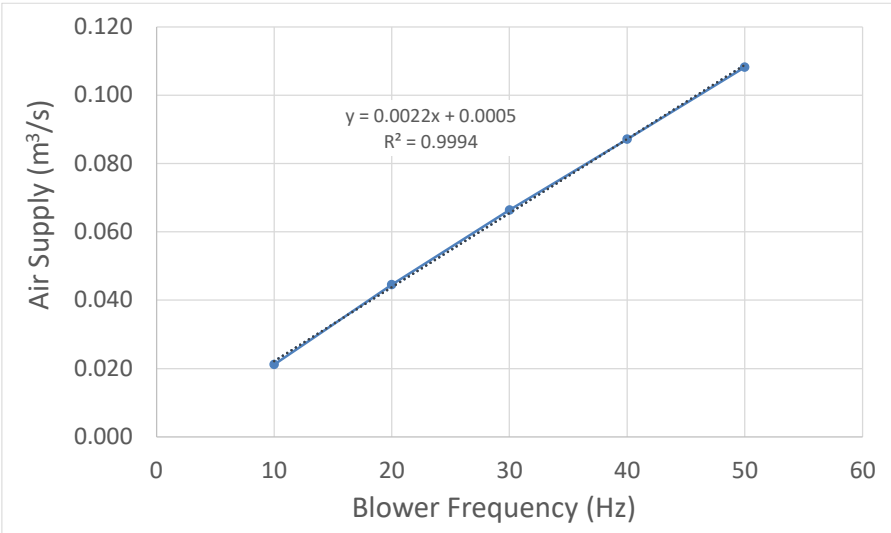

Figure 2.18 Volumetric supply of air as a function of blower's frequency.

Chapter 3 Results and Discussion

In this chapter, the results of the experiments are presented, discussed, and compared to the theory. Typically, the experiment is divided into two parts: liquid jet in crossflow (LJICF) and liquid spray in crossflow (LSICF). In theory, the two phenomena are connected since the former is a specific sub-case of the latter, with zero atomizing air. However, the data processing approach differs in each case. Additionally, the case of LJICF includes the investigation of the breakup location. This is absent in LSICF, since the location of the breakup is constant, imposed by the airflow of the atomizer. In addition, the LSICF includes the investigation of the boundary layers of the spray which is absent in LJICF.

The case of LJICF is investigated prior to the LSICF. As it has been discussed in the section 1.4, the behavior of sprays is by a great extend chaotic. In comparison to that, there is a greater level of determinism in the case of LJICF, and the phenomenon is partially supported by theoretical evidence; therefore, certain behavior characteristics are expected by LJICF. According to this, the LJICF results provide a good verification of the credibility of the experimental procedures, the calibration of the instruments, the processing, and the experimental arrangement in general. Essentially, obtaining insight about the LJICF acts as a basis for the LSICF.

3.1 Liquid Jet in Crossflow

3.1.1 Jet Data Processing: Binary Images Method

The data processing relies on the contrast variances of the images. Along with the 500 data images of each case, a total of 50 images of the background are taken. The background images are averaged in order to eliminate the noise, and the average background is obtained. The data images of every case are also averaged to acquire the average jet images.

These indicate the general behavior of the trajectory in each case, and the average breakup length. After that, from each one of the images in every case the average background is subtracted. The resulting images have the highest brightness values in the jet area, and the lowest in every other pixel. Utilizing two separate thresholds; one for the brightness and one for the pixel area, the binary images occur, and the jet is separated from the droplets. The binary images of the jet contain a value of 1 in the jet pixels and 0 everywhere else. This process can be observed in the example of Figure 3.1. According to that, the CBL (jet ending point) and the trajectory of the jet can be obtained for every image. After that the average CBL the standard deviation of every case can also be acquired.

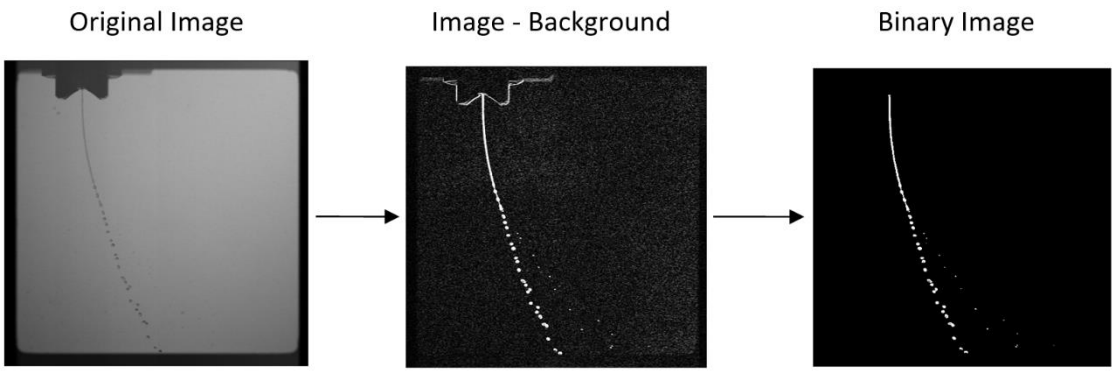

Figure 3.1 Data processing procedure.

3.1.2 Jet Trajectory

In Figure 3.2 and Figure 3.3 the average jet images are illustrated for crossflow cases of We=0,0.11,0.44, for liquid flowrates of Re=1200 and Re=2150 respectively.

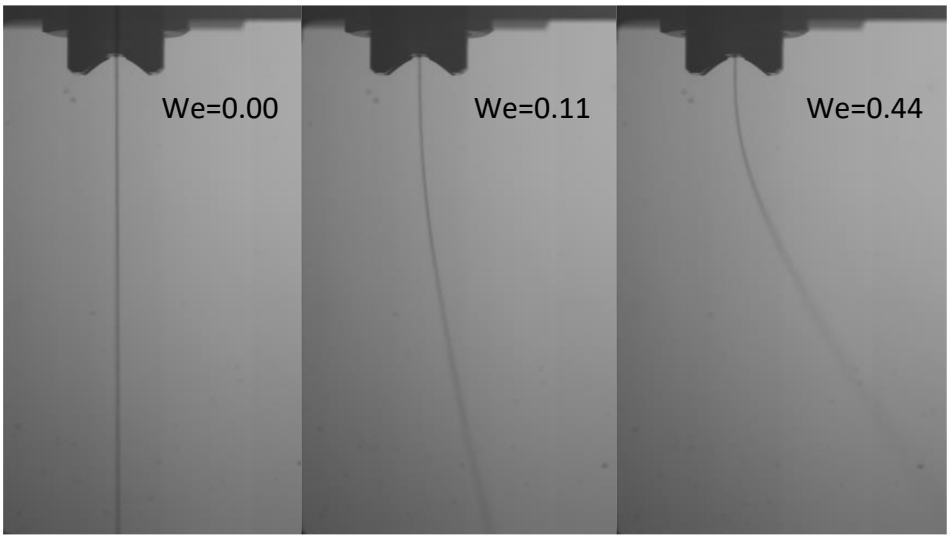

Figure 3.2 Average jet images Re=1200.

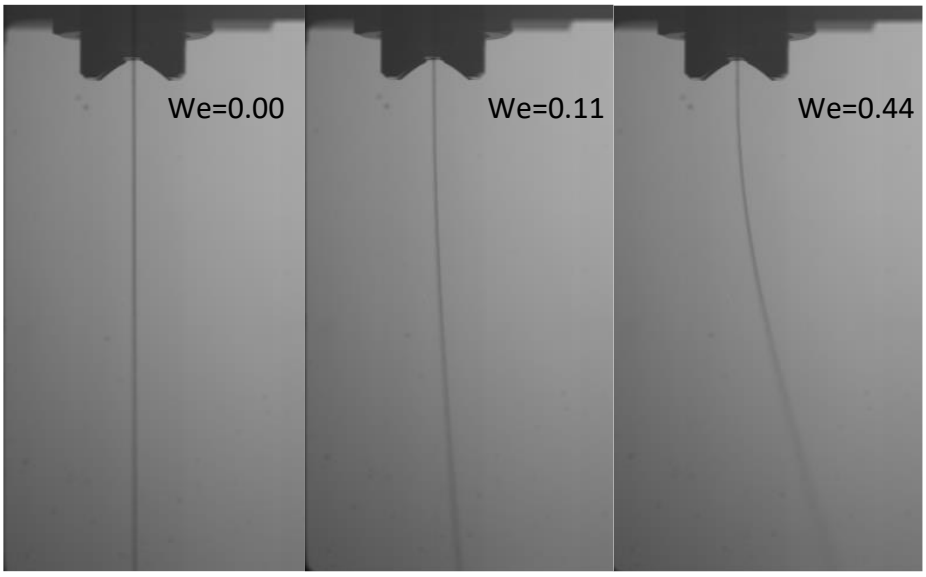

Figure 3.3 Average jet images Re=2150.

It is apparent that the jet deflection is increasing for higher Weber numbers, while a rise in the Reynolds number reduces the deflection. After a certain distance upon the jet, the density of the fluid seems to drop. That is due to the atomization of the jet, it is transform from a solid bulk to a sparse multitude of droplets.

In terms of processing, the points of the jet are interpolated utilizing a powerline fit in the form of $x = ay^b$. The power fit is employed in every image of the sample space. Accordingly, the average value of the fit constants, $\bar{a}$ and $\bar{b}$, are acquired which correspond to the average jet trajectory, along with the corresponding standard deviations.

The average trajectories of the jet for every crossflow case (We=0,0.03,0.11,0.25,0.44,0.68) are illustrated in Figure 3.4 for Re=1200 and in Figure 3.5 for Re=2700, which correspond to the lowest and highest liquid flowrate respectively. The solid lines represent the trajectories provided by the power-law fit, while the dotted ones, the measured data. It can be concluded that the power-fit coincides well with the original data, meaning the power-law equations are accurate. The only points observed to possess some deviation from the trajectories predicted by the power-fit, are those close to the breakup location, which is reasonable, due to the amplification of perturbations upon the jet.

The jet possesses higher deflection by increasing the momentum of the crossflow. As expected, in low liquid flows, the penetration of the jet is decreased for increasing airflow, as the atomization mechanics are enchanted, due to stronger aerodynamic interaction. This tends to alternate as the Reynolds number increases. A more comprehensive investigation of the penetration is conducted in section 3.1.3.

As expected, in zero crossflow conditions the trajectory coincides with the horizontal axis resulting in zero deflection. As the Weber number increases, along with the deflection, its rate of change increases, which is controlled by the b constant. In Re=1200, the trajectory follows a hyperbolic curve for high Weber numbers, while in the case of Re=2700 the trajectory approximates a more linear correlation.

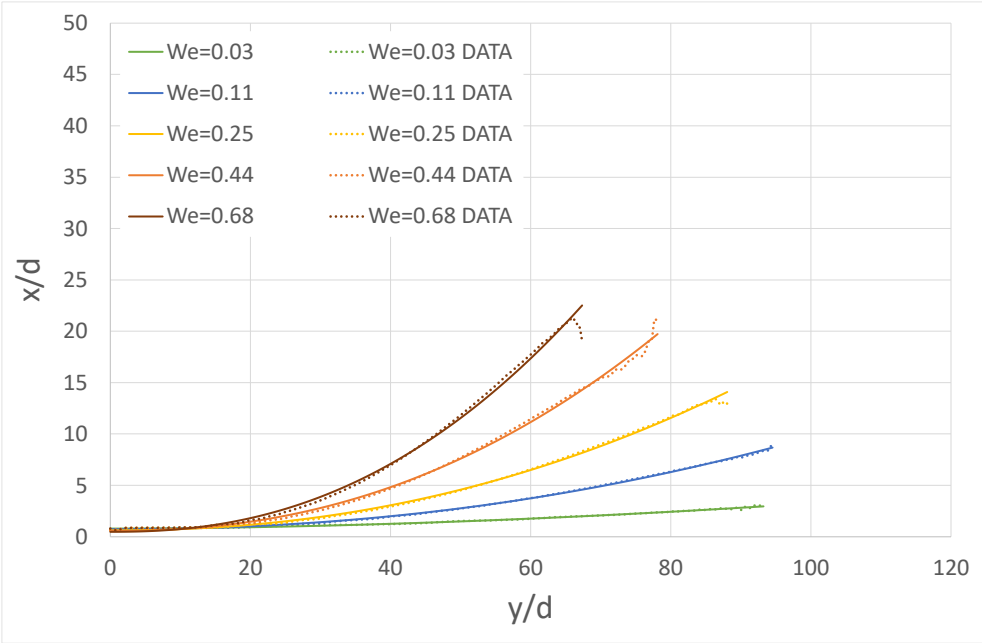

Figure 3.4 Average jet trajectories for every Weber number, for Re=1200.

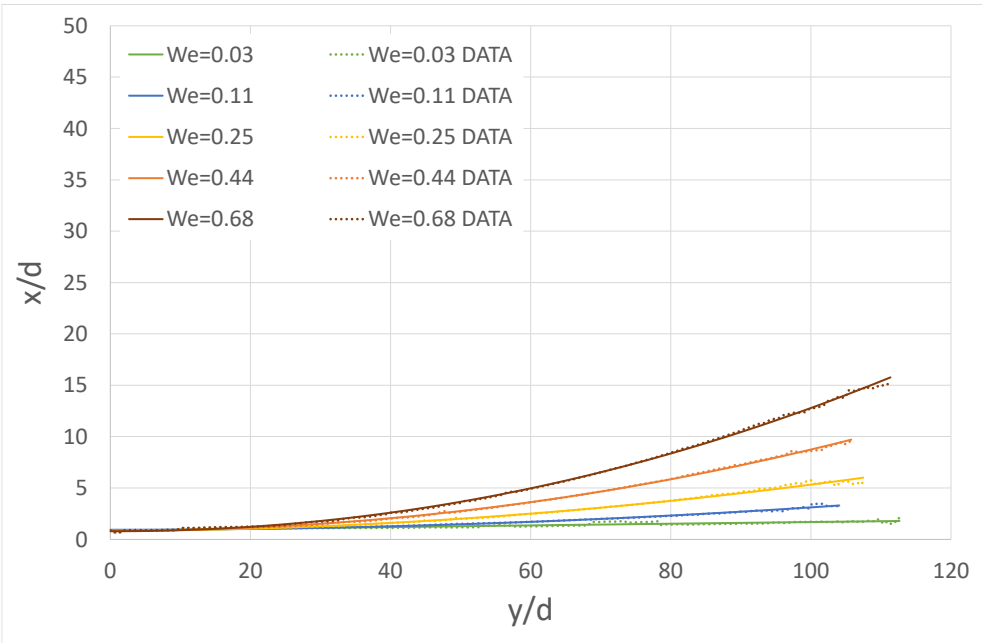

Figure 3.5 Average jet trajectories for every Weber number, for Re=2700.

According to the corresponding theory of LJICF reviewed in section 1.3.2, the jet is considered to follow a parabolic curve, thus the exponential factor is expected to be about 2. To investigate all the case-studies, the average b-constant in relation to the Weber number for every Reynolds number $\bar{b} = \bar{b}(We, Re)$, is illustrated in Figure 3.6. In quiescent air, there is no deflection of the jet thus the exponential factor is zero.

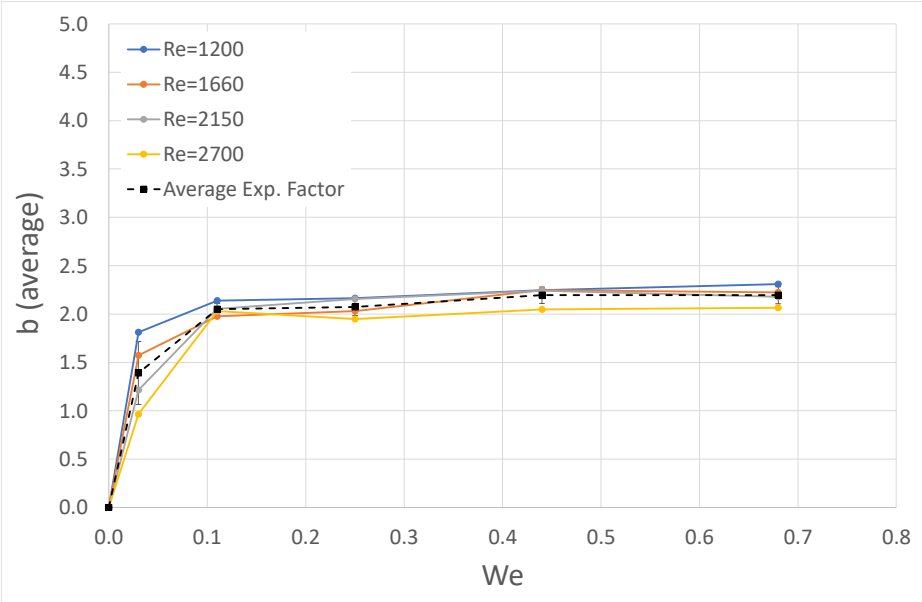

Figure 3.6 Mean b in relation to Weber and Reynolds numbers.

It is observed that in strong crossflow conditions the exponential factor revolves around the value of 2 as expected. As an exception to that, in the case of We=0.03, which is the lowest crossflow condition, the coefficient possesses the highest deviation from the average trendline. Specifically, while in the case of We=0.03 and Re=1200, the factor is about 1.81 (relatively close to the expected value of 2), nevertheless the value decreases as the Reynolds number increases, down to ~0.97 for Re=2700. This can be explained, by the high values of momentum flux ratios q in the case of We=0.03. As q increases approximately from 1700 to 8500, the deflection of the jet becomes negligible, and thus, a power-fit interpolation is not optimal. Essentially, the high relative momentum of the jet prevents it from changing its trajectory. In this situation the problem approaches the case of zero crossflow, thus why the exponential factor tends to decrease down to 0.

Followed the case of We=0.11, an insignificant change in the exponential factor is observed, thus it remains approximately the constant. The highest value obtained is about 2.3 in the case of the lowest momentum flux of 70.

3.1.3 Column Breakup Location

One of the most important characteristics due to investigation is the column breakup location (CBL). During the growth of perturbations upon the jet, the point of the jet

disintegration is a time-depended variable while also the CBL is governed by the liquid and gas flow parameters. Consequently, the study of the CBL consists of two main parts: average and transient CBL investigation. In the former, the average breakup location is calculated for every study case, and by this, correlations can be obtained between the CBL and the system parameters, such as liquid or gas flowrate and the atomizer angle. Another significant implementation is the verification of the repeatability of the experiment, through the daily average CBL deviation. In the latter, the change of the CBL values during the measurements is investigated, through statistical correlations. Each one of the images collected are processed individually, thus in this method the running CBL deviation can be obtained which indicates the level of precision of the corresponding average CBL value in each case. Generally, the breakup location can be expressed as $CBL = CBL(Re_l, We_g, \theta)$.

Transient CBL Inspection

To examine the fluctuations of the CBL during the measurements, it is considered that CBL follows a random distribution with a mean value and a standard deviation, governed by the liquid flow and the crossflow conditions. The CBL of every single one of the 500 images is calculated and therefore the histograms of the x and y components of the CBL can be obtained. The CBL is non-dimansionalized by the nozzle diameter d which has a value of 0.41mm. Some of the histograms can be observed in Figure 3.7 for the penetration (CBL-y) and in Figure 3.8 for the deflection (CBL-x).

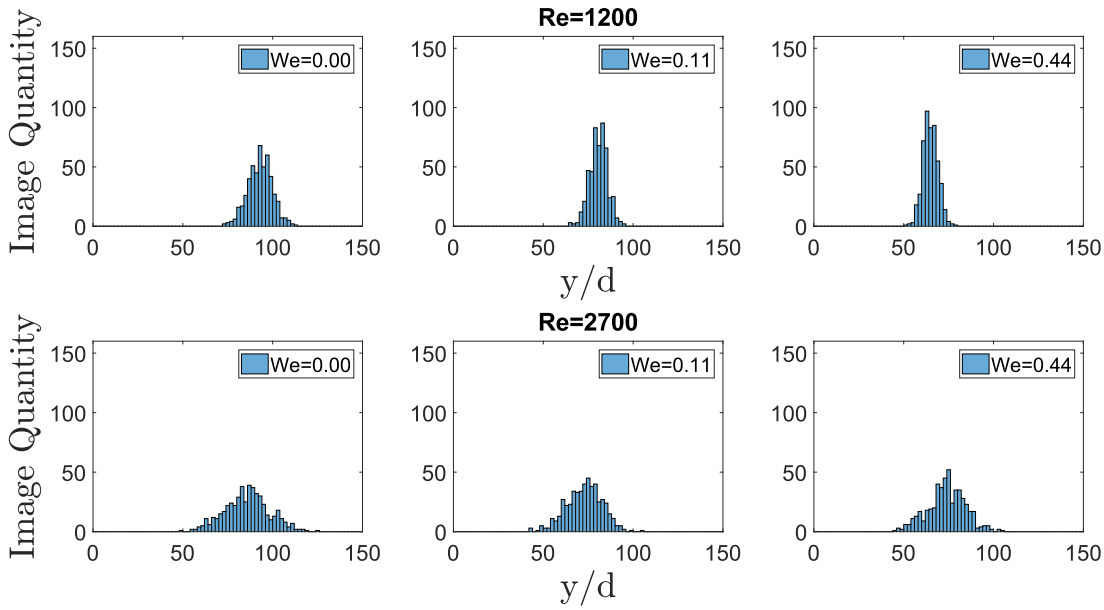

Figure 3.7 Penetration distribution in comparison to We and Re

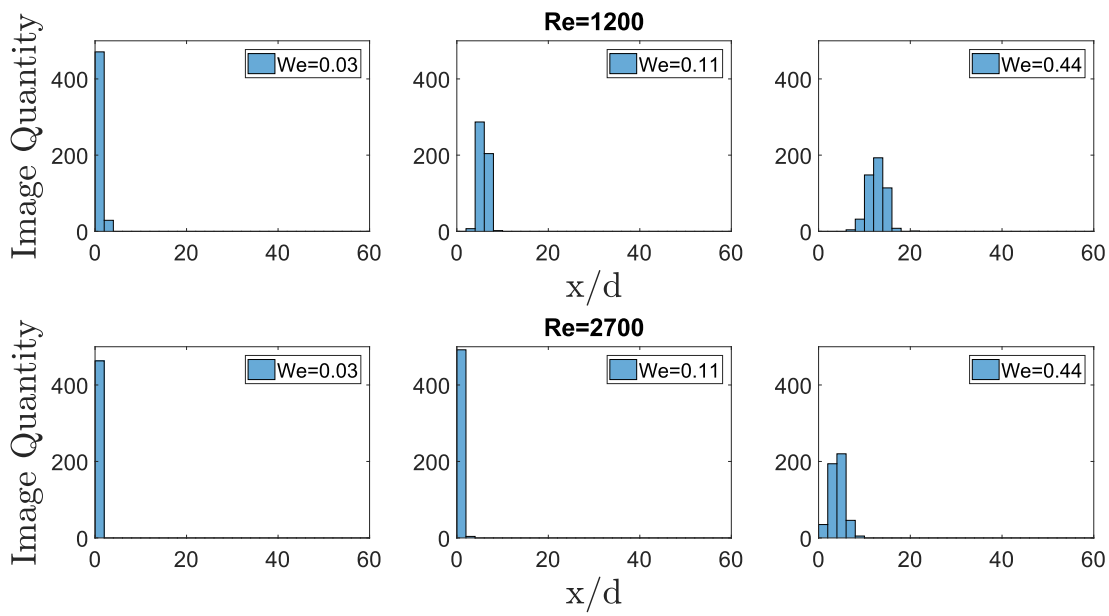

Figure 3.8 Deflection distribution in comparison to We and Re.

.

Observing the CBL histograms, the following conclusions can be stated:

1. In low liquid flowrates, the average penetration tends to decrease for increasing airflow, as the distribution shifts to lower y/d values. That is due to the increase of

the deflection of the jet, as well as the reinforcement of atomization phenomena by the strong airflow. In addition, the standard deviation seems to possess a negligible decrease, for increasing airflow.

2. In high liquid flowrates, the average penetration is decreasing with lower rate for increasing airflow, due to the high momentum of the liquid phase. The standard deviation remains about constant.
3. The average deflection of the jet increases for increasing airflow. However, the rate of increase decreases, for increasing liquid flowrates. The change of standard deviation seems insignificant to the Weber number.
4. The standard deviation of the penetration increases, while the standard deviation of the deflection seems to remain about constant for higher Reynolds.

The following figures are formed to provide a better visualization and quantification of the preceding relations, for all study-cases.

Figure 3.9 correlates the penetration y/d and the deflection x/d of the jet of every liquid flowrate case, with the Weber number of the airflow. As the momentum of the liquid phase increases, the aerodynamic effect the airflow has to the atomization decreases. The deflection of the jet increases as expected for higher Weber numbers, and the effect of the aerodynamic interaction in the deflection of the jet, is less significant for higher liquid flowrates. The most noticeable effect of the aerodynamic interaction upon the jet can be observed at Reynolds 1200 which is the case with the lowest liquid momentum

Figure 3.10 illustrates the standard deviation of the penetration and the deflection. The St.D. of the penetration does not seem to have a noticeable change for increasing Weber number but increases for higher Reynolds numbers. The St.D. of the deflection remains about constant for both increasing Weber and Reynolds values, except of the case of Reynolds 1200, in which the deviation seems to decrease for higher Weber values.

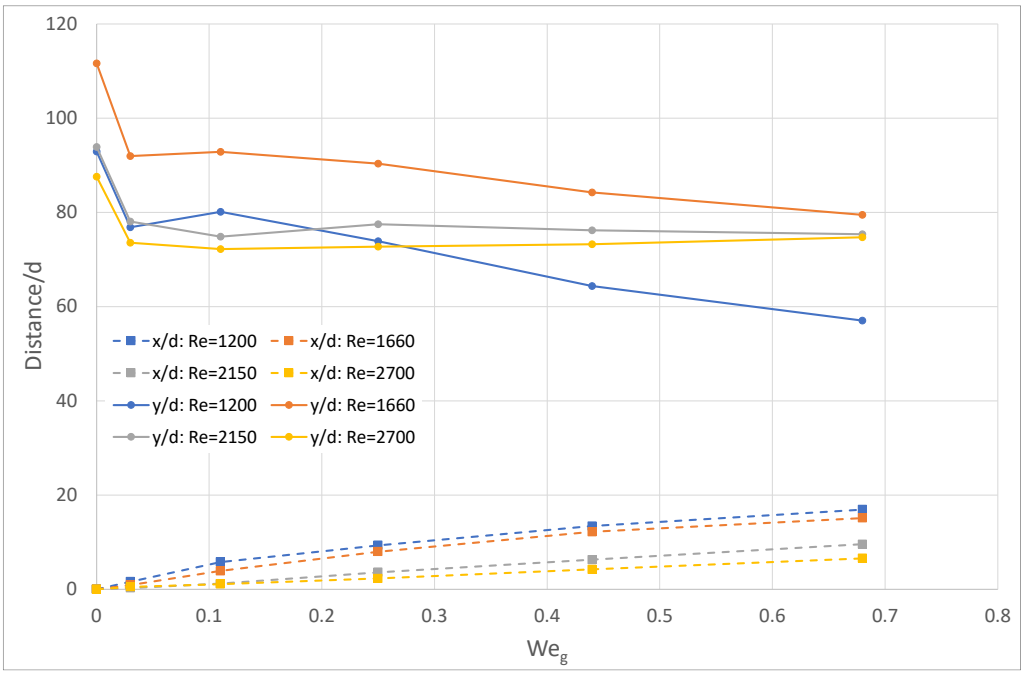

Figure 3.9 Average penetration and deflection in relation to the Weber number of the airflow, for every liquid flowrate.

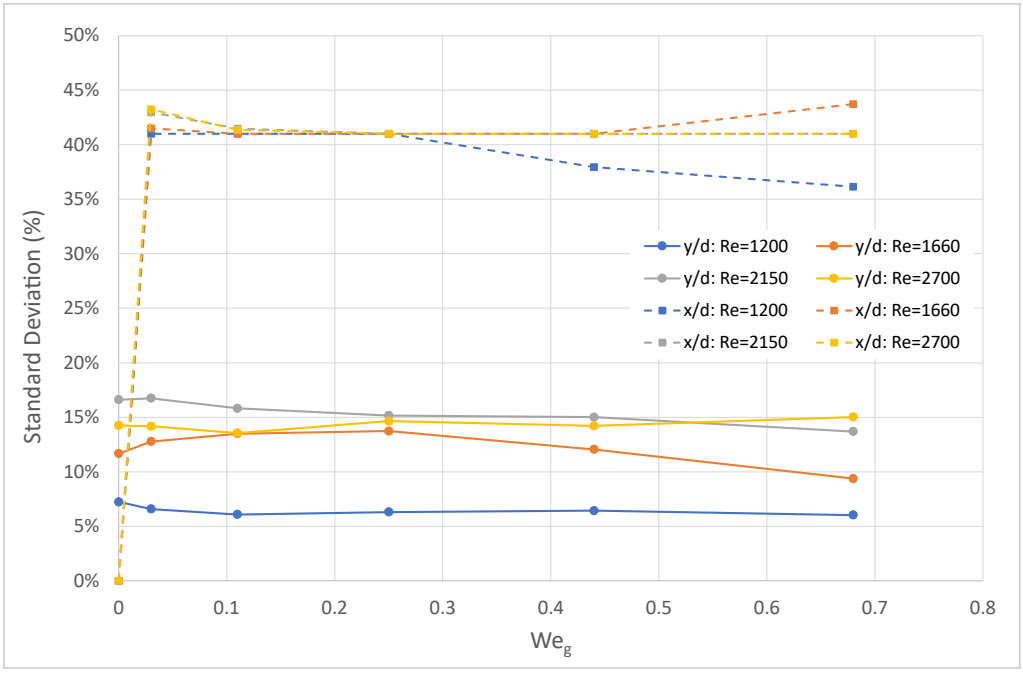

Figure 3.10 Standard Deviation of the penetration and deflection in relation to the Weber number of the airflow, for every liquid flowrate.

Average CBL Inspection: Atomizer Orientation and Repeatability

The impact of the atomizer's orientation upon the atomization is investigated. Additionally, the CBL distributions, should be about identical for different measurement dates.

Accordingly, the distribution must possess about constant average CBL values. The standard deviation should also be approximately the same, however, since the flowmeter is controlled manually, the running deviation could vary depending by the level adjustments needed for the flowmeter, and not entirely by the physical properties of the system.

First and foremost, the effect of the angle of the atomizer θ is inspected. The jet column is of cylindrical shape, which is axisymmetric. Accordingly, the orientation of the atomizer is expected to have no considerable effect in the average CBL. To investigate this, the jet is tested in zero crossflow conditions for every liquid flow case. When the crossflow is absent, the is zero deflection of the jet and therefore the CBL coincides with the penetration of the jet, since is possesses only a y-axis value (CBL-y). In Figure 3.11, the progression of the average penetration is illustrated as the liquid flow increases; $Re = 1200,1660,2150,2700$ and for both atomizer orientations; $\theta = 0^o, 90^o$. The CBL values are non-dimensionalised by the diameter of the atomizer's orifice $d = 0.41\mathrm{mm}$. As expected, the trendlines are approximately the same, providing an average error of 1% and a maximum error of 1.53% in the case of 1200 Reynolds number, which is reasonable, since this case corresponds to the lowest flowrate being the most external case of the flowmeter's operation range, as discussed in section 2.3.1. A miniscule insignificant Reynolds deviation can be also observed which reaches the maximum error of 0.38%. The error bars represent the running standard deviation of the CBL provided by the transient analysis.

According to the results, it can be concluded that the orientation of the atomizer does not affect the CBL in any considerable manner, since even the negligible errors occurring, are most likely produced by the operation of the flowmeter or by random factors.

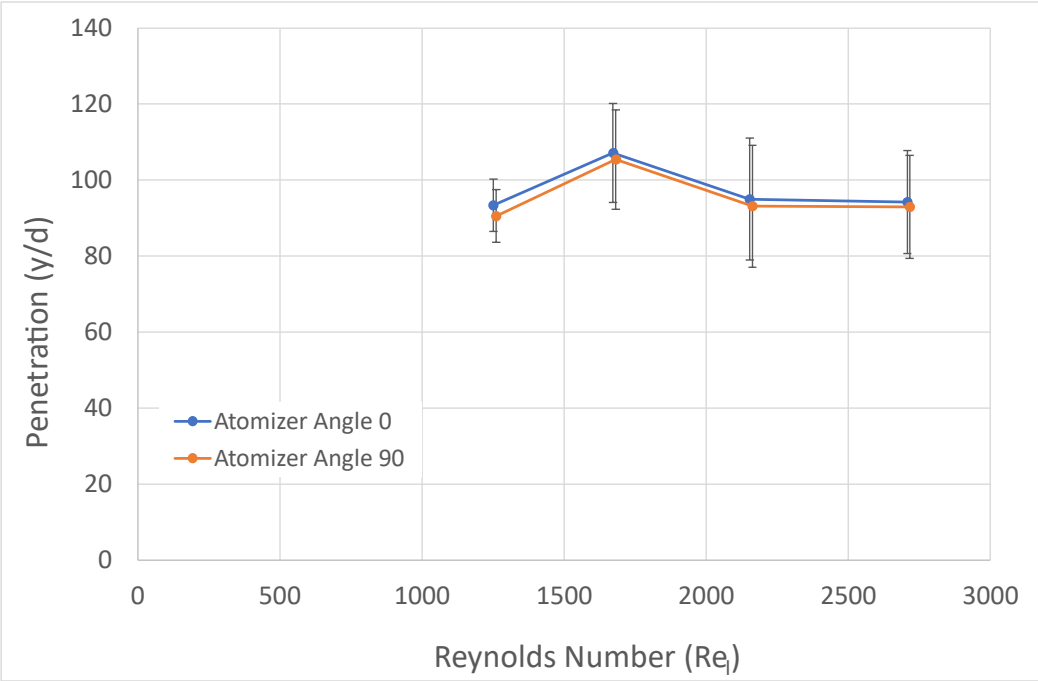

Figure 3.11 Jet penetration in quasi-stationary atmosphere for every Reynolds case and atomizer orientation.

Furthermore, it is crucial to obtain results about the repeatability of the experiment. To verify this, the progression of the average penetration of different measurement dates and for both orientations of the atomizer is compared for every crossflow condition, governed by the liquid flowrate. Typically, the graphs of zero crossflow and highest crossflow are observed in Figure 3.12 and Figure 3.13 respectively.

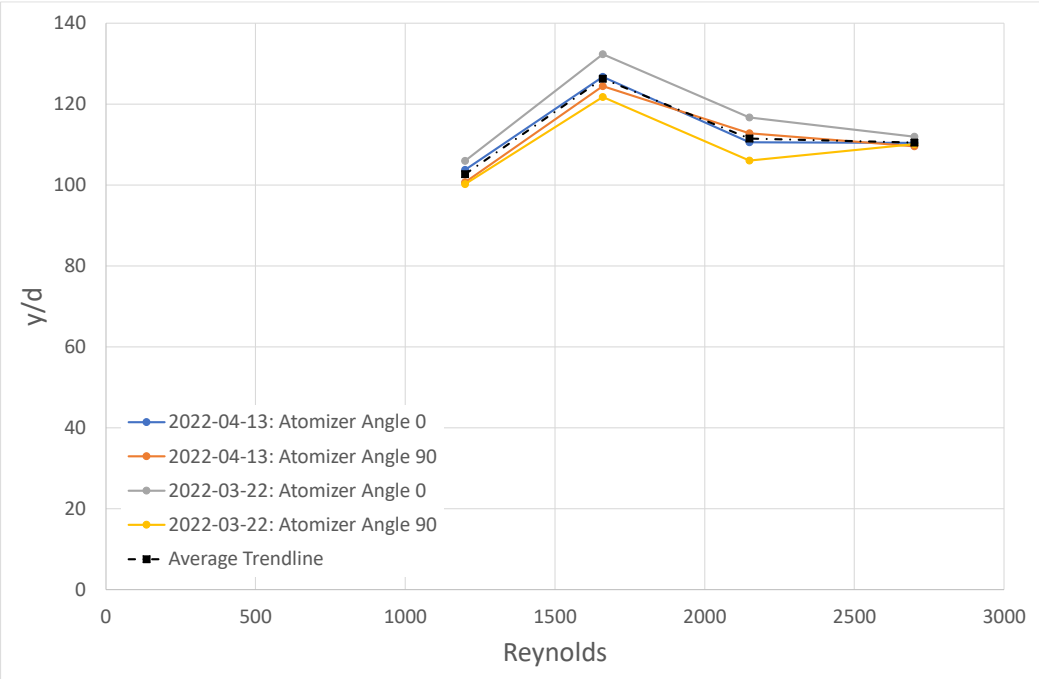

Figure 3.12 Jet Penetration Comparison for $We_g = 0$.

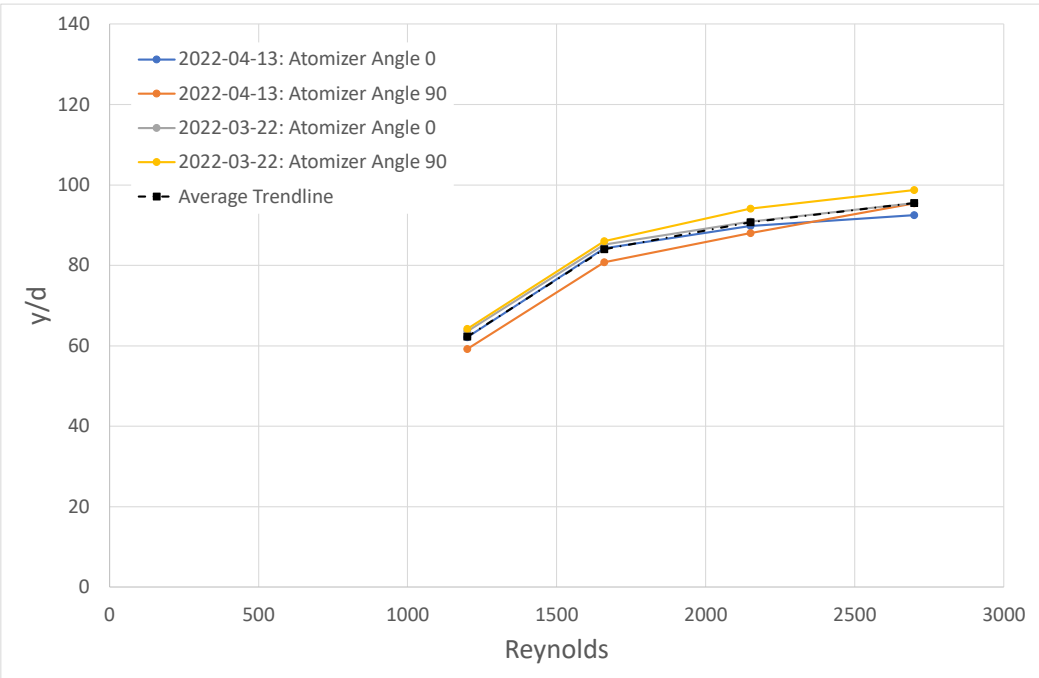

Figure 3.13 Jet Penetration Comparison for $We_g = 0.68$.

It can be observed that the trendlines remain about the same. The penetration values seem to be in agreement amongst themselves, and the divergence of the trendlines declines as the Weber number increases. The penetration values are average for every date and

orientation, and the average trendline can be estimated. The trendline error (equivalent to a daily standard deviation) is defined as the divergence from the average trendline. The average penetration trendlines for every crossflow condition are illustrated in Figure 3.14. It is worth noting that in the cases of non-zero crossflow (We>0), for high Reynolds values the penetration tends to converge to a similar trendline.

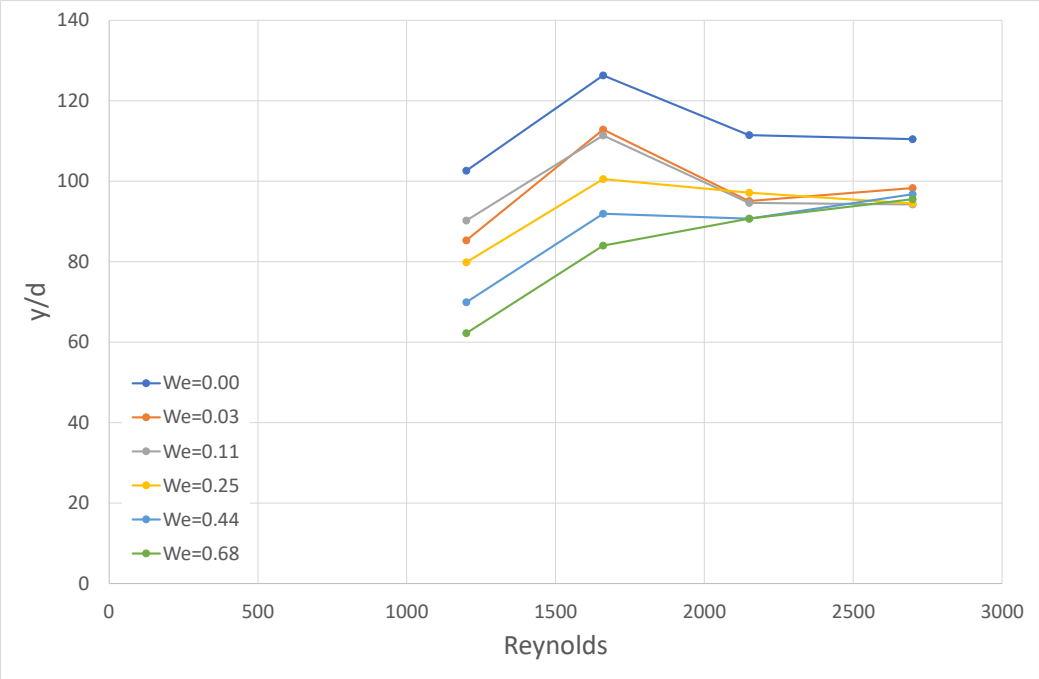

Figure 3.14 Penetration average trendlines for every crossflow case.

The maximum error produced by the trendlines is about 5% which is acceptable. It is also worth mentioning that the liquid flowrate case of Re=2700 which is considered to be in the transitional flow region (and not entirely laminar), produces accurate results with a maximum error of 5%. A valid inspection is the averaging of the error of every trendline, resulting in the average error in dependence of the Reynolds number, for every Weber number. However, inspecting the error of the average penetration as a function of Reynolds in this case does not possess any physical meaning since, the flowmeter is controlled manually. According to this, error trendline does not represent the deviation due to randomness, but mainly the effectiveness of the manual adjustment of the controller. The average error progression trendlines are illustrated in Figure 3.15. The maximum average error observed is about 3.5% which is acceptable. Generally, the mean error decreases for

increasing Reynolds values. This verifies that the main source for the error of the results is the flowmeter's operation, since for higher flowrates the error of the controller decreases.

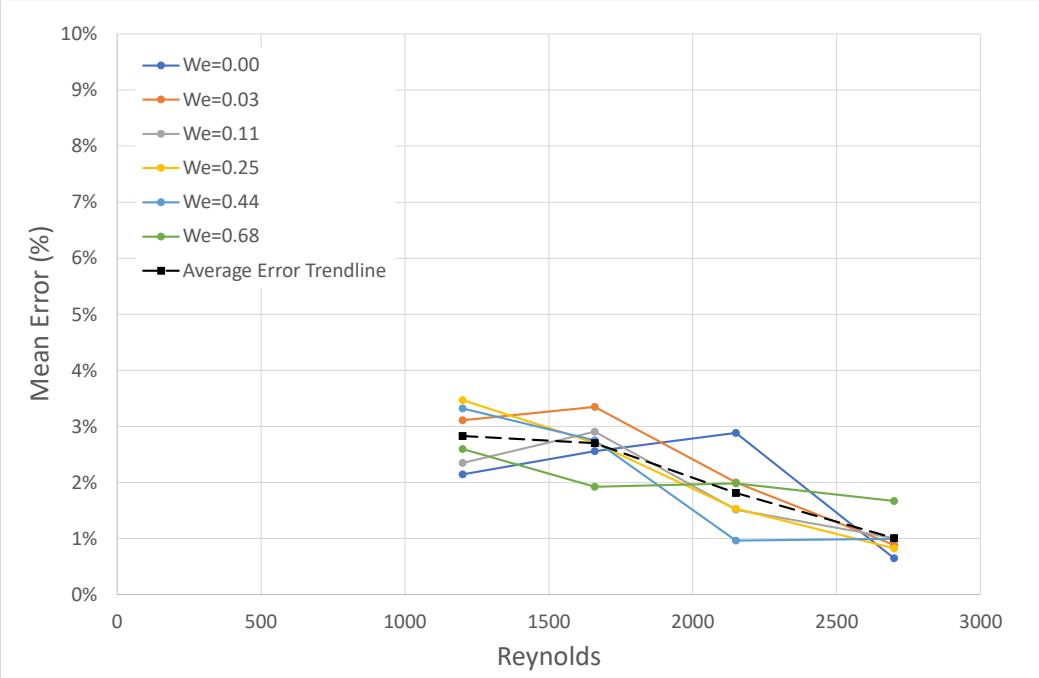

Figure 3.15 Mean error trendlines in comparison to Reynolds, for every Weber number.

According to the results, it can be concluded that the experiment is repeatable with maximum possible error of 5%. The error is expected to revolve 3% in the case of the lowest liquid flowrate (Re=1200) and to be degraded at about 1% in the highest flowrate case (Re=2700).

3.2 Liquid Spray in Crossflow

3.2.1 Spray Data Processing: Liquid Mass Contours

The method utilized to process the spray differs in comparison to the jet case. While both of the techniques rely upon the contrast fluctuations of the image, the spray structure possesses variating liquid density, and therefore it is captured with variating contrast from the sensor. The binary method that functioned exceptionally in the case of the jet (due to its constant density), is not viable in this situation. The distribution of the liquid mass is better

visualized by the means of contours of the contrast values. Specifically, the standard deviation of the contrast on every pixel is approximated utilizing the total sample of 500 images. It is expected that, for areas with higher spray density, higher contrast deviation values are acquired. The background areas, where no liquid mass is located, produce a small deviation equal to the background noise, which is negligible. An example of this procedure is illustrated in Figure 3.16. After the acquisition of the contour graphs, the average trajectory of the spray can be estimated, utilizing the gradual horizontal displacement from contour to contour, due to the crossflow. Additionally, the outer contour of the spray is isolated and employed for the investigation of the spray boundary layers.

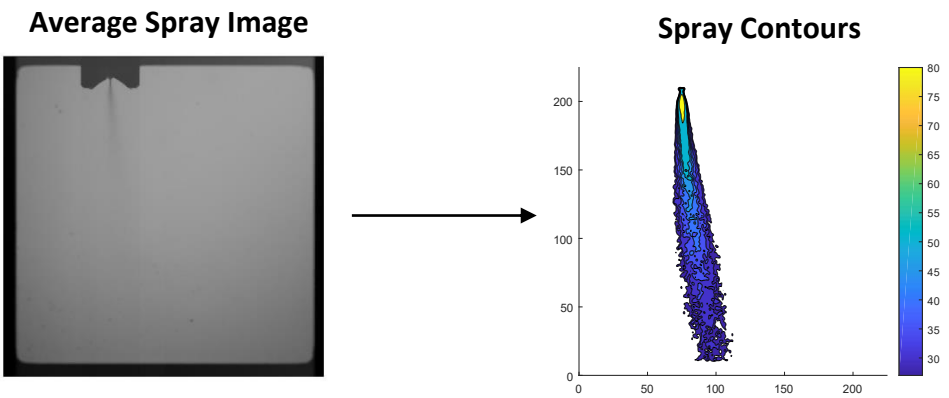

Figure 3.16 Spray Processing.

3.2.2 Spray Trajectory-Centerline

Visualization of the Spray

Figure 3.17 illustrates the spray (density contours) in quiescent atmosphere for increasing atomizing air (0,8,11 l/min) in atomizer orientation at 0°. As the GLR of the atomizer increases, the dispersion increases and thus the spray becomes sparser. The same phenomenon is illustrated in Figure 3.18 for 90° atomizer orientation. It can be observed that the spray structure differs in relation to the orientation of the atomizer, in contrast to the jet cases, due to the elliptical shape of the spray (non-axisymmetric).

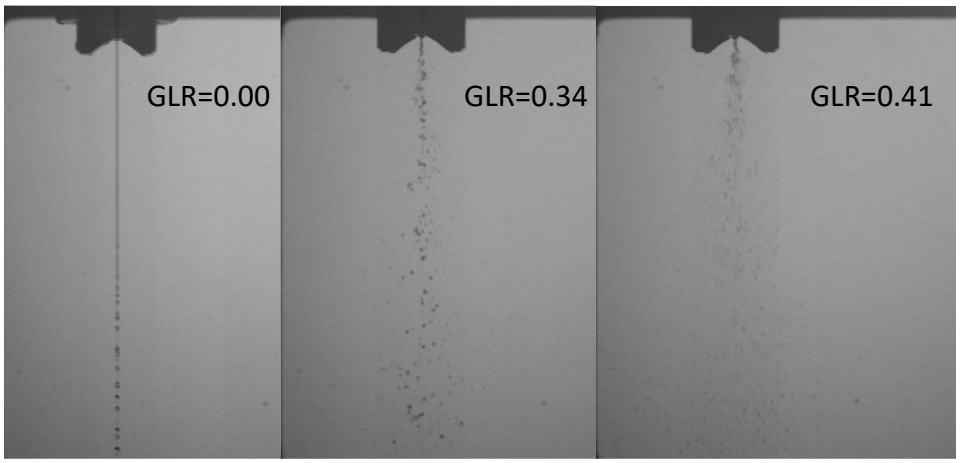

Figure 3.17 Spray structures Re=1660, θ=0°.

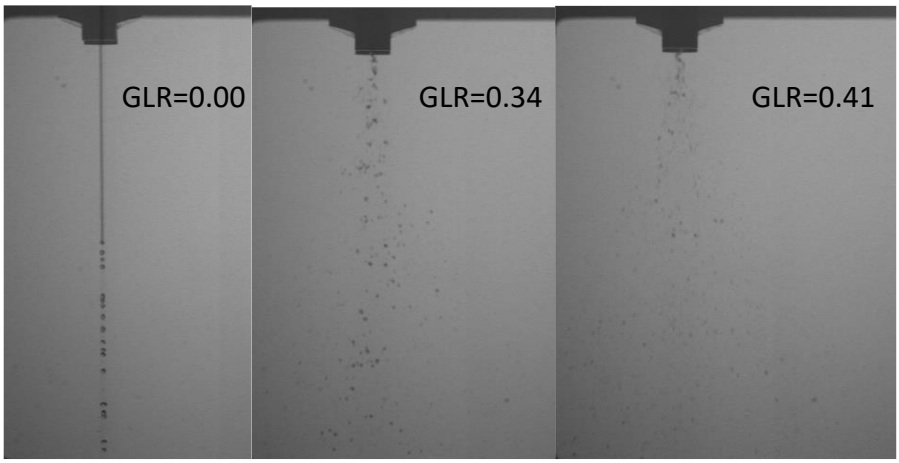

Figure 3.18 Spray structures Re=1660, θ=90°.

The difference between the two atomizer orientation cases, can be better observed in Figure 3.19, where the spray contours are illustrated in both atomizer orientations. The abundance of liquid mass located in the case of 0° degrees since higher density values are detected by the camera, given a penetration distance. On the contrary, the spray angle is higher at 90° orientation, thus the boundaries of the spray spread wider. Since the camera view is vertically placed to the crossflow direction, the aerodynamic area of 0° is higher than 90°. According to that, the deflection of the spray in the orientation of 0° is expected to be higher than 90°.

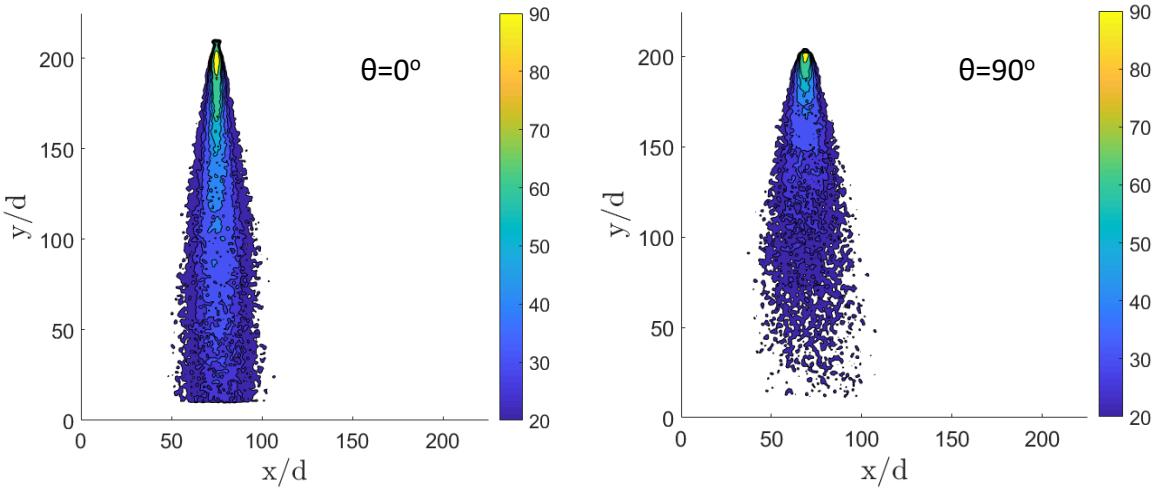

Figure 3.19 Spray contour figures; Re=1660, GLR=0.34.

Atomizer Orientation Effect on Trajectories

Figure 3.20 and Figure 3.21 illustrate the centerline trajectories of the spray, in the same Reynolds, Weber and GLR cases, for orientations of 0° and 90° respectively. It is observed that the spray deflects more in the case of 0° orientation.

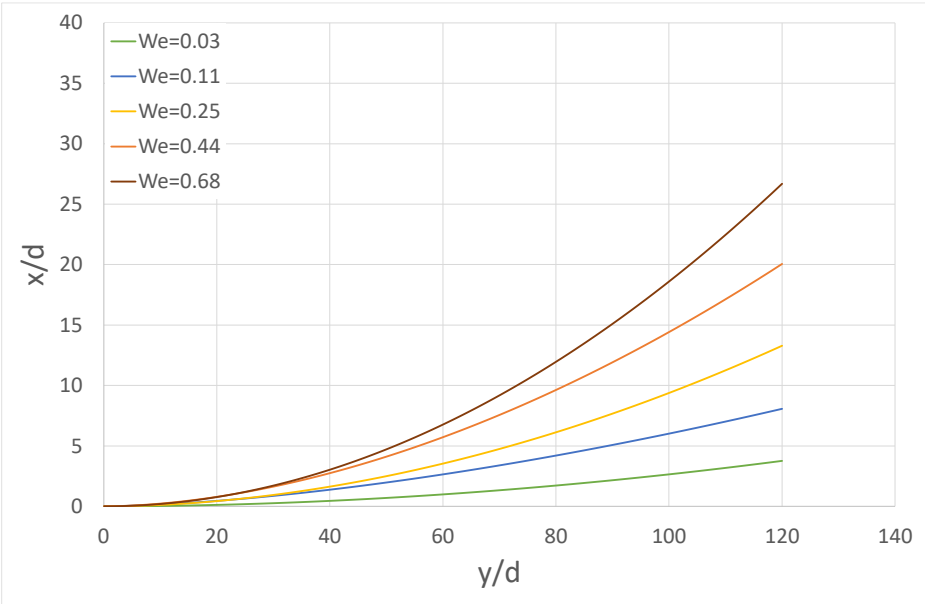

Figure 3.20 Spray centerline trajectories; Orientation 0°, Re=1660, GLR=0.34.

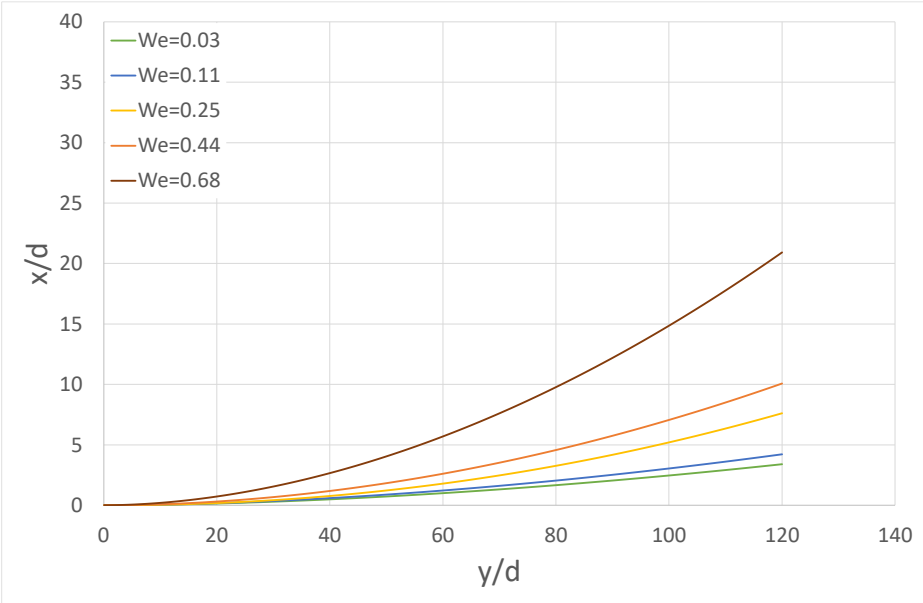

Figure 3.21 Spray centerline trajectories; Orientation 90°, Re=1660, GLR=0.34.

To quantify the difference the two atomizer orientation cases, in Figure 3.22 the increase of the maximum spray deflection, $(x/d)_{max} = \frac{x}{d}\left(\frac{y}{d} \cong 120\right)$, is illustrated, in relation to Weber and the orientation of the atomizer. As expected, the spray, in response to the crossflow, deflects more in the case of atomizer orientation 0°. Aside from that, a key difference can be noticed in the trendlines of the two cases. While the case of 0° seems to submit in a standard power-law trendline of increasing values, in the case of 90° the deflection values do increase, though in an unnatural manner. Consequently, the behavior of the spray in crossflow in the case of 90° seems to be more chaotic, in contrast to 0° orientation.

A potential explanation for this result, could be the amplification of droplet collision phenomena (scatter/coalescence) in the case of 90°, which can enforce a significant effect on the spray formation, even for a low-speed spray (M. Ruger et al., 2000). Since the spray is of elliptical shape, the distribution of liquid asymmetrical to the vertical axis of the orifice. A plentitude of droplets exists alongside the axis of the big diameter of the ellipsis, while in the small diameter the droplets are more evenly distributed. Subsequently, when the crossflow is parallel to the big radius of the spray, droplet collision effects are intensified due to the higher number of droplets in the direction of the crossflow, and thus the higher probability of impact.

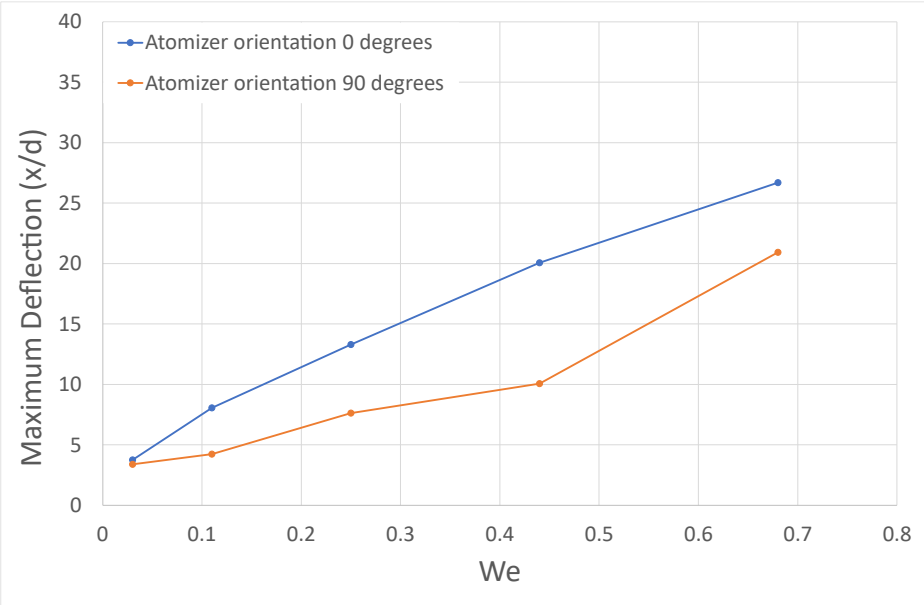

Figure 3.22 Maximum deflection in relation to Weber and atomizer orientation; Re=1660, GLR=0.34.

Power-law fitting for the Trajectory

In order to fully investigate all the case-studies, the exponential factor of the power-fit law $\frac{x}{d} = a\left(\frac{y}{d}\right)^b$, in relation to the Reynolds, Weber and atomizing air is investigated. Figure 3.23, Figure 3.24 and Figure 3.25 illustrate the average exponent for all the study-cases, for atomizing air of 8, 9 and 11 L/min respectively, in the case of atomizer orientation of 0°.

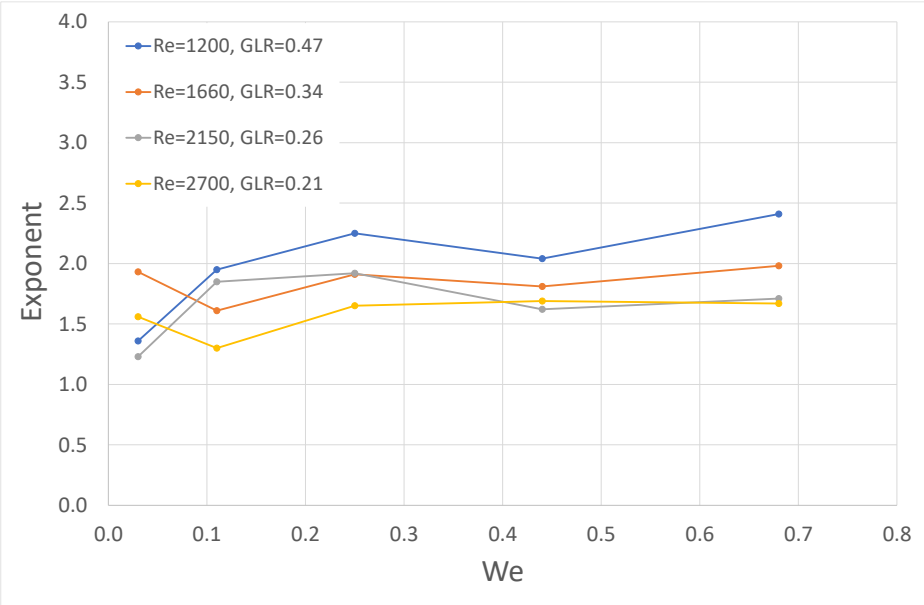

Figure 3.23 Exponent in relation to Weber and Reynolds; 8 L/min atomizing air, 0° orientation.

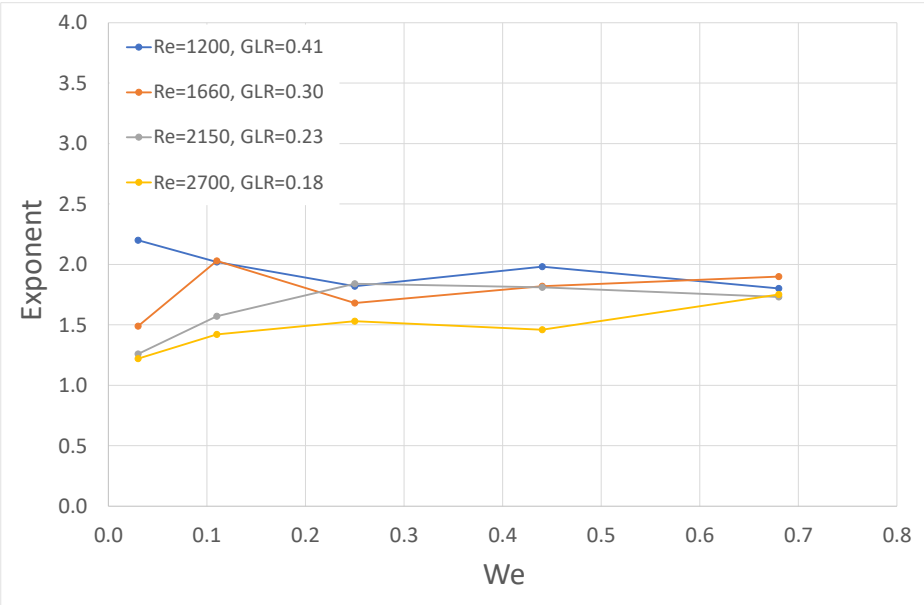

Figure 3.24 Exponent in relation to Weber and Reynolds; 9 L/min atomizing air, 0° orientation.

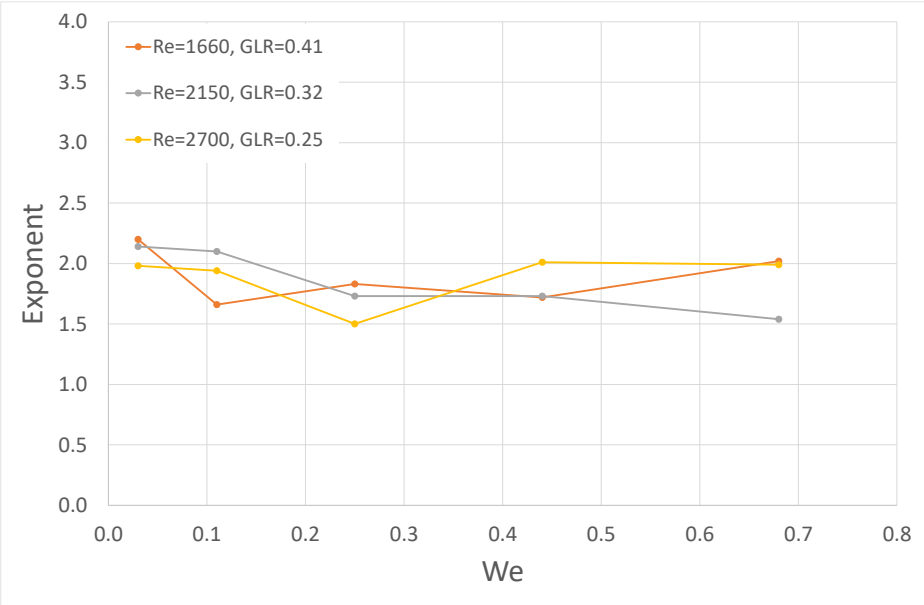

Figure 3.25 Exponent in relation to Weber and Reynolds; 1 L/min atomizing air, 0° orientation.

According to the theoretical analysis reviewed in section 1.3.2, the exponent is expected to revolve around the value of 2 (Ashgriz, 2011), as indicated by equation (1.19). The exponent values based on empirical correlations, are expected to result about 1.96-3.33 (No, 2015). The resulting values are between about 1.25-2.41, which are a bit shifted downwards (1.81 average exponent). The most diverging cases are the ones with really low exponent and their power-law fit must be inspected.

To verify the credibility of the power-law, two separate interpolations are made: the one providing the results, and one with a constant exponent of 2 for control. The two interpolations are graphed upon the contours of the spray, to inspect the trajectory and the credibility of the free-exponent interpolation. For instance, the case of Re=2150, We=0.03, GLR=0.23, which produces the lowest exponent of ~1.25, is illustrated in Figure 3.26. It is observed that the interpolation follows the trajectory well enough, and the free and constant exponent interpolations are in agreement. Therefore, even the lowest resulted values for the exponential factor, are representing the trajectory accurately.

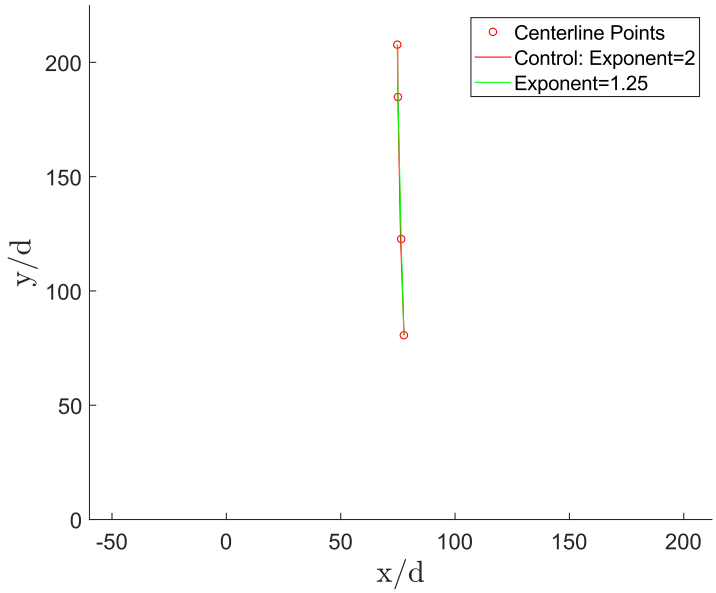

Figure 3.26 Power-law fit credibility; Exponent=1.25.

The corresponding graphs for the case of atomizer orientation of 90° are illustrated in Figure 3.27, Figure 3.28 and Figure 3.29.

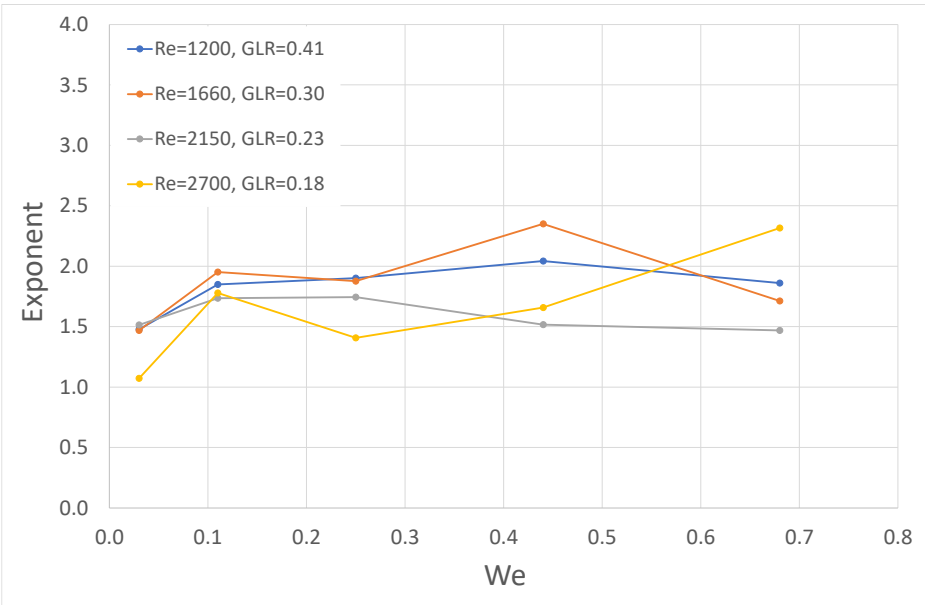

Figure 3.27 Exponent in relation to Weber and Reynolds; 8 L/min atomizing air, 90° orientation.

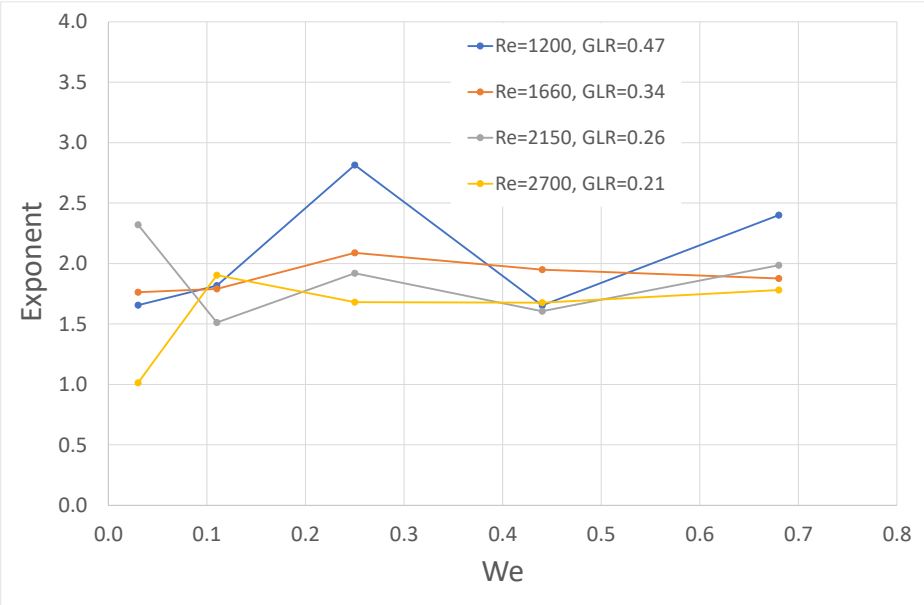

Figure 3.28 Exponent in relation to Weber and Reynolds; 9 L/min atomizing air, 90° orientation.

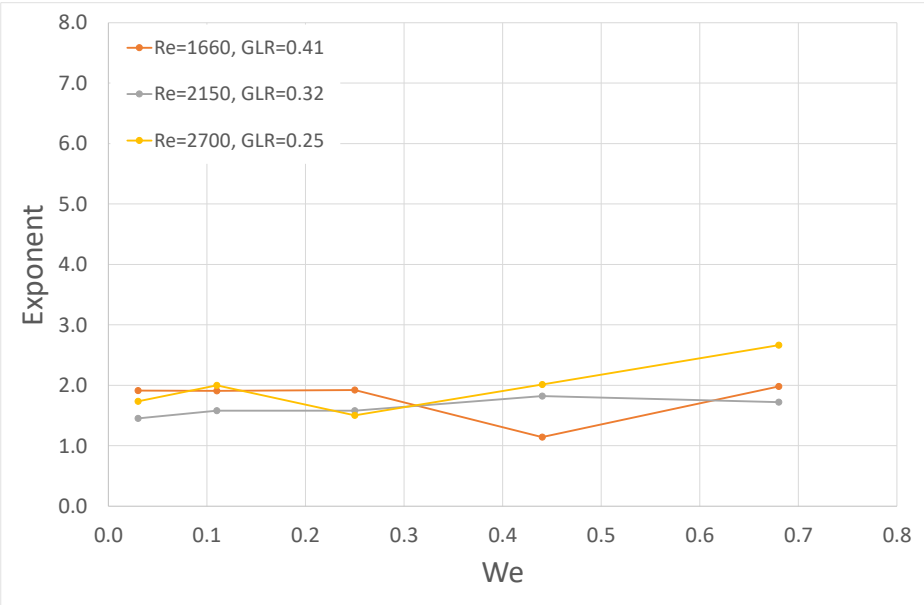

Figure 3.29 Exponent in relation to Weber and Reynolds; 11 L/min atomizing air, 90° orientation

Approximately a matching exponential factor behavior can be observed between 0° and 90° orientation. The exponent values result between about 1.1-2.8, signifying a larger deviation from the case of 0°. This conclusion that can be stated by comparing the corresponding graphs of the two orientation cases. The interpolation in the case of 90° seems to provide a more unstable behavior. This can be justified by the more chaotic nature of the spray in crossflow in the case of 90° due to droplet collision phenomena, as explained earlier.

Effects of GLR in Spray Deflection

Throughout the investigation of LJICF, the amount of trajectory deflection was expected to act in accordance with a simple norm: the stronger the crossflow, the bigger the amount of deflection, for a standard amount of liquid flow. This points to the fact that the trajectory of the jet is primarily governed by the relative momentum of the liquid and air flows, represented by the momentum flux q.

Nonetheless, the case of LSICF differs from that. In the part of Atomization Effects on Trajectories, the spray deflection was observed to increase similarly to the case of LJICF, however that is for a standard value of atomizing air flow (Figure 3.20, Figure 3.21). In contrast to the case of the jet, the trajectory in LSICF is governed by the interplay of the momentum of the liquid and the crossflow, in addition to the atomizer's airflow. The representative variable for the last one is the atomizer's gas-to-liquid supply ratio GLR, as defined for twin-fluid atomizers in the section 1.2.3.

To investigate the effects of the interaction between the three main flows upon the spray, the maximum deflection (x/d for $y/d \cong 120$) is investigated in relation to GLR and the Weber number, Figure 3.30 and Figure 3.31 illustrate this correlation for Reynolds numbers of 1200 and 2700 respectively (lowest and higher liquid flows).

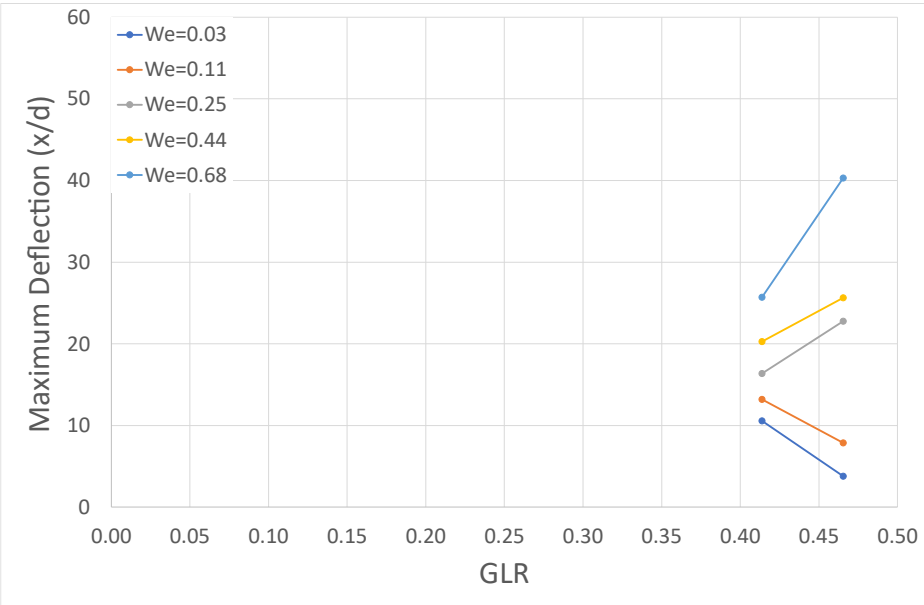

Figure 3.30 Maximum spray deflection in relation to GLR and We; Re=1200.

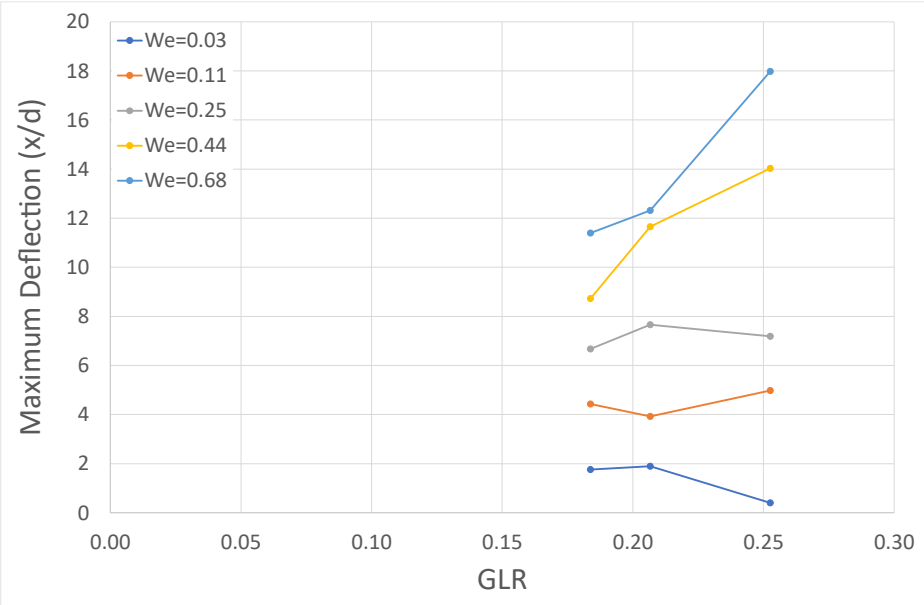

Figure 3.31 Maximum spray deflection in relation to GLR and We; Re=2700.

Generally, there is not a specific particular scheme expected in this situation. As the GLR increases, the momentum given to the spray increases, yet the atomization level of the spray is also higher, indicating a wider spray structure; thus, bigger aerodynamic area.

In the case of Re=1200 (low liquid flows) as it can be observed, in relatively low crossflows an increase in GLR causes a decrease in the maximum deflection of the spray. In this case, the increase of the atomizing air momentum is more significant than the increase in the aerodynamic area, due to the low momentum of the crossflow. As the Weber number increases, a semi-gradual shift of this norm can be observed, as the deflection tends to increase for increasing GLR, in more powerful crossflows. In this case, due to the high momentum of the crossflow, the momentum of the atomizing air is overshadowed, and the increase of aerodynamic interaction result in higher spray deflection.

Observing the case of Re=2700, a similar behavioral pattern is noticed. In relatively low crossflow (We=0.03), the same decrease of the deflection is noticed, for increasing GLR. In strong crossflows (We=0.44,0.68), increasing the GLR causes an increase in the maximum deflection. At the middle crossflows, approximately horizontal trendlines can be noted. For We=0.11, initially increasing the atomizing air reduces the deflection up to a point, where the inertia of the spray is low enough for the crossflow to takeover. The exact different mechanism is involved in We=0.25, where the deflection initially rises up to a point, from where the atomizing air overshadows the crossflow. Consequently, the mid-crossflow ranges

are the cases where the two parameters influencing the deflection of the jet, are about equal.

3.2.3 Spray Boundaries

The power-law fit procedure of the spray boundaries involves the isolation of the outer spray contour, its processing to be appropriate for interpolation and the separation into the upstream and downstream parts. The processing involves the isolation of the proper part for interpolation of the outer contour. The beginning of the spray has an irregular shape, since it constitutes the point of atomization, and that can influence the power-fit negatively. In addition, after a certain point down the spray, the boundaries are displayed to start converging instead of diverging which is expected according to theory. This is due to inability of the camera to capture the whole structure after a certain point since the dispersion of the spray becomes too high and therefore the spray density too low. The tracing for the spray boundaries is illustrated in Figure 3.32.

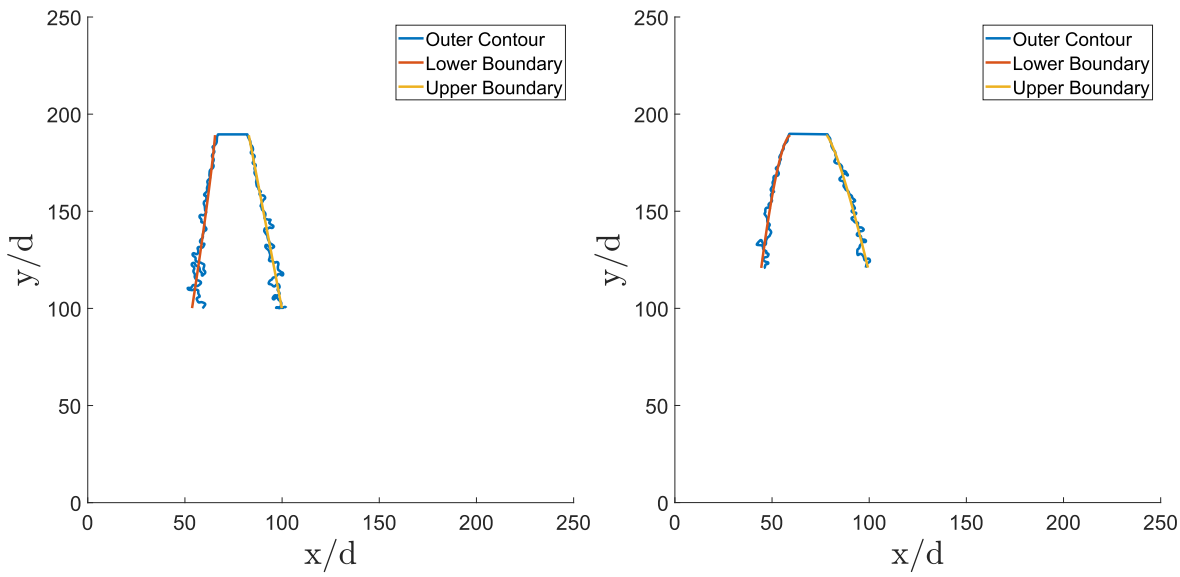

Figure 3.32 Power-law fit for spray boundaries (Re=1200, We-0.0, GLR=0.47); 0° and 90° respectively.

The tracing of the spray boundaries involves employing a power-law interpolation in a similar manner to the case of the centerline of the trajectory. Generally, the expected

pattern of the spray boundaries is the gradual increase of the spray coverage (section 1.4.4). However, in terms of specific theoretical results about the trajectories of the spray boundaries there is limited information available. Partially this is on account of the large variety of atomizer apparatuses that produce an equally large diversity of spray structures. Accordingly, the results and even the study procedure can differ to a great extend depending on the type of atomizer utilized; and thus, the spray shape formed.

Figure 3.33, Figure 3.34 and Figure 3.35 illustrate the exponential factor governed by Weber and Reynolds numbers, of the upper and lower boundaries respectively.

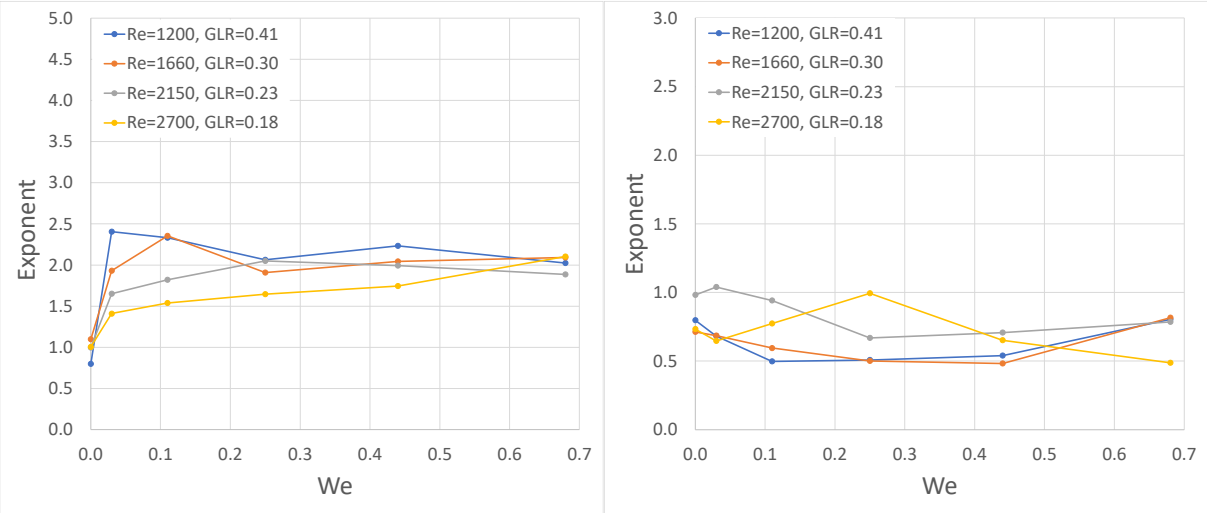

Figure 3.33 0° orientation, 8L/min atomizing air; exponent of downstream and upstream boundaries respectively.

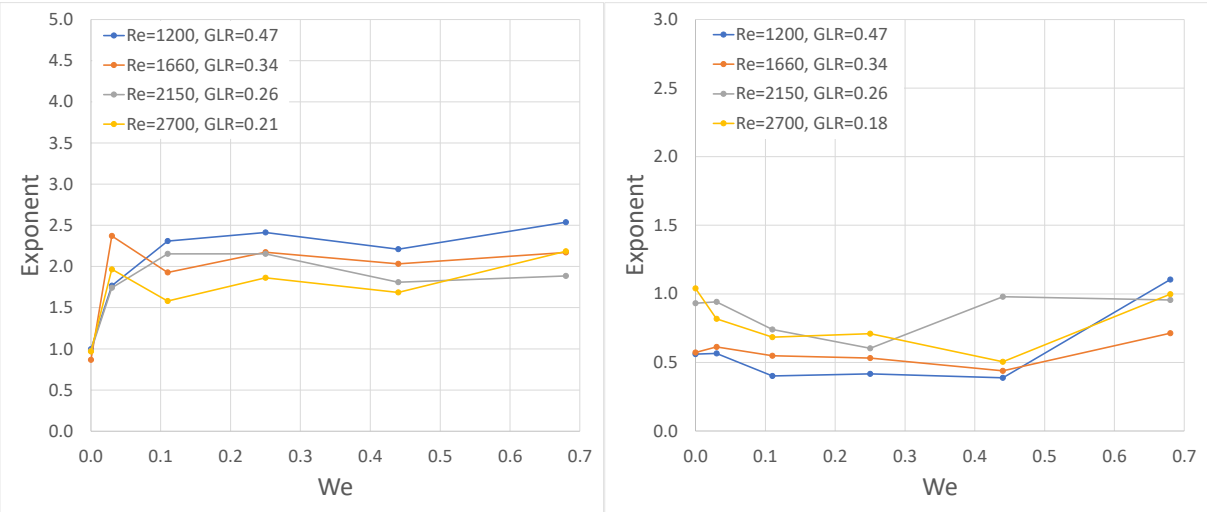

Figure 3.34 0° orientation, 9L/min atomizing air; exponent of downstream and upstream boundaries respectively.

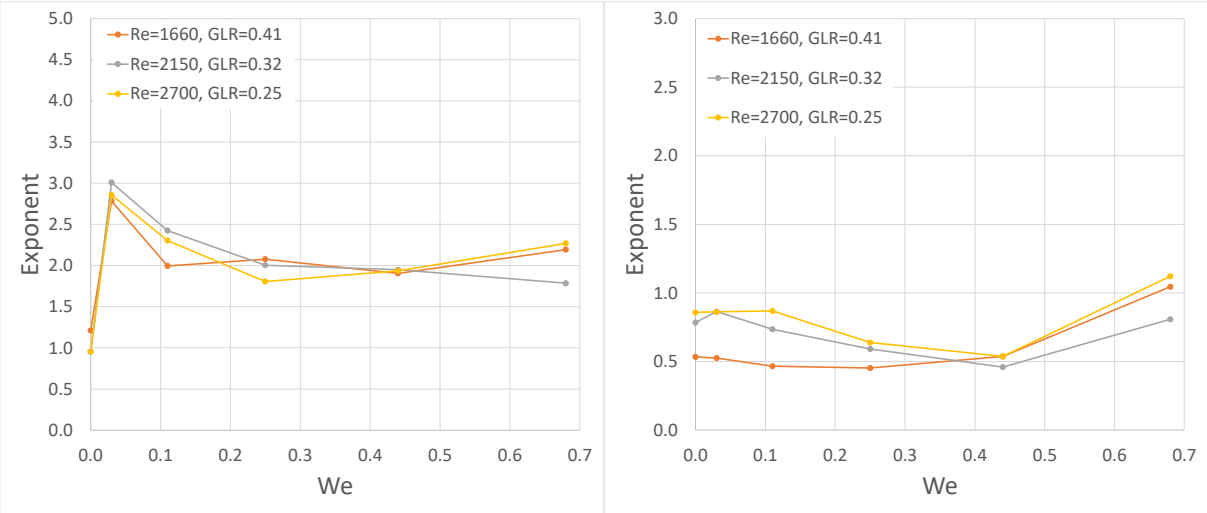

Figure 3.35 0° orientation, 11L/min atomizing air; exponent of downstream and upstream boundaries respectively.

For the downstream boundary, in the case of We=0 the values vary in 0.8-1.3. The exponent revolves around the value of 1 in zero crossflow conditions, which is expected since the boundaries theoretically follow a linear path in a quiescent atmosphere. In the case of We>0 the corresponding values are in 1.5-3.0 with an average value of 1.88. The exponents are much closer to the theoretical value of 2, indicated by the theory. Additionally, it seems that generally the accuracy of the power-law increases for higher Weber. An important observation can be made in the specific case of 11L/min and We=0.03 where the exponent is increased at about 3. This rapid exponent increase is only observed in this particular case of Weber and atomizer air, which corresponds to the higher atomization-lowest crossflow case. For the upstream boundary, the exponent values vary in 0.4-1.2 with an average exponent of 0.70. The exponent seems to be closer to the value of 1, while also following a parabola-like shape. Generally, different results are expected by the upstream boundary, since its trajectory opposes the airflow, and the phenomenon is not vertically symmetric.

Figure 3.36, Figure 3.37 and Figure 3.38 illustrate the upper and lower exponents respectively, for 90° orientation of atomizer.

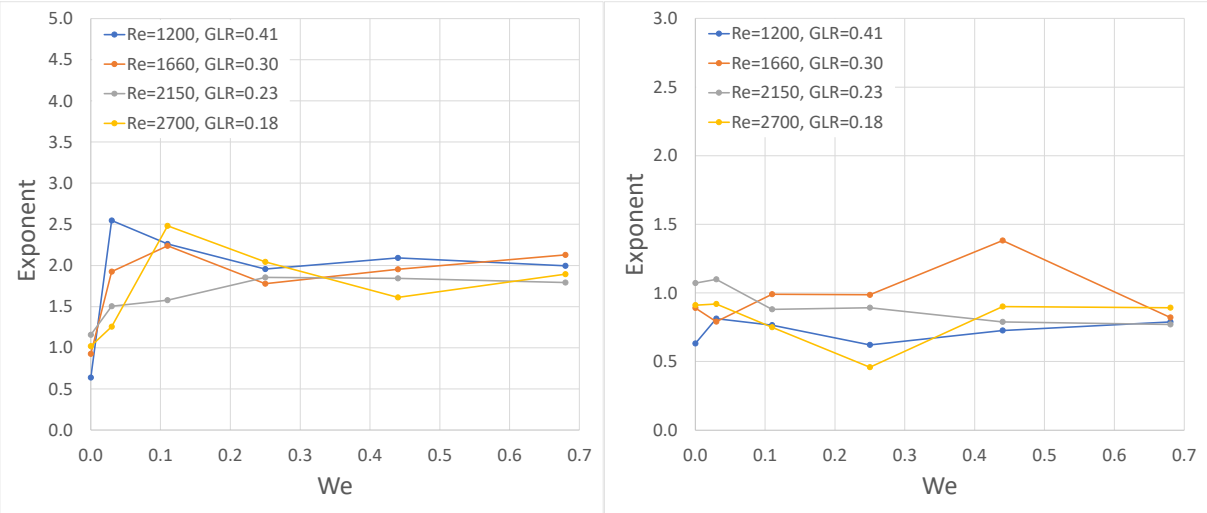

Figure 3.36 90° orientation, 8L/min atomizing air; exponent of downstream and upstream boundaries respectively.

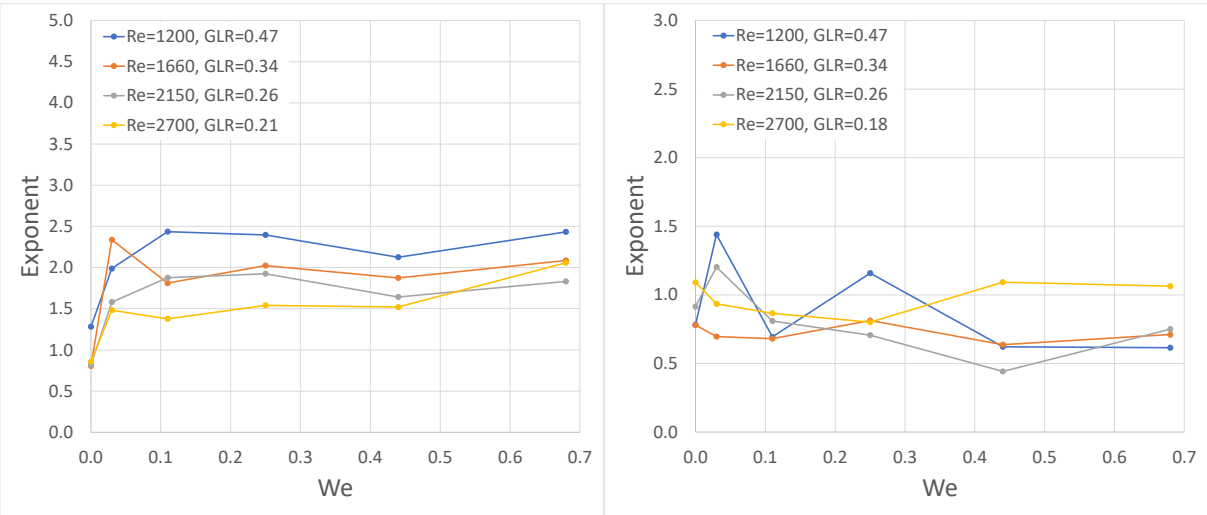

Figure 3.37 90° orientation, 9L/min atomizing air; exponent of downstream and upstream boundaries respectively.

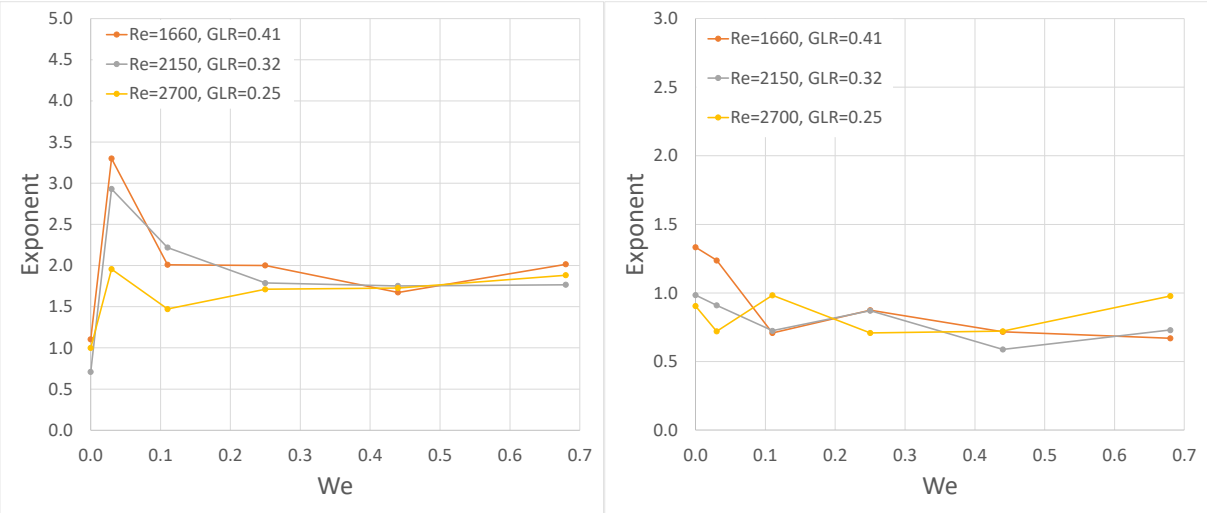

Figure 3.38 90° orientation, 11L/min atomizing air; exponent of downstream and upstream boundaries respectively.

For the downstream boundary, in the case of We=0 the exponent varies between 0.6-1.3 revolving around the value of 1 as expected. For We>0, the values vary in 1.3-3.3 with an average exponent of 1.78. As Weber increases, the exponent values are closer to the value of 2.

For the upstream boundary, the values vary in 0.45-1.45, with an average value of 0.85. The exponents are closer to 1, similar to the other atomizer orientation. In contrast to the other orientation, the parabolic behavior is nonexistent for atomizer air 8L/min, however it is progressively more noticeable moving to 9L/min and then 11L/min. This can be explained by the more chaotic nature of the phenomenon, in this particular orientation, where the minor axis is normal to the crossflow, analyzed in section 3.2.2.

Chapter 4 Conclusions

In this investigation, the characteristics of a spray or jet in crossflow were investigated, through experimental procedures. To summarize, the method of shadowgraphy was implemented using a CCD camera for the experiments. The experiments were distinguished into two main subjects: the Liquid Jet in Cross-Flow and Liquid Spray in Cross-Flow. The main study interests involved the spray/jet trajectory, the column breakup location (CBL) of the jet, and the spray boundaries.

In this chapter, the conclusions and associations that emerged from the results of the investigation are summarized. Generally, the conclusions are distinguished into the two main subjects of LJICF and LSICF, while some of the conclusions are general and apply for both cases. During the investigation, the following conclusions were demonstrated:

Generally

1. Higher aerodynamic Weber, results in higher deflection of the liquid from the vertical direction.
2. Increasing the Weber, results in lower penetration of the jet.
3. Higher liquid Reynolds results in lower liquid deflection by the crossflow.

Liquid Jet in Cross-Flow

1. The jet penetration standard deviation increases for higher Reynolds. The effect of Weber is negligible.
2. The deflection standard deviation is generally unaffected by both Weber and Reynolds numbers, except the case of Re=1200 (lowest flowrate) where the deflection St.D. drops for increasing Weber.
3. The atomizer orientation does not have a significant effect on the jet development.
4. The trajectory of the jet can be described by the power-law with good accuracy. The accuracy increases for higher Weber.

5. For most cases, the exponent ranges in 1.85-2.3 which agrees with the according theory, with an exponent around 2.
6. At low Weber, higher Reynolds results in increasing deviation of the exponent from the value of 2. This is especially noticeable at We=0.03, for Re=2150 and Re=2700.

Liquid Spray in Cross-Flow

1. The dispersion of the spray increases as the atomizer GLR increases. A sparse spray is produced for high GLR, while a more solid spray is produced for low GLR.
2. The trajectory of the spray is governed by the three flows of liquid, crossflow, and atomizer air.
3. The spray elliptical, therefore the interaction with the crossflow depends on the atomizer orientation.
4. The spray is deflected more when its major axis is normal to the crossflow (0°), than when the minor axis is normal to the crossflow (90°).
5. The spray behavior is more chaotic when the minor axis is normal to the crossflow.
6. The centerline of the spray can be described by the power-law with good accuracy.
7. For the most cases, the exponent ranges in 1.25-2.3 when the major axis is normal to the crossflow, and in 1.1-2.8 when the minor axis is normal to the crossflow.
8. The GLR of the atomizer affects the trajectory. For low Weber, increasing GLR results in decreasing deflection, while for high Weber, increasing GLR results in increasing deflection.
9. The coverage of the spray increases for higher GLR.
10. The spray boundaries can be described by the power-law with good accuracy. The only exception is at the lowest momentum flux ratio q=70, where the upstream boundary is almost vertical.
11. The upstream and downstream boundaries behave differently, due to the asymmetry of the phenomenon.
12. At atomizer orientation 0° (major axis normal to crossflow):
    12.1 The downstream boundary, in crossflow conditions (We>0), has an exponent between 1.5-3.0 with an average value of 1.88, close to the theoretical value of 2. The accuracy increases for higher Weber.

12.2 The upstream boundary has an exponent at 0.4-1.2 with an average value of 0.70. The exponent is closer to the value of 1. In general, the trendlines tend to follow a parabola-like scheme.

13. At atomizer orientation 90° (minor axis normal to crossflow):

13.1 The downstream boundary, in crossflow conditions (We>0), has an exponent between 1.3-3.3 with an average value of 1.78. As Weber increases, the accuracy to the theoretical value of 2 increases.

13.2 The upstream boundary has an exponent between 0.45-1.45 with an average value of 0.85, close to the value of 1. The trendlines seem more irregular from the case of 0° orientation.

Chapter 5 References

Amini, G. (2018). Linear Stability Analysis of a Liquid Jet in a Weak Crossflow. *Physics of Fluids*, *30*(8). https://doi.org/10.1063/1.5043589

Ashgriz, N. (2011). *Handbook of Atomization and Sprays: Theory and Applications*.

Berrocal, E., & Jönsson, J. (2012). *Development of Future Spray Imaging Techniqunes using General Purpose GPU Accelerated Monte Carlo Simulation*.

Birouk, M., & Lekic, N. (2009). Liquid Jet Breakup in Quiescent Atmosphere: A Review. *Atomization and Sprays*, *19*(6), 501–528.

Bradshaw, P., & Pankhurst, R. C. (1964). The Design of Low-Speed Wind Tunnels*. *Progress in Aerospace Sciences*, *5*, 9–11.

Cameron Tropea, Alexander L., YarinJohn, & F. Foss. (2007). *Springer Handbook of Experimental Fluid Mechanics*.

Guildenbecher, D. R., López-Rivera, C., & Sojka, P. E. (2009). Secondary Atomization. *Experiments in Fluids*, *46*(3), 371–402. https://doi.org/10.1007/s00348-008-0593-2

Gutiérrez, E., de Jesus Barreto, J., Garcia-Hernandez, S., Morales, R., & González-Solorzano, M. G. (2020). Decrease of Nozzle Clogging Through Fluid Flow Control. *Metals*, *10*(11), 1–19. https://doi.org/10.3390/met10111420

Lefebvre, A. H., & Mcdonell, V. G. (2017). *Atomization and Sprays (2nd Edition)*.

Lord Rayleigh F.R.S. (1878). On the Instability of Jets. *Proceedings of the London Mathematical Society*, *10*(1), 4–13.

M. Ruger, S. Hohmann, Martin Sommerfeld, & Gangolf Kohnen. (2000). Euler/Lagrange Calculations of Turbulent Sprays: The Effect of Droplet Collisions and Coalescence. *Atomization and Sprays*, *10*(1).

No, S.-Y. (2015). A Review on Empirical Correlations for Jet/Spray Trajectory of Liquid Jet in Uniform Cross Flow. *International Journal of Spray and Combustion Dynamics*, *7*(4), 283–314.

P.-K. Wu, & G. M. Faeth. (1993). Aerodynamic Efffects on Primary Breakup of Turbulent Liquids. *Atomization and Sprays*, *3*(3), 265–289.

Plateau J. (1873). Statique Expérimentale et Théorique des Liquides Soumis aux Seules Forces Moléculaires. *Nature*, *10*, 119–121.

Savart, F. (1833). Suit du Memoire sur le Choc Dune Veine Liquid Lancée Contre un Plan Circulaire. *Annales de Chimie et de Physique*, *54*.

Seykens, X. L. J., Somers, L. M. T., & Baert, R. S. G. (2004). *Modelling of Common Rail Fuel Injection System and Influence of Fluid Properties on Injection Process*.

Surya Prakash, R., Sinha, A., Tomar, G., & Ravikrishna, R. v. (2018). Liquid Jet in Crossflow – Effect of Liquid Entry Conditions. *Experimental Thermal and Fluid Science*, *93*, 45–56. https://doi.org/10.1016/j.expthermflusci.2017.12.012

Weber C. (1931). On the Breakdown of a Fluid Jet. *ZAMM*, *11*, 136–159.